Electronic Thesis and Dissertation Repository

1-14-2011 12:00 AM

Magnetic Excitations in Cylindrical Multilayered Nanostructures

Tushar K. Das, *University of Western Ontario*

Supervisor: Dr. Michael G. Cottam, *The University of Western Ontario*
A thesis submitted in partial fulfillment of the requirements for the Doctor of Philosophy degree in Physics
© Tushar K. Das 2011

Follow this and additional works at: https://ir.lib.uwo.ca/etd

Recommended Citation

MAGNETIC EXCITATIONS IN CYLINDRICAL MULTILAYERED
NANOSTRUCTURES

(Thesis format: Monograph)

by

Tushar <u>Das</u>

Graduate Program in Physics

A thesis submitted in partial fulfillment
of the requirements for the degree of
Doctor of Philosophy

The School of Graduate and Postdoctoral Studies
The University of Western Ontario
London, Ontario, Canada

THE UNIVERSITY OF WESTERN ONTARIO
SCHOOL OF GRADUATE AND POSTDOCTORAL STUDIES

CERTIFICATE OF EXAMINATION

Supervisor

_____
Dr. Michael G. Cottam

Examiners

_____
Dr. Lyudmila Goncharova

_____
Dr. Giovanni Fanchini

_____
Dr. François Lagugné-Labarthet

_____
Dr. Shyamal K. Bose

The thesis by

Tushar <u>Das</u>

entitled:

Magnetic Excitations in Cylindrical Multilayered Nanostructures

is accepted in partial fulfillment of the
requirements for the degree of
Doctor of Philosophy

Date: _____
Chair of the Thesis Examination Board

ABSTRACT

The recent fabrication of arrays of magnetic nanowires, nanotubes and nanorings, along with studies by Brillouin light scattering and magnetic resonance, have motivated us to present the theory of spinwaves in ferromagnetic and antiferromagnetic cylindrical multilayer systems. The calculations are applied to situations where the external magnetic field is parallel to the cylindrical axis and the structures have a large length-to-diameter aspect ratio. A macroscopic continuum theory is developed for the bulk and surface SW properties for various regimes of wavevectors.

First, a theory is given for magnetostatic modes, where the dipole-dipole interactions dominate over the exchange interactions in the SW dynamics. This situation can be realized at sufficiently small wavevectors by inelastic light scattering or magnetic resonance techniques. The magnetostatic form of Maxwell's equations and electromagnetic boundary conditions are used to derive the SW dispersion relations in nanotubes. A transfer matrix formalism is subsequently used to generalize these calculations to cylindrical multilayers consisting of a core surrounded by any arbitrary number of concentric tubular layers. Each layer may be ferromagnetic, antiferromagnetic or a nonmagnetic spacer. Attention is given to the localized interface modes, which are shown to be strongly modified due to the curved interfaces, compared to the behavior found in planar geometries. Specific investigations of interface effects on the dipolar modes are carried out for bilayer cylindrical systems where ferromagnetic and antiferromagnetic materials are formed in direct contact.

Next, the theory in magnetic cylindrical tubes is extended to the magnetic polaritons that arise at smaller wavevectors from the coupling between electromagnetic waves and the dipolar SW excitations. This involves solving for the dynamical response using the full form of Maxwell's equations with retardation effects now included. Results for the limiting (single-interface) special cases of wires and anti-

wires are also deduced. Another extension of the theory is to the dipole-exchange SW in magnetic nanotubes. This is applicable at larger wavevectors, where the long range dipole-dipole interactions and the short range exchange interactions are both important in the magnetization dynamics. These calculations describe the radial and angular quantization of the different modes in cylindrical geometries and can be compared to Brillouin light scattering experiments.

A formalism is also developed for the magnetic linear response functions (or Green's functions) in magnetic nanotubes, taking the wavevector regime of the magnetostatic modes as an example. This enables us to calculate the spectral intensities of the surface and bulk magnetostatic SW modes, and it is also useful for interpreting Brillouin light scattering data. Numerical applications are presented throughout for ferromagnets, such as Ni, Permalloy, and EuS, and for antiferromagnets, such as $GdAlO_3$ and MnF_2.

ACKNOWLEDGMENTS

To my parents:

Ramendra K. Das

&

Anita Das.

CONTENTS

LIST OF FIGURES

LIST OF COMMONLY USED ABBREVIATIONS

AF	Antiferromagnet(s) or antiferromagnetic
AFMR	Antiferromagnetic resonance
ATR	Attenuated total reflection
BLS	Brillouin light scattering
DESW	Dipole-exchange spin-wave(s)
F	Ferromagnet(s) or ferromagnetic
FMR	Ferromagnetic resonance
GMR	Giant magnetoresistance
HDD	Hard disc drives
INS	Inelastic neutron scattering
LL	Landau-Lifshitz
LLG	Landau-Lifshitz-Gilbert
RLS	Raman light scattering
S	Nonmagnetic spacer
SW	Spin wave(s)
TE	Transverse electric
TEM	Transverse electromagnetic
TM	Transverse magnetic

CHAPTER 1
Introduction

1.1 Overview of magnetism

During the last two or three decades nanomagnetism has emerged as a field of outstanding scientific advances due to novel physical properties distinct those of bulk magnetic materials. Understanding the static and dynamic properties of nanomagnetic structures, together with the interpretation of experimental data and the desire to fabricate magnetic nanostructures in a controlled manner, have created the need for reliable and predictive theoretical models [1].

Following the early discovery of magnetite (Fe_3O_4) in the ancient age, the most striking advances in magnetism were made in the 18th and 19th centuries, namely establishing the connection between electricity and magnetism. In 1873 Maxwell formulated the mathematical relationships between electricity and magnetism on the basis of earlier ideas by Gauss, Ampère and Faraday. These relationships (Maxwell's equations) formed the backbone of electromagnetism [2] and were consistent with the dipolar character of magnetostatic forces and interactions. By the mid 19th century, the connection between macroscopic and microscopic magnetism was being developed, culminating eventually in the milestone advances due to quantum physics [3]. Later, there have been extensive technological applications of magnetic thin films made in sensor and storage industries [4].

In the last few years magnetic multilayered nanostructures have been receiving considerable attention due to their interface and surface effects. This opened the way for the discovery of new phenomena such as the giant magnetoresistance (GMR) of magnetic multilayers in 1988, for which Fert and Grünberg were awarded the 2007 Nobel Prize in Physics. The GMR effect is used in various devices, which

include the read heads of the hard disc drives (HDD) of our computers (increasing the storage density by a factor of > 100), spin filtering, sensing, spin logic devices [1, 5]. Modern spintronics demands high density storage media with smaller, faster, cheaper and lower power consumption than the existing ones. It is known that thermal effects limit further reduction of magnetic devices in ultra-high-density magnetic recording [6]. However, the discovery by Meiklejohn and Bean [7] about 50 years ago of 'exchange anisotropy' in coupled ferromagnetic / antiferromagnetic bilayer films has now been utilized to extend the applicability of magnetic nanostructures further in HDD [8]. There are also various other potential applications, e.g., the microwave-signal-processing devices described in [9] and the recent fabrication of one-dimensional magnonic crystals in [10, 11].

Magnetic materials are usually classified as diamagnetic, paramagnetic, ferromagnetic (F), antiferromagnetic (AF), or ferrimagnetic. In diamagnetic materials, the constituent atoms or molecules have no permanent magnetic moment, but in an external magnetic field there is a weak negative magnetic susceptibility [12]. The other materials where the atoms have permanent magnetic moments are represented schematically in Fig. 1.1. In paramagnetic materials the magnetic moments have negligible coupling to each other, and so in the absence of an applied field there is a random arrangement of magnetic moments. An applied field leads to a weak positive magnetic susceptibility. When interactions between different magnetic moments are significant, a much stronger effect is observed. In the case of a F material the atomic magnetic moments interact with each other to favour a parallel alignment. In AF materials the interaction between neighbouring atoms produces an anti-parallel alignment of the atomic magnetic moments. In ferrimagnetic materials the atomic magnetic moments are also coupled with anti-parallel alignment but they are unequal in magnitude. The magnetic ordering breaks down at a critical temperature, above which the materials show a paramagnetic behaviour [12, 13].
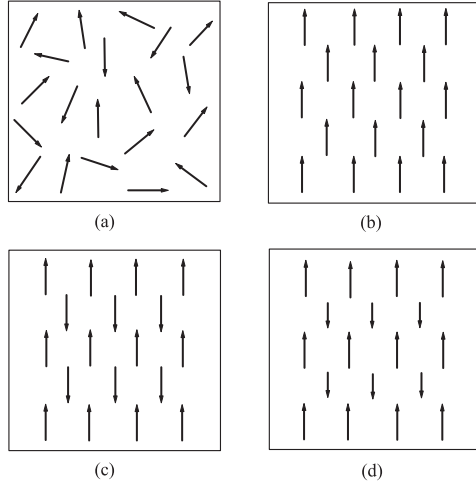
Figure 1.1: Schematic diagram of the alignment of magnetic moments in (a) para-magnetic materials, (b) F materials, (c) AF materials, and (d) ferrimagnetic materials.

1.2 Magnetic interactions

In strong magnetic materials the interactions between the atomic magnetic moments depend on their separation and relative orientation. One of the most basic interactions is the magnetic dipole-dipole interaction, which comes from the fact that each magnetic dipole will produce a magnetic field around it. A second dipole will acquire a potential energy if it is placed within the magnetic field of the first dipole [2, 14]. In an array the total dipolar interaction energy is obtained by summing over all pairs of magnetic sites, and hence the magnetic Hamiltonian resulting from the dipole-dipole interaction is (in SI units) [15]

$$\mathcal{H}_{dip} = \frac{\mu_0}{4\pi} \sum_{<i,j>} \frac{(\vec{m}_i \cdot \vec{m}_j)r_{ij}^2 - 3(\vec{m}_i \cdot \vec{r}_{ij})(\vec{m}_j \cdot \vec{r}_{ij})}{r_{ij}^5}, \tag{1.1}$$

where $\vec{r}_{ij}$ is the vector joining sites i and j, μ_0 is the permeability of free space, and the summation is over all distinct pairs of sites. The dipole-dipole interactions

are long range in nature, varying with distance like $(r_{ij})^{-3}$. In a continuum model the dipolar fields can also be calculated directly from the magnetostatic form of Maxwell's equations. Although the dipole-dipole interaction can play an important role in the dynamical properties of magnetic materials, they are relatively weak.

The magnetic order must be produced by another, much stronger interaction (typically of the order of few eV). This is the quantum-mechanical exchange [16], proposed by Heisenberg. It can be explained in terms of the electrons obeying Fermi-Dirac statistics and thus having a total wave function (with its spatial and spin parts) that must be antisymmetric under interchange of any two electrons. An interaction arises provided there is overlap of the individual electronic wavefunctions. The effective Hamiltonian between a pair of electrons 1 and 2 is expressible as

$$-\frac{1}{(g\mu_B)^2}J(r)\vec{m}_1 \cdot \vec{m}_2, \tag{1.2}$$

where $\vec{m}_1$ and $\vec{m}_2$ are the magnetic moments for the two electrons, g is the Landé g-factor, μ_B is the Bohr magneton, and $J(r)$ is called the exchange energy. Parallel alignment of magnetic moments will be favoured if J is positive and antiparallel alignment if J is negative. Generalizing the above expression, the Heisenberg Hamiltonian for ordered magnetic materials is

$$\mathcal{H}_{ex} = -\frac{1}{(g\mu_B)^2}\sum_{<i,j>} J_{ij}\vec{m}_i \cdot \vec{m}_j . \tag{1.3}$$

The exchange energy falls off rapidly with increasing distance r_{ij} between the sites. It is a short range interaction, often involving only the nearest neighbour interactions. However, it can explain many static properties (such as the magnetization and the critical temperature) of magnetic materials [16, 17].

In a macroscopic continuum model the exchange energy corresponding to the

Hamiltonian H_{ex} of Eq. (1.3) becomes

$$E_{ex} = -\frac{1}{2(g\mu_B)^2} \int d^3r \int d^3r' \, J(\vec{r}-\vec{r}')\vec{M}(\vec{r}).\vec{M}(\vec{r}'), \qquad (1.4)$$

where $J(\vec{r}-\vec{r}') > 0$ for a F material and $|\vec{M}(\vec{r})| = M_0$ gives the saturation magnetization. As the exchange is short range, we may use a Taylor series expansion of $\vec{M}(\vec{r})$ at the point $\vec{r}'$ as

$$\vec{M}(\vec{r}) = \vec{M}(\vec{r}') + [(\vec{r}-\vec{r}').\vec{\nabla}]\vec{M}(\vec{r}') + \frac{1}{2} + [(\vec{r}-\vec{r}').\vec{\nabla}]^2\vec{M}(\vec{r}') + \dots . \quad (1.5)$$

On substituting $\vec{M}(\vec{r})$ into Eq.(1.4), the first energy term gives a constant for the material, the next energy term vanishes as the integral contains an odd power of $(\vec{r}-\vec{r}')$, and the third term leads to an energy contribution of

$$E_{ex}^{(2)} = -\frac{1}{4} \int d^3r' \frac{\vec{M}(\vec{r}')}{M_0}.D\nabla^2\vec{M}(\vec{r}'), \qquad (1.6)$$

where D is a property of the material called the spin-wave stiffness. It is given by $[M_0/(g\mu_B)^2] \int d^3r J(\vec{r}-\vec{r}')(\vec{r}-\vec{r}')^2$ for a cubic crystal.

There can be effects due to magnetic anisotropy, in addition to the so-called "shape anisotropy" which is just part of the magnetic dipole-dipole interaction [18]. There is anisotropy related to the crystal symmetry (e.g., there may be certain directions, relative to the crystal unit cell axes, for which it is easier to magnetize the crystal), which is called magnetocrystalline anisotropy and is a consequence of the spin-orbit interaction. Magnetic anisotropy can also arise due to mechanical stress, in which case it is known as magnetostrictive anisotropy. Often the anisotropy (magnetocrystalline or magnetostrictive) has uniaxial symmetry and is represented

by an effective Hamiltonian:

$$\mathcal{H}_{anisotropy} = -H_A(T) \sum_i m_i{}^z, \tag{1.7}$$

where H_A denotes an effective anisotropy field. There is another type of anisotropy, usually called 'exchange anisotropy', when F and AF materials are in contact (e.g., in a bilayer or multilayer). Exchange anisotropy is reviewed in [19], and we discuss it further in Chapter 3 with its application in cylindrical geometries.

Finally, an applied static magnetic field, taken to be in the z direction (i.e., $\vec{H} = H_0 \hat{z}$), gives an extra term in the Hamiltonian, called the Zeeman energy [16]:

$$\mathcal{H}_{Zeeman} = -\sum_i \vec{H} \cdot \vec{m}_i = -H_0 \sum_i m_i{}^z. \tag{1.8}$$

1.3   Spin-wave excitations in magnetic materials

Spin waves are the low-lying collective excitations in ordered magnetic material (see, e.g., [16]). In 1930 Bloch proposed spin waves (henceforth SW) as wave-like deviations of each spin from the ground-state alignment. At zero temperature the spins are strongly aligned, but if the temperature is increased (or a perturbation is applied) a single spin will deviate from alignment. Due to the coupling between spins (or their magnetic moments), the deviation becomes associated with all the magnetic ions and forms a collective excitation propagating through the solid in a wave-like fashion. The SW are quantized and, by analogy with the phonon, the basic quantum is the magnon. A schematic diagram of a bulk SW in a ferromagnet is illustrated in Fig. 1.2.

The nature of the SW in magnetic materials depends on the dominant magnetic interaction for the *spin dynamics*. This in turn depends on the magnitude of the wave vector $\vec{q}$ of the SW. For small enough $|\vec{q}|$, the influence of long range dipole-dipole interactions becomes significant and can dominate over the short range
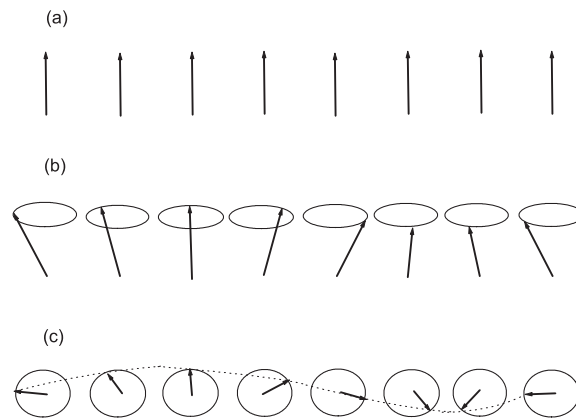
Figure 1.2: The spin wave in a F in one dimension: (a) the ground state; (b) perspective view of the spin wave excitation in the bulk material and (c) from above.
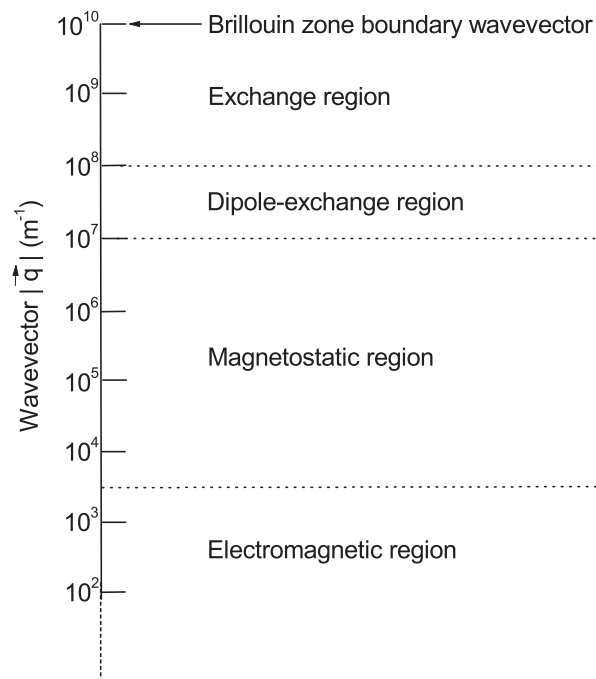
Figure 1.3: The different regimes of magnetic excitations in terms of the magnitude of SW wavevector.
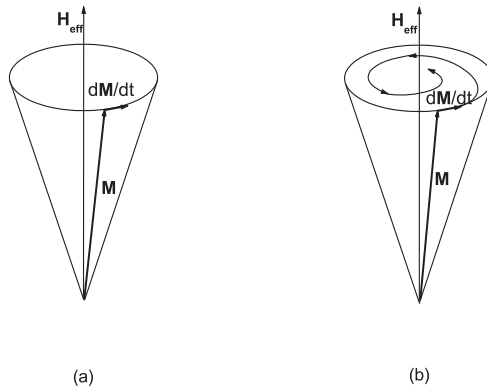
Figure 1.4: Precession of the magnetic moment around the effective magnetic field
(a) without and (b) with damping.

exchange interactions. This region of magnetic excitations is called the magneto-static region (if retardation can be ignored). For even smaller $|\vec{q}|$ the region with retardation effects included is called the electromagnetic (or polariton) region. SW in both of the above regions have wavelengths that are large compared to the inter-atomic spacing. On the other hand, the short range exchange interaction dominates over the long range dipole-dipole interactions for the SW with much larger $|\vec{q}|$. This is the exchange region and it includes most of the Brillouin zone. The intermediate regime of magnetic excitations, in which dipolar and exchange interactions both play a role, is known as the dipole-exchange region. The different regions are shown in Fig. 1.3, taking typical values for a F.

A SW analysis can be carried out in different ways, e.g., see [15, 20]. Here we use a macroscopic (or continuum) approach, which is appropriate for long wavelengths (or small $|\vec{q}|$). In a semi-classical approach the precessional motion of the magnetization $\vec{M}$ is derived from a torque exerted on it by an effective magnetic field, as shown schematically in Fig. 1.4. The torque equation with a damping term

included is known as the Landau-Lifshitz-Gilbert (LLG) equation:

$$\frac{d\vec{M}}{dt} = \gamma\mu_0 \left(\vec{M} \times \vec{H}_{eff} \right) - \frac{\alpha_0}{M} \left(\vec{M} \times \frac{d\vec{M}}{dt} \right).$$
(1.9)

The first term on the right hand side is the contribution of the torque produced by the total effective field ($\gamma = g\mu_B$ is the gyromagnetic ratio). The second term is the Gilbert damping term, proportional to a dimensionless damping factor α_0. Sometimes the damping is ignored or written in a different form. The field $\vec{H}_{eff}$ in Eq. (1.9) is the sum of the dipolar, exchange, anisotropy and applied fields, i.e.,

$$\vec{H}_{eff} = \vec{H}_{dip} + \vec{H}_{ex} + \vec{H}_{anisotropy} + \vec{H}_{applied}.$$
(1.10)

The contribution $\vec{H}_{dip}$ contains the static and fluctuating terms generated due to the dipole-dipole interactions. It can either be expressed via Maxwell's equation for the continuum model or alternatively deduced from Eq. (1.1) for a discrete (microscopic) model. The term $\vec{H}_{ex}$ represents the field contribution due to the exchange interaction. It can be deduced from Eqs. (1.4) - (1.6) and is often written in terms of static and fluctuating parts for the macroscopic model [16] as

$$\vec{H}_{ex} = \lambda\vec{M} + \frac{D}{M_0}\nabla^2\vec{M},$$
(1.11)

where λ is an exchange constant and D is the exchange stiffness mentioned earlier. The anisotropy term in Eq. (1.10) can often be neglected in cubic crystals [16, 21]. The last term in Eq. (1.10) is the static external applied field.

In this thesis the long-wavelength SW in F and AF materials will be studied analytically using a continuum model. It will be assumed in some cases that the long range dipole-dipole interactions are dominant over the exchange, but generalizations are made in later chapters. The static magnetization in the continuum approach is

usually taken to be spatially uniform inside the material and the fluctuating parts of the magnetization and the effective fields are assumed to vary slowly on the atomic scale. In the macroscopic continuum approach the dipolar field in Eq. (1.10) will be analyzed in terms of Maxwell's equations. When $q \gg \omega/c$, where ω is the angular frequency of the SW and c is the light velocity, the retardation effects are negligible, corresponding to the magnetostatic region in Fig. 1.3.

Magnetostatic SW modes were first studied by Walker for F materials [22], where the neighbouring magnetic moments are almost parallel and the static exchange field is simply proportional to the magnetization, i.e., it is $\lambda \vec{M}$ from Eq. (1.11). As a result, the exchange field does not create a torque on the magnetization since $\vec{M} \times \lambda \vec{M} = 0$. In contrast, in an AF the static exchange field on one sublattice may affect the other sublattice. Also the influence of anisotropy is different in an AF because of the two sublattices. These additional effects in an AF cause the long-wavelength SW to be in the infrared frequency regime, whereas the long-wavelength SW of a F typically propagate in the microwave region [23].

1.4 Response functions for the magnetic susceptibility

To investigate SW at long wavelengths one first needs to find a frequency-dependent susceptibility tensor $\overleftrightarrow{\chi}$, which is a response function containing information about the fluctuating magnetization in the presence of a fluctuating field. For a F the effective field in Eq. (1.10) can be approximated as the sum of the static field H_0 in the z direction and a fluctuating field with angular frequency ω, i.e.,

$$\vec{H}_{eff}(\vec{r}, t) = H_0 \hat{z} + \vec{h}(\vec{r}) e^{-i\omega t}. \tag{1.12}$$

At this stage, we will ignore exchange and look just at the dipolar response. The fluctuating field $\vec{h}(\vec{r})$ comes from the dipolar field and generally $|\vec{h}(\vec{r})| \ll H_0$. The

corresponding response for the magnetization $\vec{M}(\vec{r}, t)$ is

$$\vec{M}(\vec{r}, t) = M_0 \hat{z} + \vec{m}(\vec{r}) e^{-i\omega t}. \tag{1.13}$$

Here M_0 is the static magnetization and $|\vec{m}(\vec{r})| \ll M_0$ typically. By substituting Eq. (1.12) and Eq. (1.13) into the torque equation of motion with damping neglected, and then linearizing (i.e. neglecting the second order small quantities), one finds

$$-i\omega \vec{m}(\vec{r}) = \gamma \mu_0 \hat{z} \times [M_0 \vec{h}(\vec{r}) - H_0 \vec{m}(\vec{r})]. \tag{1.14}$$

From Eq. (1.14) the linear relationship between the x and y components of $\vec{m}(\vec{r})$ and $\vec{h}(\vec{r})$ in terms of a response function takes the form (see, e.g., [16])

$$\begin{pmatrix} m_x \\ m_y \end{pmatrix} = \begin{pmatrix} \chi_a & i\chi_b \\ -i\chi_b & \chi_a \end{pmatrix} \begin{pmatrix} h_x \\ h_y \end{pmatrix}, \tag{1.15}$$

where

$$\chi_a = \frac{\omega_m \omega_0}{(\omega_0{}^2 - \omega^2)}, \quad \chi_b = \frac{\omega_m \omega}{(\omega_0{}^2 - \omega^2)}. \tag{1.16}$$

Both χ_a and χ_b have poles at the ferromagnetic resonance (FMR) frequency ω_0, and $\omega_m = \gamma \mu_0 M_0$. The m_z component is zero in the linear approximation.

Similarly, the frequency dependent susceptibility tensor in the AF case can also be derived from the torque equation of motion without damping. The analysis is slightly more complicated, because an AF has two sublattices of magnetic moments aligned in opposite directions. A torque equation of motion can be written down for each sublattice, including the terms that couple the sublattices. Eventually an expression similar to Eq. (1.15) is found for an AF, but χ_a and χ_b are now different

and are given by [20, 24]

$$\chi_a = \frac{1}{2}\left(\chi^+ + \chi^-\right), \quad \chi_b = \frac{1}{2}\left(\chi^+ - \chi^-\right), \tag{1.17}$$

where

$$\chi^\pm = \frac{2\omega_A\omega_m}{\omega_A(2\omega_E + \omega_A) - (\omega \mp \omega_0)^2}. \tag{1.18}$$

The additional frequencies are $\omega_E = \gamma\mu_0 H_{ex}$ and $\omega_A = \gamma\mu_0 H_{anisotropy}$. In the absence of an applied field, $\omega_0 = 0$, the susceptibilities in Eq. (1.18) have a pole at $\omega = \omega_{AF} = [\omega_A(2\omega_E + \omega_A)]^{\frac{1}{2}}$, which is the antiferromagnetic resonance (or AFMR) frequency, and $\chi^+ = \chi^-$ so $\chi_b = 0$. When $H_0 \neq 0$, $\overleftrightarrow{\chi}$ is non-diagonal and the resonances in χ^+ and χ^- are split by the Zeeman term, becoming $\omega_{AF} \pm \omega_0$ provided $\omega_0 < \omega_{AF}$.

1.5   Spin waves in a thin magnetic film

The study of SW properties in nanoscale magnetic structures has been a challenging and ongoing issue due its fundamental physics and potential for high-frequency device applications. Kittel [25] first predicted that the SW in finite F materials could be excited by a uniform r.f. field, and this was confirmed experimentally in a Permalloy thin film by Seavey and Tannenwald [26]. Surface magnetostatic SW were first investigated by Damon and Eshbach [27] for a F slab magnetized in-plane with an external magnetic field parallel to the surface. DeWames and Wolfram [28] extended the study of SW to the dipole-exchange regime, showing how exchange modifies the surface and bulk magnetostatic modes in a F film. Hartstein *et al* [29] extended the study of SW to the electromagnetic regime for a description of surface magnetic polaritons. The surface magnetostatic modes in AFs were studied for semi-infinite materials [30] and films [16, 23, 31]. The theoretical and experimental studies on the SW dynamics covering present and past years can be found in a
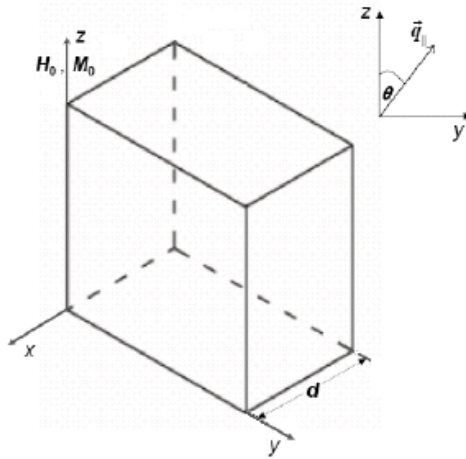
Figure 1.5: A planar F film of thickness d in the x direction and infinite in the other two directions, taking M_0 and H_0 parallel to the surfaces. The in-plane wave vector $\vec{q}_\parallel$ for the modes is shown.

number of excellent reviews [15, 16, 32, 33, 34, 35].

In the following subsections we briefly review the theory of SW excitations in a planar F slab (or film) in three different wavevector regimes. We consider a F film of thickness d, which is considered infinite in the y and z directions (see Fig. 1.5). The static magnetization M_0 and applied field H_0 are along the z axis. This planar case will later be compared with our results for cylindrical geometries.

1.5.1   Magnetostatic SW

The dipolar modes can be analyzed using the magnetostatic form of Maxwell's equations:

$$\vec{\nabla} \times \vec{h}(\vec{r}) = 0 \quad \text{and} \quad \vec{\nabla} \cdot \left[\vec{m}(\vec{r}) + \vec{h}(\vec{r})\right] = 0 . \tag{1.19}$$

The magnetic scalar potential ψ can be introduced from the first of Eq. (1.19) by defining $\vec{h}(\vec{r}) = \vec{\nabla}\psi(\vec{r})$. Substituting $\vec{h}$ in the second of Eq. (1.19) then implies

$$(1 + \chi_a)\left(\frac{\partial^2 \psi}{\partial x^2} + \frac{\partial^2 \psi}{\partial y^2}\right) + \frac{\partial^2 \psi}{\partial z^2} = 0 , \qquad (1.20)$$

which is often referred to as the Walker equation [22] inside the F film. Outside the F film it simplifies to the Laplace equation

$$\frac{\partial^2 \psi}{\partial x^2} + \frac{\partial^2 \psi}{\partial y^2} + \frac{\partial^2 \psi}{\partial z^2} = 0 . \qquad (1.21)$$

The film in Fig. 1.5 has translational symmetry parallel to the surface, and so the solutions of Eqs. (1.20) and (1.21) can be written in a Bloch form [36] as

$$\psi(\vec{r}) = \begin{cases} a_1 \exp(-q_{||}x)\exp(i\vec{q}_{||} \cdot \vec{r}_{||}) & \text{if } x > 0 \\ \{a_2 \exp(iq_x x) + a_3 \exp(-iq_x x)\}\exp(i\vec{q}_{||} \cdot \vec{r}_{||}) & \text{if } 0 > x > -d \\ a_4 \exp(q_{||}x)\exp(i\vec{q}_{||} \cdot \vec{r}_{||}) & \text{if } x < -d \end{cases} \qquad (1.22)$$

There the wave vector $\vec{q}_{||} = (q_y, q_z)$ is parallel to the surface and $\vec{r}_{||} = (y, z)$. For the so-called Voigt configuration in which $q_z = 0$ and $q_{||} = |q_y|$, we have angle $\theta = \pi/2$. The quantity q_x can be either real or imaginary and is determined from Eqs. (1.20) and (1.22). This gives

$$(1 + \chi_a)(q_x{}^2 + q_{||}{}^2) = 0. \qquad (1.23)$$

There are two possible solutions: either (a) $\chi_a = -1$, giving the solution for a bulk mode, or (b) $q_x = \pm i q_{||}$, giving the solution for a surface mode. The amplitude coefficients a_j ($j = 1, 2, 3, 4$) in Eq. (1.22) can be obtained using the standard electromagnetic boundary conditions at $x = 0$ and at $x = -d$. These boundary conditions are that ψ must be continuous and that $(h_x + m_x)$ just inside the magnetic

material must be equal to h_x just outside the material. These conditions lead to the vanishing of the determinant for the coefficients a_j, giving [16]:

$$q_{||}{}^2 + 2q_{||}q_x(1 + \chi_a)\cot(q_x d) - q_x{}^2(1 + \chi_a)^2 - q_y{}^2\chi_b{}^2 = 0. \tag{1.24}$$

In the case of a F material, the solutions for the bulk magnetostatic modes are found from $\chi_a = -1$ and give $\omega = \pm\omega_B(q_x, \vec{q}_{||}) = \pm[\omega_0{}^2 + \omega_0\omega_m]^{\frac{1}{2}}$. Similarly, the substitution of $q_x = \pm iq_{||}$ leads to the dispersion relation for a localized surface magnetostatic mode (or Damon-Eshbach mode) [27] as $\omega = \omega_S(\vec{q}_{||})$, where

$$\omega_S(\vec{q}_{||}) = \left\{(\omega_0 + \frac{1}{2}\omega_m)^2 - \frac{1}{4}\omega_m{}^2\exp(-2q_{||}d)\right\}^{\frac{1}{2}}, \tag{1.25}$$

which satisfies the inequality $\omega_B < \omega_S < \omega_0 + \omega_m/2$ for the Voigt geometry. Typically, the surface mode frequencies in F films correspond to the microwave region and have applications to signal processing [37]. They have an interesting property of "non-reciprocal propagation" such that when $\vec{q}_{||}$ is reversed the mode switches from the upper to lower surface, or vice versa. It can also be noted that "non-reciprocal propagation" occurs for uniaxial AFs, but only when $H_0 \neq 0$ [16].

1.5.2 Dipole-exchange SW

The theory of dipole-exchange SW (or DESW), where the dipole-dipole and exchange effects may be comparable, is developed next. The exchange field $\vec{H}_{ex}$ in Eq. (1.11) must now be added to Eq. (1.12) and consequently the linearized torque equation of motion (with damping ignored) becomes

$$-i\omega\vec{m}(\vec{r}) = -\omega_m\{\hat{z} \times \vec{h}_d(\vec{r})\} + (\omega_0 - D\nabla^2)\{\hat{z} \times \vec{m}(\vec{r})\}. \tag{1.26}$$

The dispersion relation for bulk DESW in an effectively infinite medium, where the mode propagation will take the plane-wave form $\exp(i\vec{q}.\vec{r})$, can be derived di-

rectly from Eqs. (1.26) and (1.19). The final expression is [38]:

$$\omega(\vec{q}) = \left\{ (\omega_0 + Dq^2)(\omega_0 + Dq^2 + \omega_m \sin^2\theta) \right\}^{\frac{1}{2}}. \tag{1.27}$$

This shows that the exchange and dipolar effects are comparable when $q \sim (\omega_m/D)^{1/2}$. By comparison with Eq. (1.20) for the magnetostatic case, Eq. (1.26) in the case of a film geometry yields a sixth-order differential equation for the scalar potential ψ inside the magnetic film, i.e.,

$$(\hat{\Theta}^2 + \omega_m \hat{\Theta} - \omega^2) \left(\frac{\partial^2 \psi}{\partial x^2} + \frac{\partial^2 \psi}{\partial y^2} \right) + (\hat{\Theta}^2 - \omega^2) \frac{\partial^2 \psi}{\partial z^2} = 0, \tag{1.28}$$

where $\hat{\Theta} = (\omega_0 - D\nabla^2)$ is a differential operator. The magnetic scalar potential ψ outside the F film satisfies Eq. (1.21) giving solutions for ψ in regions $x > 0$ and $x < -d$, as before. On the other hand, the solution of Eq. (1.28) for ψ in the region $0 > x > -d$ takes a superposition form as

$$\psi(\vec{r}) = \sum_{j=1}^{3} \left\{ a_2^j \exp(iq_x^j x) + a_3^j \exp(-iq_x^j x) \right\} \exp(i\vec{q}_{||} \cdot \vec{r}_{||}). \tag{1.29}$$

By substituting Eq. (1.29) into Eq. (1.28), the roots q_x^j (in case of $q_z = 0$) are

$$q_x^{(1)} = \pm i q_{||}, \tag{1.30}$$

$$q_x^{(2)} = \pm \left[\frac{1}{D} \left\{ \left(\omega^2 + \frac{\omega_m^2}{4} \right)^{1/2} - \frac{\omega_m}{2} - \omega_0 - Dq_{||}^2 \right\} \right]^{1/2}, \tag{1.31}$$

$$q_x^{(3)} = \pm i \left[\frac{1}{D} \left\{ \left(\omega^2 + \frac{\omega_m^2}{4} \right)^{1/2} + \frac{\omega_m}{2} + \omega_0 + Dq_{||}^2 \right\} \right]^{1/2}. \tag{1.32}$$

Here $q_x^{(1)}$ is the same as the surface magnetostatic wave number for the F slab. The other roots $q_x^{(2)}$ and $q_x^{(3)}$ correspond to bulk and highly attenuated surface modes, respectively, having no analog in the earlier magnetostatic case. The DESW are mixed eigenstates of these three types of waves. The degree of mode mixing can

be found by applying the appropriate boundary conditions at $x = 0$ and $-d$, as discussed in [16, 20, 39]. These calculations yield SW dispersion relations in the form of a modified magnetostatic surface mode and a series of quantized bulk modes.

1.5.3 Retarded SW modes or magnetic polaritons

In the previous two subsections we neglected retardation by using the magnetostatic form of Maxwell's equations because wave number $q_{\parallel} \gg \omega/c$, where c is the speed of light. Now we consider the SW excitations in a region where $q \sim \omega/c$. This is the so-called polariton regime where the SW couples to the photon of light to form a mixed mode. Bulk magnetic polaritons for a F material were first investigated by Auld [40]. Later the magnetic polaritons were investigated for AF [41, 24, 42] and for ferrimagnets [43]. An excellent review article for polaritons in planar geometries can be found in [15].

To discuss the effects of retardation on the SW we need the full form of Maxwell's equations (in the absence of free charges and macroscopic currents) [14]:

$$\vec{\nabla} \cdot \vec{D} = 0, \;\; \vec{\nabla} \times \vec{E} = -\frac{\partial \vec{B}}{\partial t},$$
$$\vec{\nabla} \cdot \vec{B} = 0, \;\;\; \vec{\nabla} \times \vec{H} = \frac{\partial \vec{D}}{\partial t}, \tag{1.33}$$

in SI units. The magnetic induction $\vec{B}$ and the electric displacement $\vec{D}$ are

$$\vec{B} = \mu_0 \overleftrightarrow{\mu}(\omega)\vec{H}, \qquad \vec{D} = \epsilon_0 \overleftrightarrow{\epsilon}\vec{E}. \tag{1.34}$$

It follows from Eq. (1.15) that the dynamic response (at frequency ω) of a F or AF

material is characterized by a gyromagnetic permeability tensor [16]

$$\overleftrightarrow{\mu}(\omega) = \begin{pmatrix} \mu_1(\omega) & i\mu_2(\omega) & 0 \\ -i\mu_2(\omega) & \mu_1(\omega) & 0 \\ 0 & 0 & 1 \end{pmatrix}, \tag{1.35}$$

where $\mu_1 = 1 + (\chi^+ + \chi^-)/2$ and $\mu_2 = (\chi^+ - \chi^-)/2$. The dielectric response is usually taken to be a diagonal tensor of the form

$$\overleftrightarrow{\epsilon} = \begin{pmatrix} \epsilon & 0 & 0 \\ 0 & \epsilon & 0 \\ 0 & 0 & 1 \end{pmatrix}, \tag{1.36}$$

where ϵ is a frequency independent constant.

To discuss polaritons we can no longer use the magnetostatic scalar potential, but instead we must solve for the electric and magnetic field components. These have a plane-wave form $\exp(i\vec{q}.\vec{r})$ in an infinite medium, so the dispersion relations for bulk magnetic polaritons can be deduced from Eqs. (1.33) and (1.34) as [16]

$$\left(1 - \xi_1 \chi^+\right)\left(1 - \xi_1 \chi^-\right) = \xi_2^2 \chi^+ \chi^-, \tag{1.37}$$

where $\xi_1 = [(2\epsilon\omega^2/c^2) - q_x^2]/2[q^2 - (\epsilon\omega^2/c^2)]$ and $\xi_2 = q_x^2/2[q^2 - (\epsilon\omega^2/c^2)]$. On taking the limit of $q^2 \gg (\epsilon\omega^2/c^2)$, we recover the results for the bulk magnetostatic modes. For a finite material (with interfaces) the situation becomes complicated in general, due to coupling between electric and magnetic fields. However, for a planar geometry, it is well established (see e.g., [16, 29]) that the modes can be decoupled into transverse electric (TE) and transverse magnetic (TM) components. We shall see later that this separation does not necessarily hold for curved interfaces.

1.6   Experimental methods

There are several different experimental techniques for studying the bulk and surface SW in the different wavevector regions. The most commonly used techniques are magnetic resonance, particularly ferromagnetic resonance (FMR) and antiferromagnetic resonance (AFMR), inelastic light scattering (Brillouin and Raman scattering), attenuated total reflection (ATR) and inelastic neutron scattering (INS). The magnetic resonance and light scattering techniques are very effective for studying the SW excitations at relatively small wavevectors near the center of Brillouin zone. Depending on the magnetic material and/or the experimental setup, the wavevectors might correspond to either the magnetostatic or dipole-exchange regimes. By contrast, INS allows the study of SW properties for wavevectors throughout the Brillouin zone. However, the instrumental resolution may be less than in other techniques, and it is not surface-sensitive. ATR is an optical method that allows the study of the coupling of electromagnetic radiation (through an attenuated surface wave) to the surface SWs, and it is important for surface magnetic polaritons. Here we give a very brief description of these techniques.

Magnetic resonance (either FMR or AFMR) is a spectroscopic technique for probing the SW excitations, in which the precessional motion of the magnetic moments is utilized. This precession, which we discussed in Sec. 1.4, depends not only on the magnetic field strength (e.g., of the order of a Tesla), but also on the crystalline anisotropy, the demagnetization, and the exchange, as well as possible damping effects. In a FMR experiment the magnetic sample (e.g., a thin film) is placed between the poles of an electromagnet in a microwave resonant cavity and in an external transverse oscillating r.f. field. If the frequency of the oscillating magnetic field matches the SW frequency (typically in the microwave regime) at zero or very small wavevector, a resonant absorption of energy in the F material is observed. By varying the frequency of the oscillating r.f. field (or more conveniently
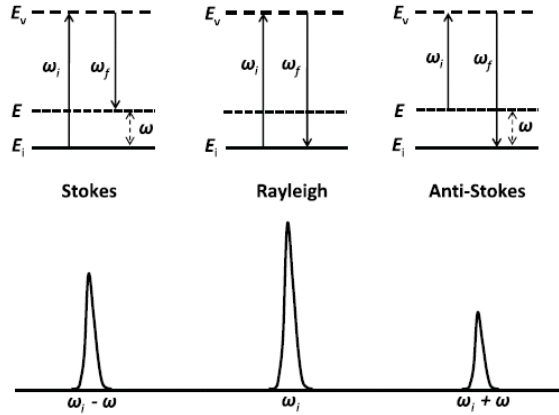
Figure 1.6: Schematic diagram of the light scattering processes, showing examples of energy-level schemes and spectral intensities.

by varying the static applied magnetic field) a series of resonance peaks corresponding to surface or standing bulk SW can be measured. The first FMR observation of bulk SW in Permalloy thin films was reported by Seavey *et al* [26], while Yu *et al* [44] investigated the surface SW in YIG using FMR. Reviews of magnetic resonance experiments can be found in [15, 45]. A disadvantage of the FMR technique is that it does not usually provide the wavevector dependence of the SW.

Light scattering has been used extensively to study bulk and surface excitations (including SW) where a photon interacts with an excitation. This interaction may involve elastic and inelastic scattering processes, and a schematic diagram is shown in Fig. 1.6. The Rayleigh peak represents elastic scattering of photons. In the more interesting process of inelastic scattering, a SW can be either created (Stokes process) or destroyed (anti-Stokes process), which leads to a change of energy and momentum between the incident and scattered photons. For a bulk material this can be described by the following conservation laws for energy and momentum

$$\hbar\vec{q_i} - \hbar\vec{q_f} = \pm\hbar\vec{q}, \qquad \hbar\omega_i - \hbar\omega_f = \pm\hbar\omega(\vec{q}). \qquad (1.38)$$

Here $\vec{q}_i$ ($\vec{q}_f$) and ω_i (ω_f) correspond to the wavevector and frequency of the incident (scattered) light, respectively. The plus and minus signs refer to the Stokes and anti-Stokes processes, respectively, in which a SW of wavevector $\vec{q}$ and frequency $\omega(\vec{q})$ is either created or destroyed. The intensity of a Stokes process is usually higher than that of the corresponding anti-Stokes process. For a bulk magnetic material the intensity ratios of the anti-Stokes to Stokes processes is typically weighted by the thermal factor of $\exp(-\hbar\omega/k_B T)$ [34, 36]. In a finite magnetic system the broken translational symmetry due to a surface leads to a spread of the wavevector components, which results in a frequency broadening of the intensity peaks in the scattering spectrum [16, 32].

The two main inelastic light scattering techniques are Brillouin light scattering (BLS) and Raman light scattering (RLS). The original BLS experiment for acoustic phonons (sound waves) was due to Brillouin in 1922, but it was much later before BLS was applied to bulk SW in YIG [46] and surface SW in EuO [47]. The RLS technique was developed by Raman and (independently) by Landsberg in 1928. The first RLS to probe SW excitations was for FeF_2 [48]. In BLS or RLS from a magnetic sample, only a very small fraction of the incident photons are scattered by a SW. Also, because of the conservation laws in Eq. (1.38), it is easy to show that the SW wavevector $|\vec{q}|$ is small compared to the Brillouin zone boundary. The two experimental techniques differ in the method for detecting the scattered light and they apply to different ranges of SW frequency. In BLS the frequency shifts of the scattered light range up to about 5 cm^{-1} and are detected by a multipass Fabry-Pérot interferometer, whereas in RLS a frequency shift typically in the range 5 - 4000 cm^{-1} is recorded by a grating spectrometer. The conversion between the wavenumber units and frequency is 1 cm$^{-1} \equiv 30$ GHz. Typically BLS is appropriate for F materials, whereas RLS is used for the higher-frequency SW in AF materials. Excellent reviews of light scattering for the study of bulk and surface magnetic

excitations are found in [34, 46, 49, 50, 51, 52, 53, 54].

The ATR technique can be used to probe surface polaritons in finite magnetic systems [55, 56, 57], following earlier work by Otto [58] in 1968 for surface phonon polaritons. ATR utilizes the property of total internal reflection in an optically-dense external medium to form an evanescent wave in the magnetic sample. An evanescent wave is a penetrating electromagnetic field whose intensity decays with distance and may extend below the sample surface by (e.g.) about 1 μm. This field couples with a surface SW in the magnetic sample, resulting in a transfer of energy and a dip in the reflection coefficient of the light. A review is given in [16].

INS is another useful technique to probe the SW excitations and to characterize their dispersion properties in the Brillouin zone. Since neutrons interact very weakly with materials and have a large penetration depth, this method is useful for studying bulk SW but it is not for surface sensitive. Also the presence of Bragg peaks at low energies and small wavevectors reduces the resolution. Hence the optical techniques discussed above are more applicable for magnetic nanomaterials [34].

1.7   Outline of the thesis

We present a macroscopic continuum theory for SW excitations in cylindrical nanostructures. This work is motivated by the fabrication of submicron-sized high-density arrays of magnetic wires, tubes and rings (see, e.g., [59]) and their experimental studies mainly by BLS and FMR (see, e.g., [60]). Recent theoretical and experimental works show the importance of understanding the fundamental SW dynamics in these systems to develop the magnetic-based technologies (see e.g., [61, 62, 63, 64, 65, 66]). The aim in this thesis is to investigate the surface and bulk SW in cylindrical multilayer nanostructures in different wavevector regimes.

In Chapter 2 a detailed study of the magnetostatic modes in long F and AF nanotubes is presented. Results for wires and antiwires are deduced as special

cases. The surface and bulk SW are studied here for the situation where the dipole-dipole interactions are dominant in the spin dynamics. The dispersion relations are found for the magnetostatic SW modes, and numerical calculations are presented for materials such as Permalloy and MnF_2. Next, we generalize this theory for tubes to cylindrical multilayer systems consisting of a core surrounded by any arbitrary number of concentric tubular layers. Each layer may be magnetic (F or AF) or nonmagnetic. A transfer matrix approach is employed to calculate the dispersion relations for the mode frequencies and numerical examples are given.

Chapter 3 is devoted to study the surface and bulk magnetostatic modes in F / AF bilayers with a cylindrical geometry. The formalism for tubes in Chapter 2 is generalized by considering a F nanotube with its core now filled by an AF material, or vice-versa. The dispersion relations and the localization properties of the modes are shown to quite different from previous results for planar bilayers [67]. As an extension we also consider a cylindrical F / AF bilayers as two concentric tubes around a nonmagnetic core. Numerical examples for both of the bilayer geometries are obtained taking Permalloy or Ni (as the F) and $GdAlO_3$ (as the AF).

In Chapter 4 we concentrate on developing a theory for the localized surface and bulk magnetic polaritons in cylindrical tubes. This involves solving for the dynamical response using a non-diagonal susceptibility tensor for a F or AF and the full form of Maxwell's equations. In developing our theory for the propagation of the magnetic polaritons, the solutions are considered in terms of transverse electromagnetic (TEM) modes, since the separation into TE and TM modes is not usually possible for the cylindrical geometry. This allows us to recover our previous results for magnetostatic modes by taking the non-retarded limit of $q \gg \omega/c$. Numerical calculations are made for YIG and MnF_2 materials.

Chapter 5 deals with a theory for the dipole-exchange SW in cylindrical nanotubes, where the long range dipole-dipole interactions and the short range exchange

interactions may be comparable in the magnetization dynamics. Our calculations describe the radial and angular quantization of different modes in the nanotubes, and the dispersion relations for the dipole-exchange SW can be related to BLS experiments, as in Ni nanotubes [60]. For limiting special cases our calculations simplify to the one interface-geometries of dipole-exchange SW in wires [68] or antiwires. Numerical calculations are carried out for nanostructures of Ni and EuS including a phenomenological damping, and our results are compared with experimental data in [69].

In Chapter 6 we present a linear response theory of the magnetic Green's functions in a cylindrical tube, taking the magnetostatic regime for simplicity. This enables us to investigate the spectral intensities of the surface and bulk magnetostatic SW in the different cylindrical geometries. Numerical results are given to illustrate the behavior for both F (e.g., Ni) and AF (e.g., $GdAlO_3$) materials.

Each of Chapters 2 - 6 contains its own conclusions, but some overall conclusions are also given in Chapter 7, where we also indicate possible extensions.

CHAPTER 2

Magnetostatic Modes in Cylindrical Geometries: Tubes and Generalized Multilayered Systems

(Some of the results in this chapter have been published in [70] and [71])

2.1 Introduction

As mentioned briefly in Chapter 1, the static and dynamical properties of spin waves (SW) have attracted considerable attention in magnetic nanostructures with cylindrical geometries, both theoretically and experimentally and for device applications (see [32, 72]). These nanostructures have included metallic wires (e.g., [68, 69, 73]), disks (e.g., [32, 74]) and rings (e.g., [75, 76, 77]), both individually and in periodic arrays. The fabrication of Ni nanowires arrays and their characterization were reported by Nielsch *et al.* [78], using electrodeposition into highly ordered nanometer-sized cylindrical alumina templates with large length to diameter aspect ratios. Also, more recently, the fabrication of high-density arrays of magnetic nanotubes, which are essentially hollow cylinders composed of materials such as Ni or Permalloy, has been reported [59] and their SW have been probed by BLS and FMR techniques [60] as in Sec. 1.6. For the Ni nanotubes arrays used in [60], typical sizes correspond to 25 to 35 nm for the inner radius, 10 to 15 nm for the wall thickness, and length up to 200 nm. Potential applications include high-density storage devices, magnetic sensors, fast switching devices, etc.

The above investigations have motivated us to develop analytic theories for the long-wavelength surface and bulk magnetostatic SW in cylindrical geometries, starting with nanotubes. Numerical applications are made for specific ferromagnetic (F) and antiferromagnetic (AF) materials. As discussed in Chapter 1, by consider-

ing the magnetostatic modes we are focusing on situations where the dipole-dipole interactions dominate in the *spin dynamics*. For this, the wave number along the symmetry axis of the nanotube must be sufficiently small (typically 10^7 m^{-1} or less), as can be achieved in BLS experiments if a 90^0 scattering geometry is employed. By contrast, the BLS experiment in [60] involved a 180^0 backscattering geometry giving a larger wave number that corresponded to the dipole-exchange region.

Over the last few years magnetic multilayers have received much attention due to their fundamental physics and technological applications. Theoretical investigations of dipolar SW in F and AF multilayers, grown with nonmagnetic spacer layers, have been of interest following seminal work by Mika and Grünberg [79] among others. The basic techniques involve either employing a transfer matrix approach or directly applying Bloch's theorem over a periodic length (see, e.g., [61, 80] for reviews). Experimentally, the nanostructures have been grown by electrodeposition and their SW excitations studied by FMR and BLS techniques. (see, e.g., [16, 81]). So far most theoretical and experimental attention has been given to planar systems with an arrangement of the layers that may be either periodic, quasiperiodic (e.g., in a Fibonacci sequence), or arbitrary [80].

In order to investigate the effects of curved surfaces and interfaces in magnetic multilayers, a comprehensive theory for the dipolar spin waves in long cylindrical geometries is presented here. The theories of the spin dynamics in magnetic wires [82] and tubes, for which there are just one or two interfaces respectively, are generalized later in this chapter to structures consisting of a core surrounded by any arbitrary number of concentric layers (or tubes). Each layer may be magnetic (either F or AF) or a nonmagnetic spacer. The long-range dipolar fields provide coupling between magnetic layers across the spacer regions, resulting in a coupling between the dipolar modes of the system. Several branches of coupled SW, having frequencies and localization that may be controlled by the structural properties, are found.

The focus is on the localized interface modes, which are shown to be strongly modified (for example, in their frequency and wave number cutoff) by the multilayer structure, compared to the behaviour in single magnetic wires and tubes.

We first present the theoretical model for cylindrical nanotubes in Sec. 2.2, where a large length-to-radius aspect ratio is assumed (allowing end effects to be ignored). The external magnetic field and static magnetization (or sublattice magnetization) are taken parallel to the symmetry axis of the tube. The characteristic equations (or dispersion relations) for the surface and bulk SW modes, derived by applying the standard electromagnetic boundary conditions at the two interfaces of a nanotube, are described. Some special limiting cases are also discussed. For the numerical solutions given in Sec. 2.3, both F (using $Ni_{80}Fe_{20}$) and AF (using MnF_2) materials are employed to illustrate the dispersion relations and the radial amplitudes for the different modes. Sec. 2.4 describes a generalization of the theory to the cylindrical multilayer structures. Here we employ our previous analysis as in Sec. 2.2, together with a transfer matrix approach, to derive the theoretical dispersion relations. Numerical examples are given in Sec. 2.5, choosing Ni and $GdAlO_3$ as the magnetic materials. Finally, a summary of this chapter is given in Sec. 2.6.

2.2   General theory of magnetostatic modes in tubes

A model of a nanotube is shown in Fig. 2.1 as a long hollow cylinder with inner and outer radii R_1 and R_2, respectively. The magnetic material fills the region $R_1 < r < R_2$, whereas a nonmagnetic material occupies $r < R_1$ and $r > R_2$. The theory is developed for general values of R_1 and R_2, contrasting with [86] where a magnetostatic theory of nanotubes with negligible wall thickness ($R_1 \approx R_2$) was developed. Our calculations incorporate two limiting cases, one for a nanowire (when $R_1 \to 0$, $R_2 \neq 0$) and the other for an anti-nanowire (when $R_1 \neq 0$, $R_2 \to \infty$).

In Fig. 2.1 the symmetry axis of the tube, the direction of external magnetic
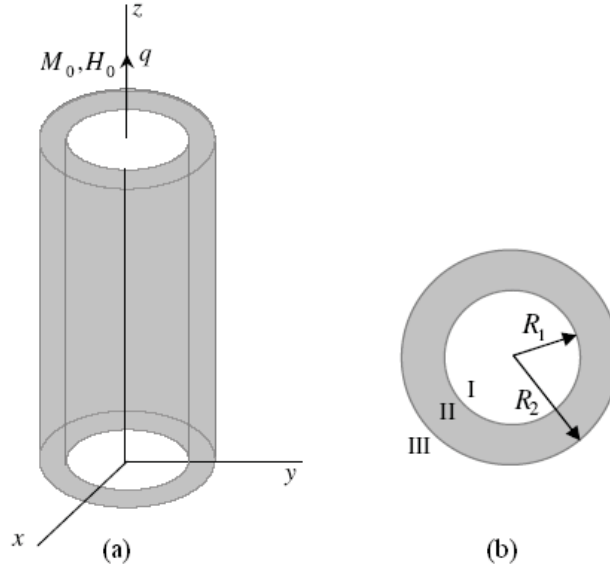
Figure 2.1: (a) A magnetic nanotube with static magnetization M_0, external magnetic field H_0 and propagation wave number q along the z axis, and (b) its cross section. The magnetic material fills region II whereas a nonmagnetic material is in I and III.

field H_0 and static magnetization M_0 for a F (or sublattice magnetization for an AF) coincide with the z axis. When a magnetic mode of an appropriate wave number is excited in the nanotube, the precession of the magnetization creates an internal dipolar magnetic field in the magnetostatic approximation. The linear response between the components of the fluctuating magnetization and the corresponding fluctuating field is given by the well-known frequency dependent susceptibility tensor $\overset{\leftrightarrow}{\chi}$ (see [39, 82, 83]), which we introduced in Sec. 1.4. The diagonal and non-diagonal frequency dependent tensor components are respectively of the form

$$\chi_{xx} = \chi_{yy} = \frac{1}{2}(\chi^+ + \chi^-) \equiv \chi_a \,, \quad \chi_{xy} = -\chi_{yx} = \frac{i}{2}(\chi^+ - \chi^-) \equiv i\chi_b. \quad (2.1)$$

For a F the explicit results (ignoring damping) are given in Eq. (1.16), where we defined ω as the angular frequency of the spin wave, while $\omega_0 = \gamma\mu_0 H_0$ and $\omega_m =$

$\gamma\mu_0 M_0$ are related to the external field and static magnetization, respectively (γ is the gyromagnetic ratio). The corresponding result for a uniaxial AF is slightly more complicated because of the two-sublattice structure, and is quoted in Eq. (1.18). In this case we defined the additional frequencies $\omega_A = \gamma\mu_0 H_A$ and $\omega_E = \gamma\mu_0 H_E$ (H_A and H_E are the effective fields related to the anisotropy and static exchange, respectively) and $\omega_{AF} = [\omega_A(2\omega_E + \omega_A)]^{1/2}$. The poles for ω in the F and AF cases occur at $\pm\omega_0$ and $\pm(\omega_{AF} \pm \omega_0)$, where ω_0 and ω_{AF} are the FMR and AFMR frequencies, respectively.

Our calculations for the nanotube proceed by following an approach analogous to that used for a solid wire (e.g., [82]), where the appropriate Maxwell's equations for the fluctuating fields are re-expressed in terms of the magnetostatic scalar potential $\Psi(r, \theta, z)$. This satisfies the Walker equation (see also Sec. 1.5)

$$\frac{\partial^2 \Psi}{\partial r^2} + \frac{1}{r}\frac{\partial \Psi}{\partial r} + \frac{1}{r^2}\frac{\partial^2 \Psi}{\partial \theta^2} + \nu(\omega)\frac{\partial^2 \Psi}{\partial z^2} = 0 \tag{2.2}$$

inside the magnetic medium, where we denote $\nu(\omega) = 1/[1+\chi_a(\omega)]$, and the Laplace equation outside (replacing $\nu(\omega)$ by unity). From the cylindrical symmetry, the solutions of both equations have the form

$$\Psi(r, \theta, z) = \psi(r)\exp[i(n\theta + qz)], \tag{2.3}$$

where q is the wave number of the magnetostatic mode along the z axis (consistent with Bloch's theorem [16]) and n is an integer ($n = 0, \pm1, \pm2, \ldots$) for Ψ to be a single-valued function of θ. The equation satisfied by $\psi(r)$ inside the magnetic material ($R_1 < r < R_2$) becomes

$$\frac{d^2\psi(r)}{dr^2} + \frac{1}{r}\frac{d\psi(r)}{dr} - \left\{\frac{n^2}{r^2} + \nu(\omega)q^2\right\}\psi(r) = 0. \tag{2.4}$$

If $\nu(\omega) > 0$, this has solutions that are formed from a superposition of two kinds of modified Bessel functions [84] and we write

$$\psi(r) = a_2 I_n\{\sqrt{\nu(\omega)}qr\} + b_2 K_n\{\sqrt{\nu(\omega)}qr\}, \tag{2.5}$$

where a_2 and b_2 are constants. However, if $\nu(\omega) < 0$, the solutions of Eq. (2.4) are expressible in terms of Bessel functions J_n and Y_n (see [84]). Denoting $\nu_0(\omega) = -\nu(\omega) > 0$ in this case, we have

$$\psi(r) = c_2 J_n\{\sqrt{\nu_0(\omega)}qr\} + d_2 Y_n\{\sqrt{\nu_0(\omega)}qr\}, \tag{2.6}$$

where c_2 and d_2 are constants. By contrast, the radial part of the potential $\psi(r)$ in the region $r < R_1$ always involves a modified Bessel function, i.e.,

$$\psi(r) = a_1 I_n(qr), \tag{2.7}$$

which increases with r. Similarly, $\psi(r)$ in the region $r > R_2$ has the form of another modified Bessel function, i.e.,

$$\psi(r) = a_3 K_n(qr). \tag{2.8}$$

The choices of modified Bessel functions in Eqs. (2.7) and (2.8) are consistent with the required asymptotic behaviour as $r \to 0$ and as $r \to \infty$, respectively.

Clearly the physical form of the solutions depend on the sign of $\nu(\omega)$ and hence on the value of ω. If $\nu(\omega) < 0$ the Bessel functions J_n and Y_n inside the magnetic material are oscillatory, and we associate this case with bulk-like modes. If $\nu(\omega) > 0$ the modified Bessel functions I_n and K_n inside the magnetic material have decay-like characteristics associated with localized surface modes. Fig. 2.2 shows the variation of $\nu(\omega)$ with ω in case of a F material. From the sign of $\nu(\omega)$
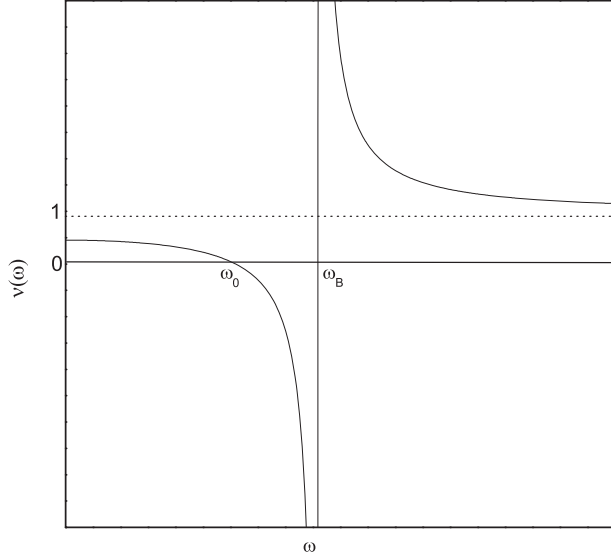
Figure 2.2: Schematic plot of $\nu(\omega)$ vs. ω for a F material showing the frequency regions where $\nu(\omega) > 0$ and $\nu(\omega) < 0$.

we deduce that the localized surface modes can exist only in the regions $0 < \omega < \omega_0$ or $\omega > \omega_B$, and the bulk magnetostatic modes can occur for $\omega_0 < \omega < \omega_B$, where

$$\omega_B = \left[\omega_0{}^2 + \omega_0\omega_m\right]^{\frac{1}{2}}. \tag{2.9}$$

Similarly, we show $\nu(\omega)$ versus ω for AF materials in Fig. 2.3 taking the general case of $H_0 \neq 0$. Here there are two regions where $\nu(\omega) < 0$, corresponding to the split bulk bands of an AF, while there are three regions with $\nu(\omega) > 0$ where (in principle) surface modes may be found. Specifically, the surface modes are restricted to the regions $0 < \omega < \omega_{AF} - \omega_0$, $\omega_{B1} < \omega < \omega_{AF} + \omega_0$ or $\omega > \omega_{B2}$, where

$$\omega_{B1},\ \omega_{B2} = \left[(\omega_{AF}{}^2 + \omega_0{}^2 + \omega_A\omega_m) \mp \{(\omega_A\omega_m)^2 + 4\omega_0{}^2(\omega_{AF}{}^2 + \omega_A\omega_m)\}^{\frac{1}{2}}\right]^{\frac{1}{2}}. \tag{2.10}$$

Likewise, it is concluded that the bulk modes can occur in the frequency regions
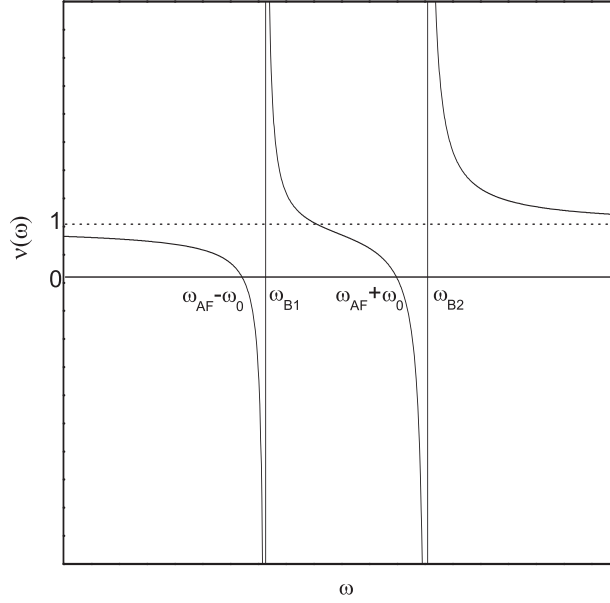
Figure 2.3: Same as Fig. 2.2 but for an AF material when $H_0 \neq 0$.

$\omega_{AF} - \omega_0 < \omega < \omega_{B1}$ and $\omega_{AF} + \omega_0 < \omega < \omega_{B2}$. In the special case of $H_0 = 0$, Fig. 2.3 simplifies with the two bulk bands collapsing into one, giving a behaviour that is qualitatively similar to Fig. 2.2.

First we consider the surface modes for either F or AF materials. The four unknown coefficients a_2, b_2, a_1 and a_3 introduced in Eqs. (2.5), (2.7) and (2.8) can be eliminated by applying the standard electromagnetic boundary conditions at $r = R_1$ and R_2 [16]. One condition ensures that ψ must be continuous at each interface of the nanotube. The other condition at each interface implies that $\{(1 + \chi_a)\partial\Psi/\partial r + i\chi_b\partial\Psi/\partial\theta\}$ just inside the magnetic medium must equal $\partial\Psi/\partial r$ just outside the medium. These conditions result in four simultaneous linear equations, and the determinant of the four unknown coefficients must vanish, leading to the

"characteristic equation" for the surface mode in the form

$$
\begin{vmatrix}
I_n(qR_1) & -u_1 & -v_1 & 0 \\
I_n{}'(qR_1) & -u_1\Phi_{K1} & -v_1\Phi_{I1} & 0 \\
0 & u_2 & v_2 & K_n(qR_2) \\
0 & u_2\Phi_{K2} & v_2\Phi_{I2} & K_n{}'(qR_2)
\end{vmatrix} = 0 .
\tag{2.11}
$$

Here I_n' and K_n' denote the derivatives of the modified Bessel functions with respect to their argument, and

$$
u_i = K_n\{\sqrt{\nu(\omega)}qR_i\}, \qquad v_i = I_n\{\sqrt{\nu(\omega)}qR_i\},
$$

$$
\Phi_{Ki} = K_n'\{\sqrt{\nu(\omega)}qR_i\}/\sqrt{\nu(\omega)}K_n\{\sqrt{\nu(\omega)}qR_i\} - n\chi_b/qR_i,
$$

$$
\Phi_{Ii} = I_n'\{\sqrt{\nu(\omega)}qR_i\}/\sqrt{\nu(\omega)}I_n\{\sqrt{\nu(\omega)}qR_i\} - n\chi_b/qR_i,
\tag{2.12}
$$

for $i = 1$, 2. Apart from finding the dispersion relations, one can also deduce, from Eqs. (2.5), (2.7) and (2.8), the variation of the amplitude $\psi(r)$ of the surface modes in the radial direction r of the nanotube. Examples will be given later.

Similarly, in the case of the bulk modes (for either the F or AF materials), the four unknown coefficients c_2, d_2, a_1 and a_3 introduced in Eqs. (2.6), (2.7) and (2.8) can be eliminated by applying the electromagnetic boundary conditions (as stated earlier) at the R_1 and R_2 interfaces. The analogous result to Eq. (2.11) is

$$
\begin{vmatrix}
I_n(qR_1) & -r_1 & -s_1 & 0 \\
I_n{}'(qR_1) & -r_1\Phi_{Y1} & -s_1\Phi_{J1} & 0 \\
0 & r_2 & s_2 & K_n(qR_2) \\
0 & r_2\Phi_{Y2} & s_2\Phi_{J2} & K_n{}'(qR_2)
\end{vmatrix} = 0 ,
\tag{2.13}
$$

where (for $i = 1, 2$)

$$r_i = Y_n\{\sqrt{\nu_0(\omega)}qR_i\}, \qquad s_i = J_n\{\sqrt{\nu_0(\omega)}qR_i\},$$

$$\Phi_{Y1} = Y_n'\{\sqrt{\nu_0(\omega)}qR_i\}/\sqrt{\nu_0(\omega)}Y_n\{\sqrt{\nu_0(\omega)}qR_i\} - n\chi_b/qR_i,$$

$$\Phi_{J1} = J_n'\{\sqrt{\nu_0(\omega)}qR_i\}/\sqrt{\nu_0(\omega)}J_n\{\sqrt{\nu_0(\omega)}qR_i\} - n\chi_b/qR_i. \tag{2.14}$$

Again, the amplitude $\psi(r)$ of the bulk modes in F or AF nanotubes can be found as a function of r.

Before solving the dispersion relation Eqs. (2.11) and (2.13) numerically in Sec. 2.3, it is helpful to consider some special cases, either in terms of the geometry or the wave number q. First, the 4×4 determinantal condition in Eq. (2.11) simplifies and reduces to a 2×2 determinant when $R_1 \to 0$ (with $R_2 \neq 0$). It leads to the "characteristic equation" for the surface magnetostatic modes in a nanowire:

$$\{\sqrt{\nu(\omega)}\}^{-1}qR_2\frac{I_n'\{\sqrt{\nu(\omega)}qR_2\}}{I_n\{\sqrt{\nu(\omega)}qR_2\}} - qR_2\frac{K_n'(qR_2)}{K_n(qR_2)} + n\chi_b = 0. \tag{2.15}$$

An equation of this form was previously derived specifically for FM cylinders [68, 82]. Similarly, for the bulk modes in this case we find that Eq. (2.13) reduces to

$$\{\sqrt{\nu_0(\omega)}\}^{-1}qR_2\frac{J_n'\{\sqrt{\nu_0(\omega)}qR_2\}}{J_n\{\sqrt{\nu_0(\omega)}qR_2\}} - qR_2\frac{K_n'(qR_2)}{K_n(qR_2)} + n\chi_b = 0 \tag{2.16}$$

for a nanowire. On the other hand, taking the limit of $R_2 \to \infty$ in Eq. (2.11), we obtain a dispersion relation for the surface modes in an anti-wire of radius R_1 (i.e., a nonmagnetic cylinder embedded in a F or AF medium):

$$\{\sqrt{\nu(\omega)}\}^{-1}qR_1\frac{K_n'\{\sqrt{\nu(\omega)}qR_1\}}{K_n\{\sqrt{\nu(\omega)}qR_1\}} - qR_1\frac{I_n'(qR_1)}{I_n(qR_1)} + n\chi_b = 0. \tag{2.17}$$

An analogous expression for the dispersion relation of the bulk magnetostatic modes in an anti-nanowire can be deduced using Eq. (2.13).

For both the wire and the anti-wire structures, it is easily proved by taking the limit of $q \to 0$ in Eqs. (2.15) and (2.17) that the surface modes (consisting of one branch for each value of $|n|$ except $n = 0$) have a common frequency equal to $\omega_0 + \omega_m/2$ in the F case and $(\omega_{AF}^2 + \omega_A \omega_m)^{1/2} - \omega_0$ in the AF case at $q = 0$. When $n = 0$ there is no surface mode for any value of q, because the localization condition cannot be satisfied. Also, in the AF case, the surface mode exists only when $H_0 \neq 0$. When q is nonzero the surface mode frequency decreases monotonically (initially proportional to q^2) as q is increased until it reaches a cut-off at ω_B, representing the top of the bulk band in the F case, or ω_{B1}, representing the top of the lower bulk band in the AF case (see Eq. (2.10)). The cut-off value q_{max} increases with $|n|$ and is always larger for an anti-wire of radius R than for a wire of the same radius. For example, in the case of a F material with applied field such that $\omega_0 \gg \omega_m$, we find by expanding the modified Bessel functions that

$$q_{max}R \simeq \left\{ 2|n|(|n| \mp 1)\left(\frac{\omega_B}{\omega_0} - 1\right) \right\}^{1/2}, \qquad (|n| > 1), \qquad (2.18)$$

where the upper (lower) sign refers to the wire (anti-wire) structure.

In the case of the bulk modes of either a wire or an anti-wire, there are multiple branches (i.e., many solutions of the dispersion relation) for each $|n|$, including here $n = 0$, for each q value. We illustrate this property numerically later.

Next, we return to Eq. (2.11) for the surface modes of a general nanotube structure and consider how it simplifies for small q. This involves expanding the modified Bessel functions for small values of their arguments, assuming $qR_1 \ll 1$ and $qR_2 \ll 1$. We conclude that for small $q \neq 0$ there are now two surface modes with different frequencies for each nonzero value of $|n|$ and no localized surface modes when $n = 0$. When R_1 and R_2 are fairly well separated (i.e., in the case of large wall thickness), these two branches may be interpreted approximately as corresponding to one mode localized near the $r = R_1$ interface and the other near

the $r = R_2$ interface. However, this concept no longer applies when the walls are thin because of strong overlap effects. For the limit where $q \to 0$, the two surface mode frequencies in the nanotubes become degenerate and can be expressed as

$$\omega = \sqrt{(\omega_0 + \omega_m/2)^2 - \{(\omega_m/2)(R_1/R_2)^{|n|}\}^2} \tag{2.19}$$

in the F case. We note that this is different from the frequency of the surface modes at $q = 0$ in the special cases of a F wire or antiwire. In Eq. (2.19) the frequency depends on the quantum number n as well as on the radii R_1 and R_2. In a similar manner, the frequency of the surface modes in AF nanotubes (in nonzero applied field) when $q \to 0$ can be found. This behaviour for the dispersion relations will be illustrated later in the numerical calculations.

2.3   Numerical applications

Numerical applications are now presented for Permalloy ($Ni_{80}Fe_{20}$) in the F case and MnF_2 in the AF case to show the dispersion relations and the radial dependence of the amplitude for surface and bulk modes. The material parameters are $\mu_0 M_0 = 0.0645$ T (or $\omega_m/2\pi = 1.90$ GHz) for Permalloy [85], while for MnF_2 we have $\mu_0 M_0 = 0.754$ T (or $\omega_m/2\pi = 21.0$ GHz), $\mu_0 H_E = 55.0$ T (or $\omega_E/2\pi = 1530$ GHz) and $\mu_0 H_A = 0.787$ T (or $\omega_A/2\pi = 21.9$ GHz) [23].

2.3.1   Dispersion relations for the surface modes

In Fig. 2.4 the dispersion relations for surface magnetostatic modes in $Ni_{80}Fe_{20}$ nanowires and anti-nanowires of the same radius are compared, taking $\mu_0 H_0 = 0.6$ T. The mode frequencies are plotted against the dimensionless qR for the first two modes, i.e., $|n| = 1$ and 2. Consistent with our earlier discussion, the upper and lower bounds of the dispersion curves are $(\omega_0 + \omega_m/2)$ and ω_B, respectively, and these are plotted as the horizontal dashed lines. It is seen that the cut-off values
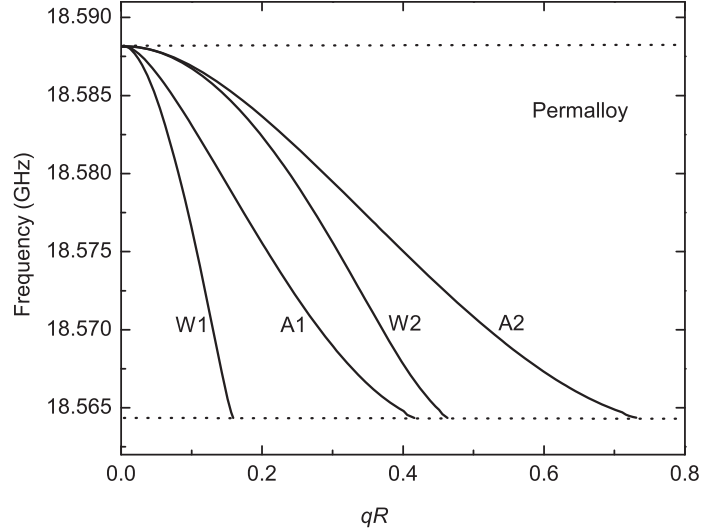
Figure 2.4: Frequencies of the surface modes in $Ni_{80}Fe_{20}$ wire and anti-wire geometries (radius R) versus dimensionless qR. The modes for the lowest two $|n|$ ($= 1$, 2) are labelled as W1 and W2, respectively, for the wire case and as A1 and A2 for the anti-wire case.

of qR are smaller for a wire than for an anti-wire, as mentioned earlier, and these values increase with $|n|$. In this example we have $\omega_0/\omega_m \simeq 9.30$, whereupon Eq. (2.18) yields approximate cut-off values for qR when $|n| = 2$ as 0.46 and 0.79 for the wire and anti-wire, respectively. These values are seen to be fairly close to the more accurate values found numerically in Fig. 2.4. No solutions for Eqs. (2.15) and (2.17) are found when $n = 0$. The group velocity $v_g = \partial\omega/\partial q$ of the surface magnetostatic modes in a wire or an anti-wire can also be deduced from the numerical dispersion relations. It depends on q and R as well as other parameters, and we estimate (for example, using Fig. 2.4 and $|n| = 1$) that the maximum values of $|v_g|$ is about 11 m/s in the wire case and 4 m/s in the anti-wire case when $R = 50$ nm. Qualitatively similar results are obtained for the frequencies of surface modes in wires and anti-wires of MnF_2.

We next focus on the numerical results for the surface magnetostatic modes in nanotubes, where effects due to the two interfaces play a role. In Fig. 2.5 we present
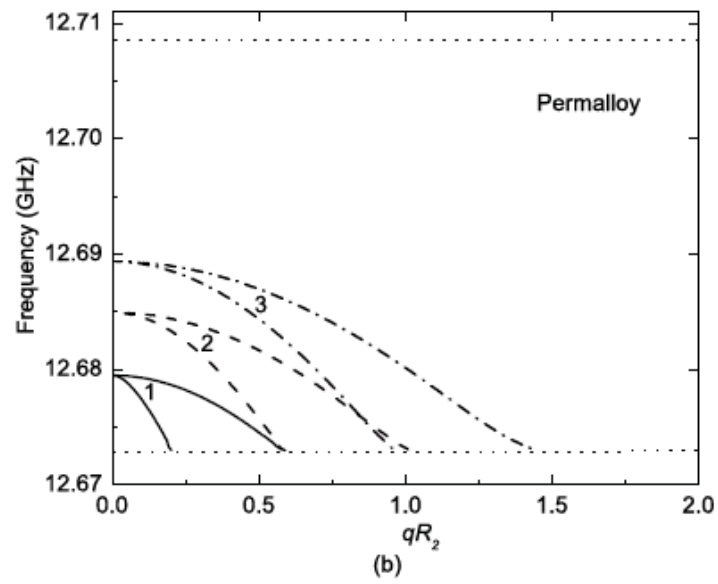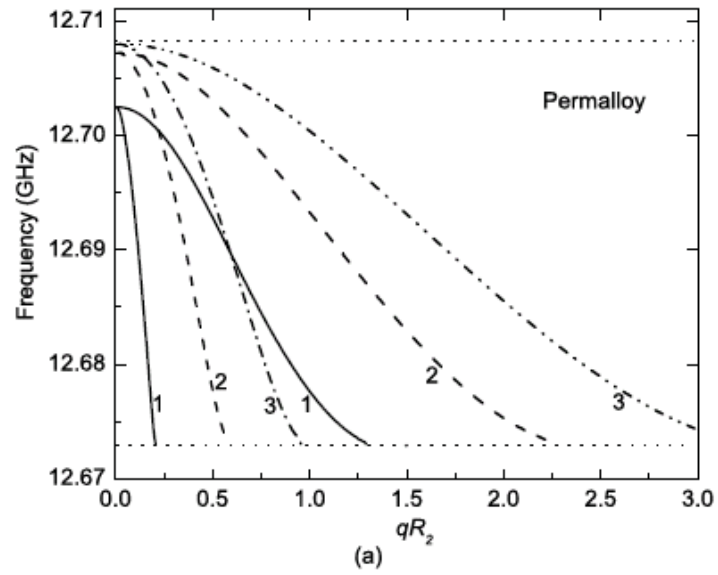
Figure 2.5: Frequencies of surface modes in a $Ni_{80}Fe_{20}$ nanotube versus qR_2. The first three $|n| = 1$, 2 and 3 modes are labeled as solid, dashed and chain lines for (a) $R_1/R_2 = 0.4$ and (b) $R_1/R_2 = 0.9$.
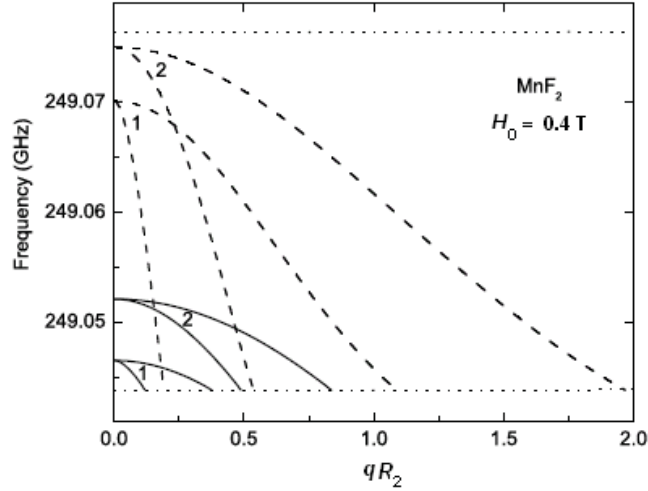
Figure 2.6: Dispersion relation for the surface modes in a MnF$_2$ nanotube. The first two $|n|$ modes are plotted as dashed lines for $R_1/R_2 = 0.4$ and solid lines for $R_1/R_2 = 0.9$.

the dispersion relations for a Ni$_{80}$Fe$_{20}$ nanotube, taking $\mu_0 H_0 = 0.4$ T. The surface mode frequencies are plotted here against the dimensionless qR_2 for $|n| = 1$, 2 and 3 (as labeled). They are again restricted to $(\omega_0 + \omega_m/2) < \omega < \omega_B$, and in Fig. 2.5 (and henceforth) these bounds are shown as horizontal lines. No numerical solution of Eq. (2.11) for the surface mode is found for $n = 0$. When $|n| \neq 0$ the maximum frequency always occurs at $q = 0$ and takes the values consistent with Eq. (2.19), i.e., it is reduced compared to the wire and anti-wire cases (where $R_1/R_2 \approx 0$). This reduction effect increases with $|n|$ and is less pronounced in Fig. 2.5(a) when $R_1/R_2 = 0.4$ compared to Fig. 2.5(b) when $R_1/R_2 = 0.9$. Also, as remarked earlier, for each $|n|$ there are now two branches in the dispersion curves when q is nonzero. Again, each branch exists only for q less than a cut-off value. The occurence of two branches is a direct consequence of the two interfaces.

Analogous calculations for the surface modes can be obtained for AF nan-
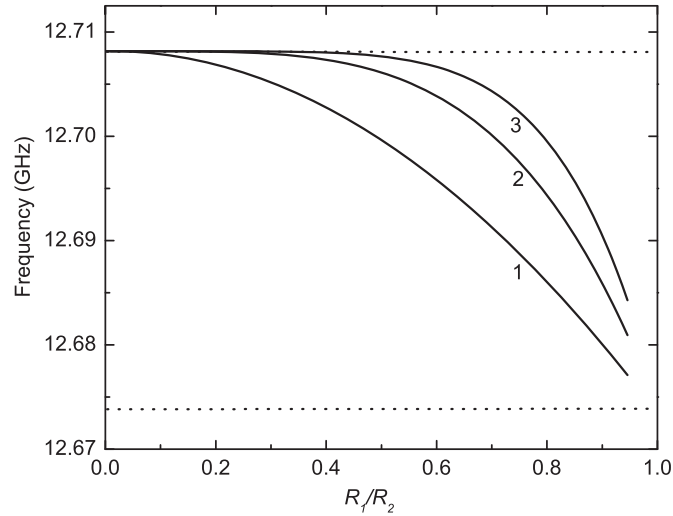
Figure 2.7:   Frequencies of surface modes in a $Ni_{80}Fe_{20}$ nanotube versus R_1/R_2 when $q = 0$, taking $|n| = 1$, 2 and 3.

otubes. As mentioned in Sec. 2.2 the frequencies lie in the range $(\omega^2_{AF} + \omega_m \omega_A)^{1/2} - \omega_0 > \omega > \omega_{B1}$, with the upper bound being achieved only when $R_1/R_2 \approx 0$. For localization to be satisfied, we required $H_0 \neq 0$ and $|n| \neq 0$. In Fig. 2.6 we illustrate the dispersion curves of the surface modes for a MnF_2 nanotube, where the frequencies for the lowest two values $|n| = 1$ and 2 are plotted versus qR_2 for two values of the ratio R_1/R_2. In most respects, the surface mode properties are qualitatively similar to those for F tubes.

The dependence of the surface mode frequencies on the wall thickness is of interest for both F and AF nanotubes. Numerical calculations for $Ni_{80}Fe_{20}$ nanotubes are presented in Fig. 2.7 where the frequencies for the $|n| = 1$, 2 and 3 surface modes at $q \approx 0$ are plotted against the ratio R_1/R_2 (which varies the wall thickness if R_2 is fixed). In this figure the two horizontal dotted lines represent the previously defined frequency bounds for the surface modes. When $R_1/R_2 \to 0$ and $q \approx 0$, all modes are degenerate at $(\omega_0 + \omega_m/2)$, as for a F wire or anti-wire. As $R_1 \to R_2$, all these
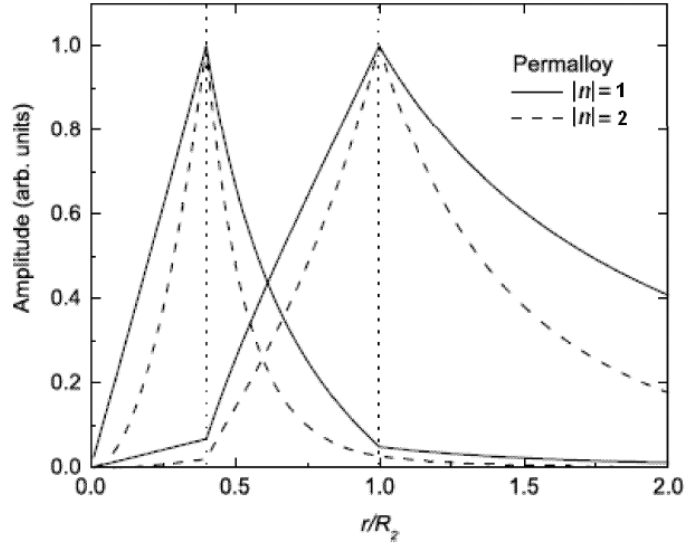
Figure 2.8: The amplitude $|\psi(r)|$ of the surface modes at $\omega/2\pi = 12.69$ GHz plotted against r/R_2 for a $Ni_{80}Fe_{20}$ nanotube. The two interfaces correspond to the vertical dotted lines.

modes become closer in frequency and collapse towards ω_B, which is consistent with the behaviour predicted in [86] for F nanotubes with negligible wall thickness.

The variations of $\psi(r)$ for the surface modes with the radial distance r have also been studied. For brevity our numerical calculations are presented only for $Ni_{80}Fe_{20}$, but we find similar results for MnF_2. Using the expressions for $\psi(r)$ in Sec. 2.2, together with the numerical values for the mode frequencies, we deduce the results shown in Fig. 2.8 for the surface modes. Here we have chosen the inner and outer radii of the nanotube as 20 nm and 50 nm, respectively. To obtain the amplitudes of any surface mode, the corresponding mode frequency and the qR_2 value are found from the dispersion curves (again with $\mu_0 H_0 = 0.4$ T). For a surface mode with $\omega/2\pi = 12.69$ GHz and using Fig. 2.5(a), the qR_2 values are 0.12 and 0.59 for $|n| = 1$, and 0.36 and 1.15 for $|n| = 2$. In Fig. 2.8 the dependence of $|\psi(r)|$ for the surface modes on r/R_2 is shown. Here the mode amplitudes are localized near the two interfaces and decay with distance from the interfaces. The modes
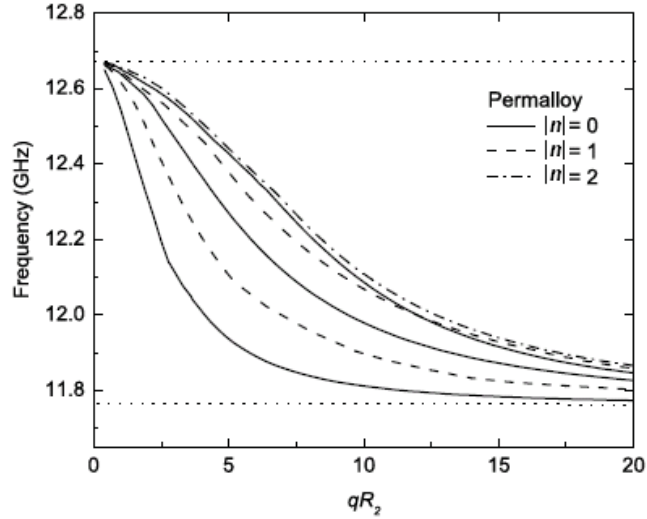
Figure 2.9: The dispersion relations for the lowest six branches of $|n| = 0$, 1 and 2 bulk magnetostatic modes in the $Ni_{80}Fe_{20}$ nanotube.

with larger $|n|$ are more strongly localized near the inner and outer interfaces than those with small $|n|$.

2.3.2   Dispersion relations for the bulk modes

The dispersion relations for the bulk magnetostatic modes are similarly obtained by solving Eq. (2.13) numerically. It is convenient to proceed directly to the bulk modes in nanotubes, since the general properties for wires, anti-wires and tubes are qualitatively rather similar. Previously we deduced that for F materials the bulk modes correspond to $\omega_0 < \omega < \omega_B$. For $Ni_{80}Fe_{20}$ with $\mu_0 H_0 = 0.4$ T this gives a frequency range from 11.76 GHz to 12.67 GHz. In Fig. 2.9 these upper and lower bounds are represented by the horizontal dashed lines, while the frequencies of the lowest six bulk-mode branches are plotted against qR_2 within this frequency range. As indicated, three of these branches correspond to $|n| = 0$, two to $|n| = 1$, and one to $|n| = 2$. There are, in fact, multiple bulk-mode branches corresponding
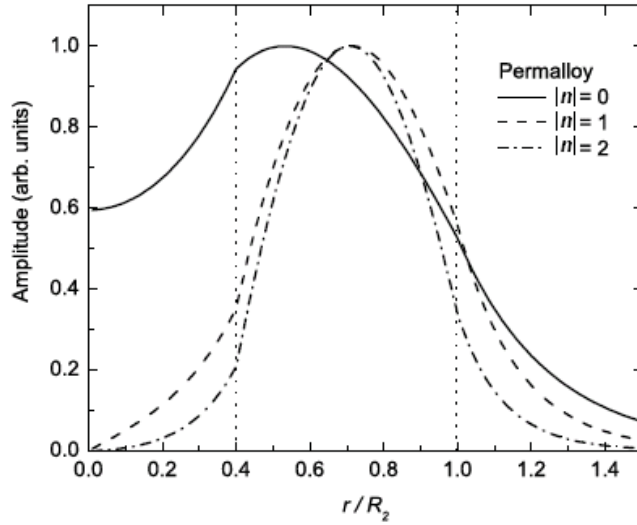
Figure 2.10: Same as Fig. 2.8 but for the bulk modes in a $Ni_{80}Fe_{20}$ nanotube at $\omega/2\pi$ = 12.1 GHz.

to each value of $|n|$, depending on how many nodes of the Bessel function occur between $r = R_1$ and $r = R_2$. The general behaviour is that the frequency increases with $|n|$ and with the number of nodes. Each bulk mode decreases in frequency with increasing qR_2 and eventually approaches the lower bound of the bulk mode. However, there is no frequency cut-off in the dispersion curves even for large qR_2, since there is no localization condition. The group velocities of the bulk modes can be deduced from the slope of the dispersion curves. For example, for the $R_2 = 50$ nm $Ni_{80}Fe_{20}$ nanotube in Fig. 2.9 the maximum $|v_g|$ occurs for the lowest frequency branch of the $|n| = 0$ mode, and it is of order 500 ms^{-1}.

The dispersion relations of the bulk magnetostatic modes in AF nanotubes can also be investigated numerically. The behaviour is quantitatively similar to the above F case, except that they occur within two frequency regions (i.e., $\omega_{AF} - \omega_0 < \omega < \omega_{B1}$ and $\omega_{AF} + \omega_0 < \omega < \omega_{B2}$) when an applied field is present.

Numerical results for $\psi(r)$ versus r have been obtained for the bulk modes, and
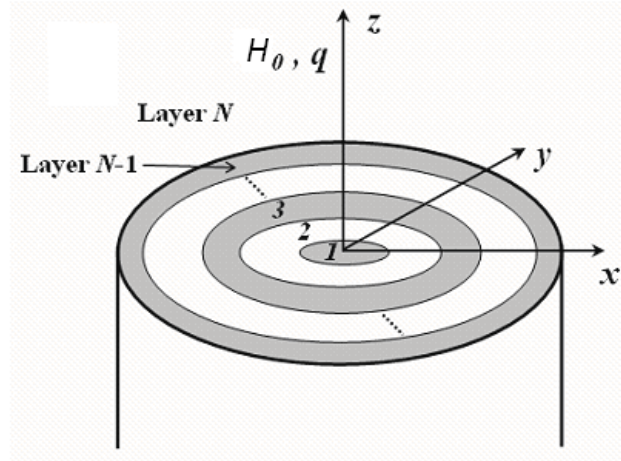
Figure 2.11:   A cylindrical multilayer geometry, where the magnetic layers (shown shaded) alternate here with nonmagnetic spacer layers. The applied field H_0 and wave number q are along the z-axis. The numbering of layers from 1 to N is indicated.

in Fig. 2.10 we illustrate this for the $Ni_{80}Fe_{20}$ nanotube used in Fig. 2.9. Selecting a bulk mode with $\omega/2\pi = 12.1$ GHz, the qR_2 values for the lowest branch of each $|n|$ are found from the dispersion curves as 3.12 for $|n| = 0$, 5.15 for $|n| = 1$, and 11.17 for $|n| = 2$. By contrast with the surface mode amplitudes in Fig. 2.8, it can be seen from Fig. 2.10 that the bulk modes are not localized at the interfaces but vary with r between the interfaces in an oscillatory fashion. In effect, a standing wave is formed within the wall thickness of the tube.

2.4   Outline of theory for multilayers

The system consists of a long cylindrical core of radius R_1 surrounded by an arbitrary number of cylindrical tubes, so that the interfaces occur at radial values $\{R_1, R_2, R_3, \cdots, R_{N-1}\}$ where the outermost layer N extends from R_{N-1} to infinity. Each layer, including the core, may be either magnetic (a F or AF layer) or nonmagnetic (a spacer layer). The layers are labeled with integers from 1 (the core)

to N, and a typical example is depicted in Fig. 2.11 where there is a magnetic core surrounded by alternating spacer and magnetic layers. To consider the dipolar (or magnetostatic) modes we again assume the long-range dipole-dipole interactions to be dominant in the spin dynamics. As in Sec. 2.2 for a single magnetic tube, we employ a non-diagonal magnetic susceptibility tensor for each magnetic layer. The z axis coincides with the direction of the applied field H_0 and the saturation magnetization M_0. Therefore the diagonal and off-diagonal frequency-dependent tensor components χ_a and χ_b are the same as before.

To describe the coupled magnetic modes, we extend the transfer matrix formalism, as previously employed for planar geometries (see, e.g., [80, 87, 88]), to apply to the cylindrical multilayers. Following our calculations for a magnetic tube, the appropriate Maxwell's equations are first re-expressed in terms of the magnetostatic scalar potential Ψ , which satisfies the Walker equation inside any magnetic layer and Laplace's equation in a nonmagnetic layer. The solution in the layer with label m has the form $\psi_m(r) \exp[i(n\theta + qz)]$ similar to Eq. (2.3) with

$$\psi_m(r) = \left\{ a_m I_n(\alpha_m qr) + b_m K_n(\alpha_m qr) \right\} \tag{2.20}$$

in cylindrical polar coordinates, where n is an integer. These solutions involve the Bessel functions $I_n(\alpha_m qr)$ and $K_n(\alpha_m qr)$. Here $\alpha_m = \{\nu_m(\omega)\}^{1/2}$ is a ω-dependent parameter related to the diagonal susceptibility component for the mth layer. It is real or imaginary corresponding to surface modes (localized near an interface) or propagating bulk modes, respectively. In any nonmagnetic layer, $\alpha_m = 1$.

The usual magnetostatic boundary conditions may next be applied in terms of the scalar potential (see Sec. 2.2). Thus, at the interface $r = R_m$ between layers m and $m+1$, we eventually obtain, using the susceptibilities for the F or AF case, a

matrix relationship between the respective a and b coefficients:

$$\begin{pmatrix} a_m \\ b_m \end{pmatrix} = \mathbf{T_m} \begin{pmatrix} a_{m+1} \\ b_{m+1} \end{pmatrix}, \tag{2.21}$$

where $\mathbf{T_m}$ is the 2×2 transfer matrix for that interface. It can be obtained from $\mathbf{T_m} = [S_m(R_m)]^{-1}[S_{m+1}(R_m)]$, where for layer m and any interface p we have

$$S_m(R_p) = \begin{pmatrix} I_n(\alpha_m q R_p) & K_n(\alpha_m q R_p) \\ \Phi_{Im}(R_p) & \Phi_{Km}(R_p) \end{pmatrix}, \tag{2.22}$$

with

$$\Phi_{Im}(R_p) = \frac{q R_p}{\alpha_m} I'_n(\alpha_m q R_p) - n \chi_{bm} I_n(\alpha_m q R_p). \tag{2.23}$$

An analogous definition is made for the quantity $\Phi_{Km}(R_p)$ in terms of the Bessel function K. The above results apply for both F and AF materials. The repeated application of Eq. (2.21) leads to

$$\begin{pmatrix} a_1 \\ b_1 \end{pmatrix} = \mathbf{T} \begin{pmatrix} a_N \\ b_N \end{pmatrix}, \tag{2.24}$$

where the overall transfer matrix for the multilayer is given by $\mathbf{T} = \mathbf{T_1 T_2} \ldots \mathbf{T_{N-1}}$. Finally, on using $b_1 = 0$ and $a_N = 0$ for the coefficients in the first and last layers (which are conditions for the solutions to be well behaved as $r \to 0$ and $r \to \infty$, respectively), it follows from Eq. (2.24) that $T_{22}(q, \omega) = 0$.

The vanishing of this matrix element of $\mathbf{T}$ constitutes an implicit dispersion relation for the frequencies ω of the dipolar modes at wave number q. For the cases of cylindrical systems with one or two interfaces, it can be explicitly verified that the above condition reduces to the previous results for wires (see Eq. (2.15)) and
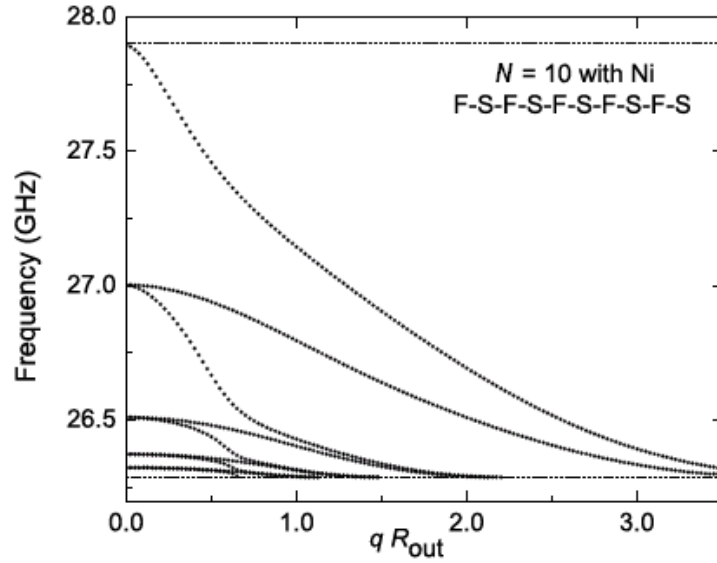
Figure 2.12: Calculated dispersion relations for the coupled dipolar modes, showing frequency versus qR_{out} in a multilayer with $N = 10$ and the structure indicated. The radii are chosen as $R_1 = 40$, $R_2 = 60$, $R_3 = 80$, $R_4 = 100$, $R_5 = 120$, $R_6 = 140$, $R_7 = 160$, $R_8 = 180$, $R_9 = R_{out} = 200$ (all in nm), while $\mu_0 H_0 = 0.6$ T and $|n| = 1$. The horizontal lines indicate the upper and lower boundaries for localized modes. See the text for other values.

tubes (see Eq. (2.11)). More generally, it can be solved numerically for systems with any finite number of interfaces. In the following section we present examples where the magnetic layers (which may be of different thickness and composed of the same or different materials) are separated by spacers.

2.5   Numerical results and applications

Calculations are now presented for multilayers in which the magnetic layers alternate with spacer layers (S). This is as shown in Fig. 2.11, except that in general the core region may be either magnetic or a spacer. The magnetic layers may be all F, where we use Ni as an example, all AF, with $GdAlO_3$ as an example, or a combination that includes some F and AF layers. Starting with the F case, results

for the SW frequencies versus the dimensionless qR_{out} (where $R_{out} = R_{N-1}$ denotes the outermost interface) are shown in Fig. 2.12. Here $N = 10$ and the F layers, chosen as Ni, correspond to saturation magnetization $M_S = 0.048$ T (or $\omega_m/2\pi = 18.7$ GHz) and $\gamma = 30.9$ GHz/T (see, e.g., [60]), as well as $\mu_0 H_0 = 0.6$ T. Specifically we assume here a structure with a Ni wire as core and four Ni tubes surrounding it (with intervening spacers). For simplicity, dispersion curves are shown only for the localized surface (or interface) SW for which there are nine branches in the present case, but there are also bulk SW manifolds that can occur outside the region indicated by the horizontal dashed lines. The modes shown in Fig. 2.12 have an angular dependence corresponding to $|n| = 1$. We note that all dispersion curves have a negative slope and a cut-off at large q, which are general characteristics shared by the interface modes for individual tubes [70]. The negative slope implies that the group velocity is negative (i.e., propagation is in the opposite direction to q). This is also found in certain other magnetostatic cases (see [15] for an example in a planar film geometry). The highest-frequency branch in the present case is the one localized near the R_1 interface of the Ni core. The other coupled modes are all associated mainly with the surrounding Ni tubes and occur in pairs (for the two interfaces) that become degenerate in the small q limit.

For comparison, we show another F example in Fig. 2.13, where the core region is now a spacer. Taking $N = 7$, we also include the dispersion curves for $|n| = 2$, as well as $|n| = 1$. In general, a larger value of $|n|$ means a more rapid variation of the fluctuating magnetization with the azimuthal angle θ, which in turn leads to a higher frequency (for a given q). This is seen to be the case in Fig. 2.13. Also, because the core is nonmagnetic (by contrast with the case in Fig. 2.12), the highest-frequency modes occur as a pair (becoming degenerate as $q \to 0$) and are mainly associated with the two interfaces of the innermost Ni tube. Fig. 2.14 shows some similar calculations made for AF multilayers using $GdAlO_3$. This material has
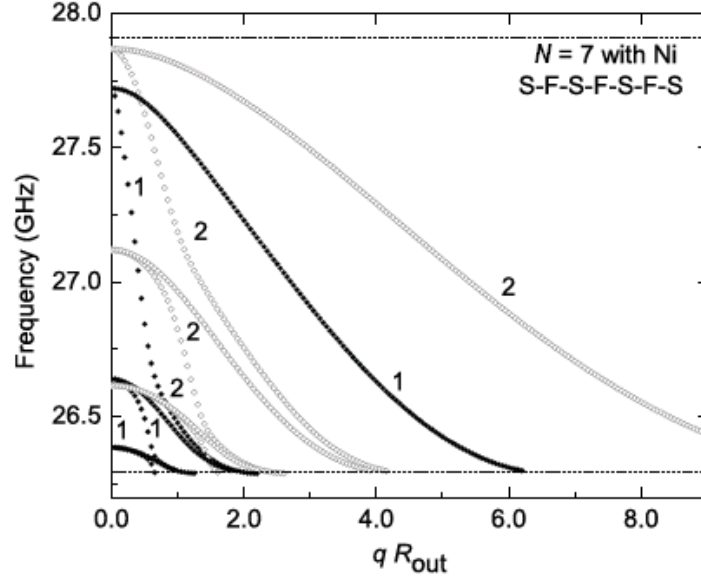
Figure 2.13: As in Fig. 2.12, but for a F multilayer with $N = 7$ and the structure indicated. The radii are chosen as $R_1 = 20$, $R_2 = 40$, $R_3 = 50$, $R_4 = 70$, $R_5 = 80$, $R_6 = R_{out} = 100$ (all in nm), and $\mu_0 H_0 = 0.6$ T. Here we show results for $|n| = 1$ (filled circles) and $|n| = 2$ (open circles), as labeled. See the text for other values.

a weak uniaxial anisotropy, so the mode frequencies are in the microwave region and are comparable with those for typical ferromagnets. The relevant parameters are $\omega_m/2\pi = 22.0$ GHz, $\omega_A/2\pi = 10.2$ GHz, and $\omega_{Ex}/2\pi = 52.6$ GHz (see, e.g., [23]), which imply a relatively low AFMR value of $\omega_{AF}/2\pi = 34.4$ GHz. The interface modes in AF wires and tubes occur only when $H_0 \neq 0$, as a necessary condition for localization, and they lie within a narrow frequency interval (defined by the horizontal lines in Fig. 2.14) that starts above $\omega_{AF} - \omega_0$. Here we take $\mu_0 H_0 = 0.7$ T for a multilayer with $N = 6$ corresponding to an AF core with two surrounding AF tubes separated by spacers.

It can be seen that qualitatively the behaviour is rather similar to that in Fig. 2.12 for the F structure, except that there are fewer interfaces (and therefore fewer localized modes) in the present case. We have also made calculations for other
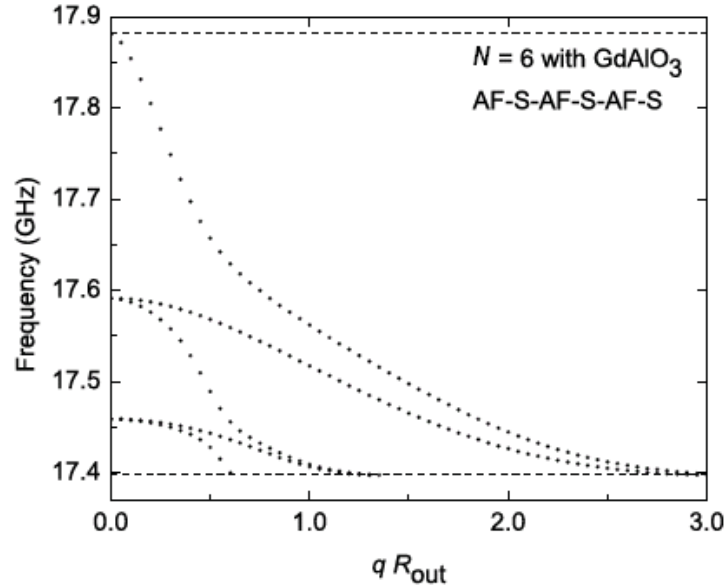
Figure 2.14: As in Fig. 2.12, but for an AF multilayer with $N = 6$ and the structure indicated. The radii are chosen as $R_1 = 25$, $R_2 = 35$, $R_3 = 60$, $R_4 = 75$, $R_5 = R_{out} = 100$ (all in nm), while $\mu_0 H_0 = 0.7$ T and $|n| = 1$. See the text for other values.

choices of the AF material. For example, in MnF_2 the AFMR frequency is much larger, so as a consequence the SW occur at a much higher frequency range ($\sim$ 250 GHz) and in a very narrow band of width ~ 0.04 GHz. Finally, in Fig. 2.15 we present calculations of the dispersion relations for a multilayer in which there are both F and AF layers, again using Ni and $GdAlO_3$ to illustrate the behaviour. Specifically, the structure has an AF tube separated by spacers from an inner F core and an outer F tube, which together are expected to provide a magnetically polarizing effect on the AF. There are now found to be two regions of frequency in which the localized modes may occur. In Fig. 2.15, which is obtained using $\mu_0 H_0$ = 0.1 T, the upper and lower regions are broadly characteristic of the AF and F materials, respectively. The SW of the coupled system (see the filled circles) occur as two branches in the upper region and three in the lower region. This might be expected when the two frequency regions are non-overlapping and fairly well
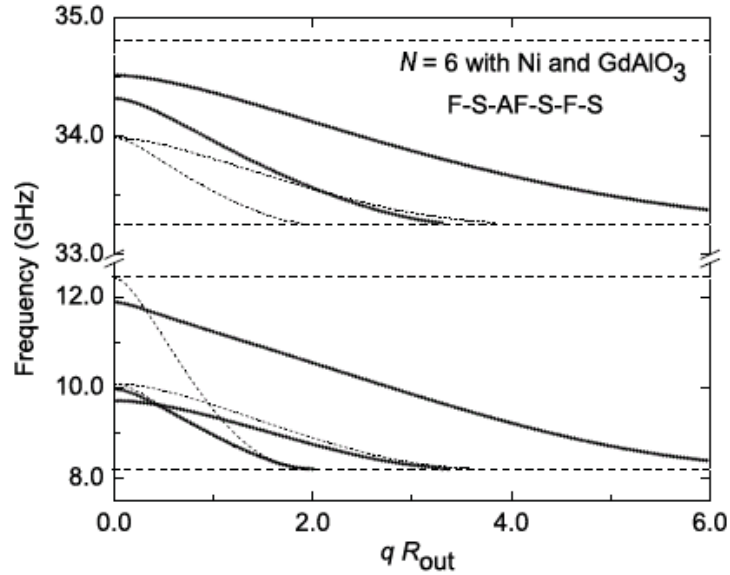
Figure 2.15: As in Fig. 2.12, but for a multilayer with both F and AF layers, taking N = 6 and the structure indicated. The radii are chosen as $R_1 = 25$, $R_2 = 35$, $R_3 = 60$, $R_4 = 75$, $R_5 = R_{out} = 100$ (all in nm) , while $\mu_0 H_0 = 0.1$ T and $|n|$ = 1. As indicated, there are now two regions for the localized modes (note the scale change in the vertical axis). The curves with the filled circles are for the coupled modes of the multilayer, while the other curves (with dashed lines) are the dispersion curves in the absence of any interlayer coupling.

separated, since there are two AF interfaces and three F interfaces. Nevertheless, the mode coupling effect is significant, as can be seen by comparison with the curves shown with dashed lines. The latter are the dispersion curves calculated for the individual magnetic elements (i.e., for a F wire, an AF tube, and a F tube with the appropriate sizes in the absence of the other magnetic elements). It can be seen that in the upper region the coupling in the multilayer has produced an upward shift in the two branches and has also removed the degeneracy that would occur as $q \rightarrow 0$ in an isolated AF tube. In the lower region the coupling in the multilayer has produced a shift in all the branches and has drastically altered one of the mode cut-off values for q at the lower limit. This change in cut-off q can be associated broadly with modified localization properties of the interface mode in the F core.

We have also studied the effects of varying the applied field H_0 for the same mixed F/AF multilayer as in Fig. 2.15. There is an interesting field dependence because the two frequency regions where localized modes may occur have quite different properties as H_0 is varied. For example, if H_0 is increased above the value in Fig. 2.15, the AF region shifts downwards in frequency (and becomes very narrow) whereas the F region shifts upwards. For a small range of field values around $\mu_0 H_0 \sim$ 0.47 T the two regions may be overlapping, and then for $\mu_0 H_0$ greater than about 0.50 T the regions are reversed in order compared to the situation in Fig. 2.15. We then find that the localized mode properties are drastically modified. For example, when $\mu_0 H_0 = 0.52$ T we find only three localized modes (instead of five as in Fig. 2.15) because the localization condition at some of the interfaces can no longer be satisfied due to the inhibiting effect of the larger H_0.

2.6   Conclusions

In this chapter the theory of surface and bulk magnetostatic SW in F and AF nanotubes has been developed, taking the external magnetic field parallel to the symmetry axis of the tube. We used the magnetostatic form of Maxwell's equations to describe the propagation of the modes. The appropriate forms of the dynamic (frequency-dependent) susceptibility of the magnetic material and the standard electromagnetic boundary conditions at the two interfaces of the tube were employed for the general form of theoretical dispersion relations of the surface and bulk magnetostatic modes. We applied these analytical results to Permalloy ($Ni_{80}Fe_{20}$) in the F case and MnF_2 in the AF case for numerical studies of surface and bulk modes in terms of their dispersion relations and radial amplitudes. Other applications to Ni and $GdAlO_3$ gave qualitatively similar results in the F and AF cases, respectively, and are not presented here. Two limiting cases of the geometry provide the surface and bulk magnetostatic modes for magnetic wires and anti-wires.

In the wire case the previous dispersion relations of the surface magnetostatic modes for F nanowires [68, 82] have been generalized.

The transfer matrix formalism developed here for multilayers with cylindrical symmetry was used to study the coupled interface modes for various materials. For simplicity we focused on the localized modes, since these occur in particular frequency ranges characteristic of the magnetic material(s), as discussed in [70], and typically give rise to sharp peaks in BLS spectra. The same formalism applies equally well for the coupled bulk modes, which occur in frequency regions where the relevant quantities α_n are complex. Typically the bulk mode spectra consist of many branches and lead to broadened peaks in BLS.

As a direct extension of this work, it would be of interest, through a Green's function approach and by analogy with earlier studies on magnetic thin films [89, 90], to evaluate the spectral intensities of the surface and bulk magnetostatic spin waves in the nanotubes. This will be considered in Chapter 6. Another useful extension would be to generalize the magnetostatic mode calculations to obtain a description of magnetic polaritons in nanotubes. This involves using Maxwell's equations with retardation effects included and will be presented in Chapter 4. Similarly, going to larger wave numbers, it is of interest to consider the dipole-exchange SW in nanotubes, and this is the topic of Chapter 5. The multilayer applications discussed here all involved having the magnetic layers separated by a nonmagnetic spacer. A generalization would be to consider different magnetic materials grown in direct contact. This would require us to replace the applied field H_0 in the susceptibility components χ_a and χ_b by terms that include effective interface anisotropy fields, and the relevant theory will be presented in Chapter 3.

CHAPTER 3

Magnetostatic Modes in Bilayer Cylindrical Systems with Ferromagnetic / Antiferromagnetic Interfaces

(Some of the results in this chapter have been published in [91] and [92])

3.1 Introduction

The phenomenon of exchange anisotropy in coupled magnetic bilayer systems of ferromagnetic (F) and antiferromagnetic (AF) materials grown in direct contact has been studied since its discovery in 1956 by Meiklejohn and Bean (see [7, 93, 94], for reviews). This effective anisotropy leads to a unidirectional shift in the hysteresis loop, accompanied by an exchange bias field and an increase in the coercivity. Based on these physical properties of F-AF coupled systems, there has recently been an interest in exchange-biased lithographed nanostructures and their potential device applications in spin valves, magnetic storage and sensor industries (see [1, 95, 96]). Eisenmenger *et al.* [8] reported that exchange-bias based devices could make magnetic recording media even cheaper than paper. However, there are many unresolved experimental issues in exchange-biased systems, where the effects of size, aspect ratio or shape of the nanostructures on the exchange anisotropy are poorly understood in both the F and AF layers. Inadequate interfacial characterization makes it difficult to optimize the performance of these bilayer (and multilayer) devices.

As a consequence, the considerable interest in bilayer films grown with a direct contact between F and AF materials has been extended to their dynamical properties, e.g., to the coupled magnetostatic modes and their dependence on the interface magnetic anisotropies ([67, 97]). Except for the fabrication of F-AF antidots [19],
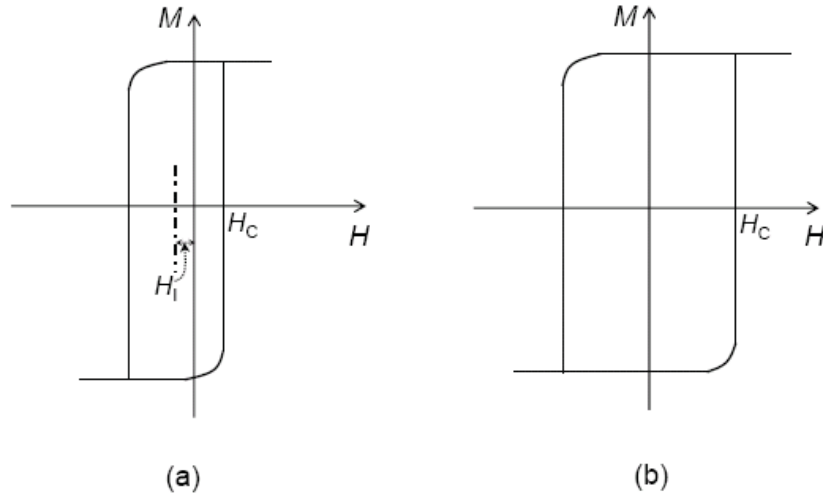
Figure 3.1: Schematic plot of hysteresis loops for an F-AF coupled systems in presence of a (a) strong AF anisotropy and (b) weak AF anisotropy.

there have not so far been any reports of F-AF cylindrical nanostructures. Nevertheless, understanding the effects of exchange bias in confined cylindrical nanostructures and exploring the influence of exchange anisotropies at different surfaces are likely to become important. A motivation for this chapter is to extend the above-mentioned bilayer studies for planar geometries to the case of curved interfaces in various F-AF coupled multilayer cylindrical structures.

The exchange anisotropy (see [1, 19, 93, 98, 99] for reviews) originates as a result of an interfacial exchange coupling between F and AF magnetic moments when these two materials are in direct contact. In the presence of a strongly anisotropic AF material, the magnetic moments in the F layer experience an additional torque and the effective anisotropic field H_I due to this interfacial coupling produces a unidirectional hysteresis loop shift [see Fig. 3.1(a)]. On the other hand, if the AF anisotropy is very weak, no hysteresis loop shift is observed, although the coercive field may become enhanced [see Fig. 3.1(b)]. This effective field H_I can be incorpo-

rated into the Landau-Lifshitz torque equations in Sec. 1.4, modifying the response to study the functions and the magnetostatic SW in the F/AF bilayered cylindrical systems. Thus we expect, by comparison with both the planar case ([67, 97]) studied previously and the cylindrical multilayer results obtained in Chapter 2, that the magnetic modes near the curved interface will have modified frequencies and localization properties.

In generalizing the previous chapter, the simplest case of interest is the two-interface structure in which we take, for example, a F nanotube but fill the core with an AF material, or vice-versa. The theory for this case is presented in Sec. 3.2. Afterwards, in Sec. 3.3, the specific numerical applications of this formalism are given taking Ni and $GdAlO_3$ as the F and AF constituents of the cylindrical bilayer nanotube and its inverse structure. Then we extend our theory in Sec. 3.4 to a magnetic bilayer cylindrical geometry where a nonmagnetic core is surrounded by two concentric F / AF nanotubes of finite thickness (i.e., a three-interface structure). The dispersion relations for the surface magnetostatic modes are presented for Permalloy and $GdAlO_3$ in Sec. 3.5, and finally in Sec. 3.6 we give the conclusions.

3.2 Magnetostatic theory for a bilayer cylindrical nanotube

Here we model the bilayer magnetic system as a long cylindrical tube of one magnetic material (see Fig. 3.2) interfaced with an inner core of another magnetic material. In most cases one of the material is chosen to be an AF and the other is a F, which leads to two distinct cases depending on which is chosen for the core. An external magnetic field is taken parallel to the cylindrical axis (the z axis) and a large length-to-diameter aspect ratio is assumed. The radii R_1 and R_2 are allowed to take general values, but are typically in the sub-micron range. As in Chapter 2, the magnetostatic modes are characterized in terms of a wave number q along the cylinder axis of symmetry, and again we assume $q \sim 10^6$ or 10^7 m^{-1}.
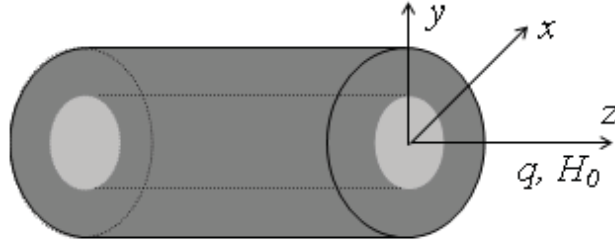
Figure 3.2: A cylindrical nanotube with inner and outer radii R_1 and R_2 of one magnetic material (e.g., a F) with the core filled by a different magnetic material (e.g., an AF), or vice versa, is surrounded by a nonmagnetic material. The external magnetic field H_0 and propagation wave number q are along the z axis, parallel to the magnetization (of the F) and the sublattice magnetization (of the AF).

Following our calculations in the previous chapter for a single magnetic material in a cylindrical geometry, we now solve for the dynamic response within each magnetic material using Maxwell's equations (without retardation) and the non-diagonal magnetic susceptibility tensors. The latter quantities again have a gyromagnetic form with the nonzero frequency-dependent components $\chi_{xx} = \chi_{yy} = \chi_a$ and $\chi_{xy} = -\chi_{yx} = i\chi_b$. This form is applicable when the z axis (the cylindrical axis) coincides with the direction of the applied field H_0, the magnetization of the F, and the sublattice magnetization of the AF, as in Fig. 3.2. However, in presence of the effective exchange anisotropy, the previous expressions for χ_a and χ_b in Eqs. (1.16) - (1.18) will be modified here. Due to the direct exchange coupling of magnetic moments at the F / AF interface, the effective fields used in the Landau-Lifshitz equation will contain an additional term for each F and uniaxial AF material [39, 82]. Taking this into account and following Refs. [67, 97], the static part of the effective magnetic fields in the F material and the AF material will be modified as

$$H^F = H_0 + (M_{AF}/\langle M \rangle)H_I \,, \quad H^{AF} = H_0 + (M_F/\langle M \rangle)H_I \,, \qquad (3.1)$$

where H_I is the interface anisotropy field and $\langle M \rangle$ is a volume-weighted average of M_F and M_{AF} for the bilayer. The susceptibility tensor components χ_a and χ_b in Chapter 1 for F and AF material are then re-expressed through the replacement of the applied field H_0 by the above effective fields for each F and AF material. Accordingly, the terms in ω_0 will be modified for each material, but the other quantities ω_m, ω_{AF}, ω_A and ω_E remain the same as before.

Briefly, the magnetostatic calculations proceed by generalizing our previous work in Chapter 2 (see also [100]). The appropriate Maxwell's equations are re-expressed in terms of the magnetostatic scalar potential Ψ, which satisfies the Walker equation inside each of the magnetic materials and Laplace's equation in the non-magnetic material outside. The solutions have the general form $\psi_{n,q}(r)\exp(in\theta + iqz)$ in cylindrical polar coordinates, where n is an integer and q is the wave number. The solutions for the radial function ψ involve the standard Bessel functions $I_n(\alpha_1 qr)$ for $r < R_1$, a combination of $I_n(\alpha_2 qr)$ and $K_n(\alpha_2 qr)$ for $R_1 < r < R_2$, and $K_n(qr)$ for $r > R_2$. The α parameters are ω-dependent quantities and can be expressed as in Chapter 2 for each magnetic material. They are either real or imaginary for surface-like modes (localized near the interfaces) or bulk-like modes (with a wave-like behavior in the radial direction), respectively. Taking into account the effective anisotropy at $r = R_1$ (the F / AF interface) and applying the magnetostatic boundary conditions at $r = R_1$ and R_2, we find the dispersion relation for the surface and bulk modes given by

$$\begin{vmatrix} I_n(\alpha_1 qR_1) & -c_1 & -d_1 & 0 \\ I_n(\alpha_1 qR_1)\Phi_{I11} & -c_1\Phi_{K21} & -d_1\Phi_{I21} & 0 \\ 0 & c_2 & d_2 & -K_n(qR_2) \\ 0 & c_2\Phi_{K22} & d_2\Phi_{I22} & -K_n{}'(qR_2) \end{vmatrix} = 0, \tag{3.2}$$

where $c_i = K_n(\alpha_2 qR_i)$, $d_i = I_n(\alpha_2 qR_i)$, with i and j denoting 1 or 2, and
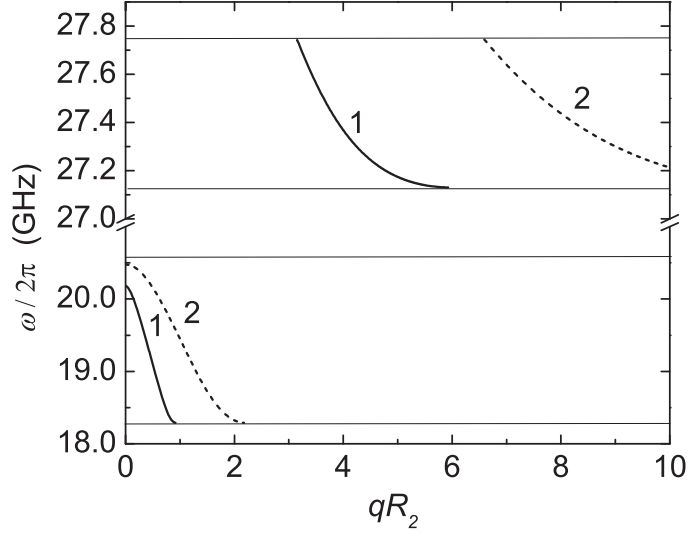
Figure 3.3: Frequencies of the surface modes in a Ni nanotube with a GdAlO$_3$ core plotted versus the dimensionless qR_2. The parameters are $\mu_0 H_0 = 0.3$ T, $\mu_0 H_I = 0.05$ T, $R_1 / R_2 = 0.4$, and the labels 1 and 2 refer to the $|n|$ values.

$$\Phi_{Kji} = \frac{K_n{}'(\alpha_j qR_i)}{\alpha_j K_n(\alpha_j qR_i)} - \frac{n\chi_b{}^j}{qR_i}. \tag{3.3}$$

There is a similar definition for Φ_{Iji} in terms of the Bessel function $I_n(\alpha_j qR_i)$.

3.3 Numerical results for bilayer nanotubes

We now apply the above theory to bilayer structures in which the F material is Ni (for which $\omega_m/2\pi = 18.7$ GHz) and the AF is GdAlO$_3$ (for which $\omega_m/2\pi = 22.0$ GHz, $\omega_A/2\pi = 10.2$ GHz, and $\omega_E/2\pi = 52.6$ GHz), implying a relatively low AFR frequency corresponding to $\omega_{AF}/2\pi = 34.4$ GHz). These parameter values are the same as in Refs. [70, 100]. There are two possible bilayer structures to consider, depending on which material forms the core, and we show below that they give rise
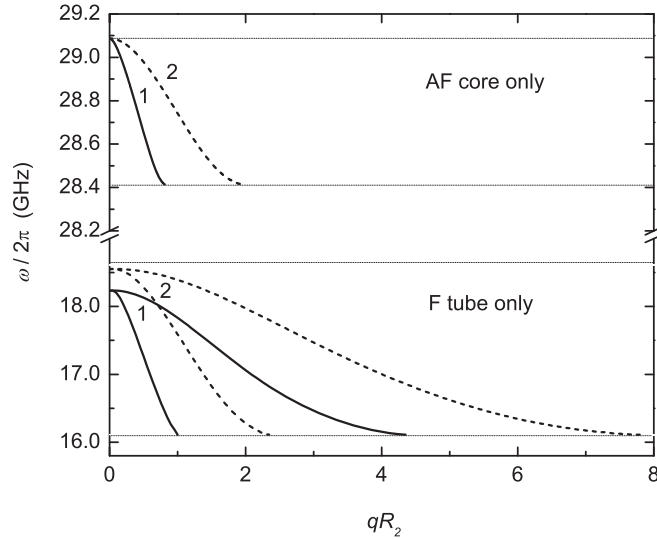
Figure 3.4: For comparison, the same as in Fig. 3.3 but separately for a Ni nanotube (with nonmagnetic core) and for a GdAlO$_3$ nanowire (with nonmagnetic outer layer).

to contrasting properties for the magnetostatic modes.

In Fig. 3.3 we show calculations for a structure where the AF forms the core and it is surrounded by the F. The frequencies of the coupled surface magnetostatic modes for $|n| = 1$ and 2 are plotted versus wave number in terms of the dimensionless qR_2 for the above parameters and using R_1 / R_2 as a structure factor. Qualitatively the modes have some features that are similar to those for cylindrical structures with one magnetic material (see Chapter 2 and [70, 82, 100]). For example, the frequency of each branch decreases monotonically as q increases until there is a cut-off value above which no localized modes occur. Also the modes exist only within specific ranges of frequency, as indicated by the horizontal lines. However, quantitatively there are important differences including the existence of two bands of frequencies for each $|n|$. Broadly, these have the character of an upper perturbed AF band and a lower perturbed F band. Results for the frequencies, q dependence, and localization
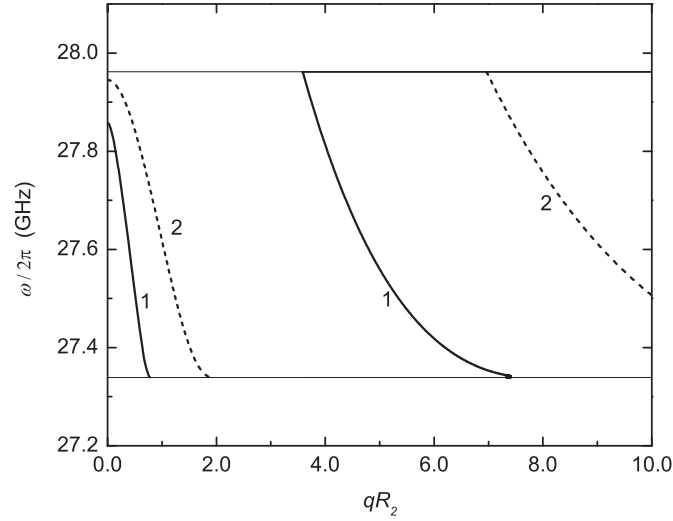
Figure 3.5: As in Fig. 3.3 but for the inverse structure consisting of a GdAlO$_3$ nanotube with a Ni core, using the same field values and the same radii. By contrast with Fig. 3.3, there is only one region of surface modes in this case.

are strongly affected by the R_1 / R_2 ratio and the interface coupling. For comparison we show in Fig. 3.4 the corresponding dispersion relations for the AF core on its own and the F tube on its own, each surrounded by a nonmagnetic (vacuum) region. We note that one of the branches to the dispersion relation for the F tube is suppressed in the coupled structure (Fig. 3.3) because the localization condition can no longer be satisfied. Furthermore there is a shift for each band.

Next we show in Fig. 3.5 some calculations for the inverse bilayer structure to that of Fig. 3.3. Hence in this case the F forms the core and it is surrounded by an AF tube. The modification due to the coupling in this geometry is found to be more drastic than previously, essentially because the lower-frequency material now fills the core. In fact, for the example shown the lower range of frequencies is absent since the localization conditions are not satisfied. Again, for comparison, Fig. 3.6
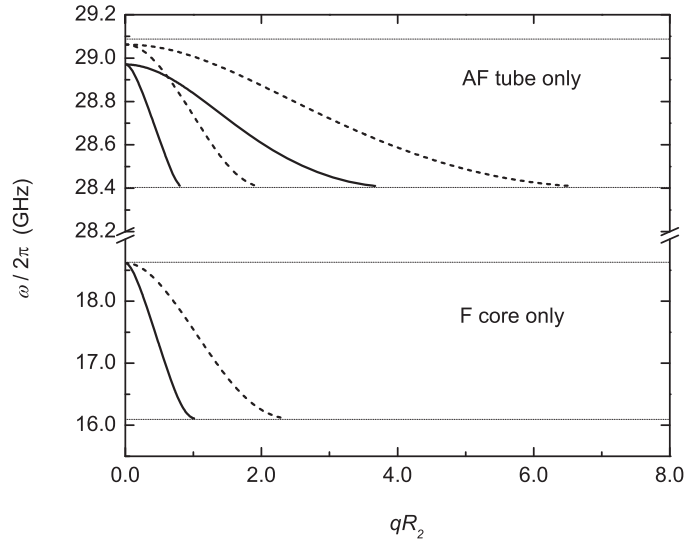
Figure 3.6: As in Fig. 3.4 but separately for a GdAlO$_3$ nanotube (with nonmagnetic core) and for a Ni nanowire (with nonmagnetic outer layer).
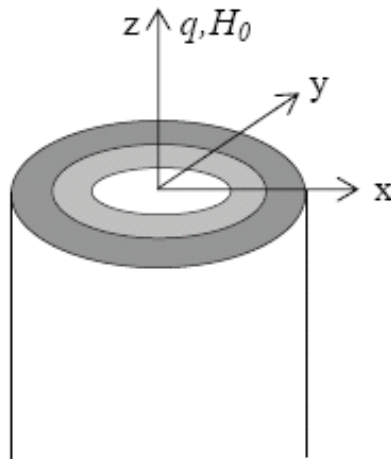
Figure 3.7: A bilayer cylindrical nanotube where the light shaded region represents one magnetic material (e.g., AF) extending from radius R_1 to R_2, while the darker shaded region is the other magnetic material (e.g., F) from R_2 to R_3. The magnetic field H_0 and wave number q are along the z axis, parallel to the F magnetization and AF sublattice magnetization.

shows the dispersion relations that would apply for the core and the tube separately.

3.4   Theory for F-AF cylindrical multilayers

Here we extend our previous magnetic bilayer calculations in Sec. 3.2 to the more general geometry shown in Fig. 3.7, where there is a nonmagnetic core and the double-walled magnetic nanotube has inner and outer radii R_1 and R_3 respectively and an internal interface at R_2. Using the multilayer notation of the previous chapter, this is a three-interface structure ($N = 4$) corresponding to S-AF-F-S or its inverse S-F-AF-S. As before, H_0 is taken parallel to the cylindrical axis (the z axis) and a large length-to-diameter aspect ratio is assumed. The magnetostatic modes are characterized by the wave number q along the cylinder axis. The regions internal and external to the nanotube are filled by a nonmagnetic medium (assumed here to be vacuum).

By extension of the calculations in Chapter 2 for a nanotube composed of just one material, we now solve for the dynamic response within each material using Maxwells equations (without retardation) and applying electromagnetic boundary conditions at all interfaces. The magnetic susceptibility tensors in terms of χ_a and χ_b for the materials forming the bilayer have the same modified form as discussed in Sec. 3.2. In particular, Eq. (3.1) is again applicable.

Following our previous methodology in Sec. 3.2 (see also [71]) the appropriate Maxwells equations are re-expressed in terms of the magnetostatic scalar potential, which satisfies the Walker equation inside each of the magnetic tubes and Laplace's equation in the vacuum regions outside. In cylindrical polar coordinates the solutions have the form of a radial function multiplied by $\exp(in\theta + iqz)$, where n is an integer. The radial function has solutions involving the Bessel functions $I_n(qr)$ for $r < R_1$, combinations of $I_n(\alpha_m qr)$ and $K_n(\alpha_m qr)$ inside the tubes, and $K_n(qr)$ for $r > R_3$. The frequency-dependent α_m can be defined as before (see Sec. 3.2) for

a magnetic material, and we denote the values as α_1 for $R_1 < r < R_2$ and α_2 for $R_2 < r < R_3$. The surface-like (localized) modes and bulk-like modes correspond to real and imaginary α_m, respectively. As for the previous F / AF bilayer nanotubes, the role of the anisotropy due to the two materials in contact (i.e., at the $r = R_2$ interface in our case) is expected to be important.

The final step is to apply the magnetostatic boundary conditions, as already discussed [70], at the three interfaces, giving rise to six coupled equations involving the six undetermined coefficients in the scalar potential. A dispersion relation for the surface and bulk magnetostatic modes is then obtained in the form

$$
\begin{vmatrix}
I_n(qR_1) & -c_{11} & -d_{11} & 0 & 0 & 0 \\
I_n^{'}(qR_1) & -c_{11}\Phi_{K11} & -d_{11}\Phi_{I11} & 0 & 0 & 0 \\
0 & c_{21} & d_{21} & -c_{22} & -d_{22} & 0 \\
0 & c_{21}\Phi_{K12} & d_{21}\Phi_{I12} & -c_{22}\Phi_{K22} & -d_{22}\Phi_{I22} & 0 \\
0 & 0 & 0 & c_{32} & d_{32} & -K_n(qR_3) \\
0 & 0 & 0 & c_{32}\Phi_{K23} & d_{32}\Phi_{I23} & -K_n^{'}(qR_3)
\end{vmatrix} = 0, \quad (3.4)
$$

where $c_{ij} = K_n(\alpha_j qR_i)$, $d_{ij} = I_n(\alpha_j qR_i)$, with i denoting 1 or 2 or 3, j denoting 1 or 2, and

$$
\Phi_{Kji} = \frac{K_n^{'}(\alpha_j qR_i)}{\alpha_j K_n(\alpha_j qR_i)} - \frac{n\chi_b^{\,j}}{qR_i}. \tag{3.5}
$$

There is a similar definition for Φ_{Iji} in terms of the Bessel function $I_n(\alpha_j qR_i)$.

3.5   Numerical results for multilayers

Numerical applications to the magnetic bilayer structures considered in Sec. 3.4 are now made, taking the F as Permalloy (or $Ni_{0.8}Fe_{0.2}$), for which $\omega_m/2\pi = 23.9$ GHz (see [70]). The AF is chosen as uniaxial $GdAlO_3$, using the same material
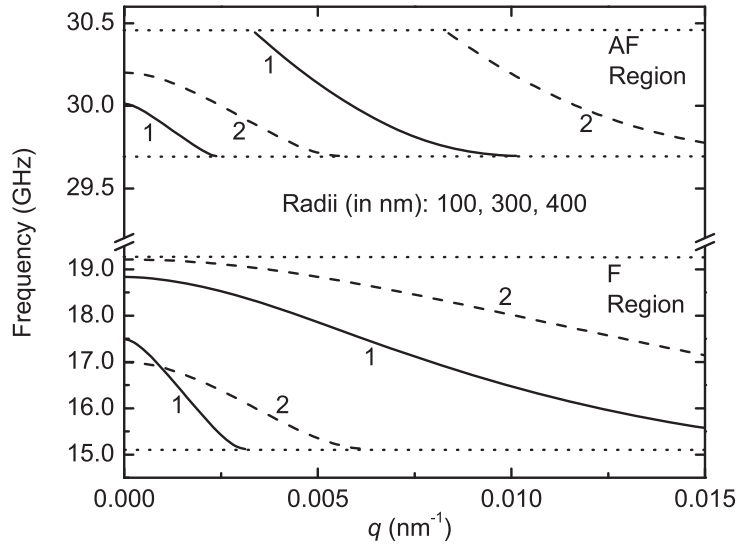
Figure 3.8: Frequencies of surface modes in a Permalloy / GdAlO$_3$ nanotube plotted versus wave number q, where the F forms the inner layer. Solid and broken lines refer to $|n| = 1$ and 2.

parameters as in Sec. 3.3. The applied magnetic field and the interface anisotropy field are chosen as $\mu_0 H_0 = 0.2$ T and $\mu_0 H_I = 0.05$ T.

There are two possible bilayer structures to consider, depending on which material forms the inner layer, and we now show that they give rise to contrasting behaviour for the coupled magnetostatic modes. In Fig. 3.8 we show an example where the F forms the inner layer of the tube. The frequencies of the coupled surface magnetostatic modes for $|n| = 1$ and 2 are plotted versus q for the above parameters and assuming values for R_1, R_2 and R_3 as indicated. Qualitatively the modes have some features that are similar to those for cylindrical nanotubes with one magnetic material [70], except that there are two bands of frequencies, labeled as the AF Region and the F Region, which are characteristic of the component materials. However, due to the coupling, the surface modes within each region
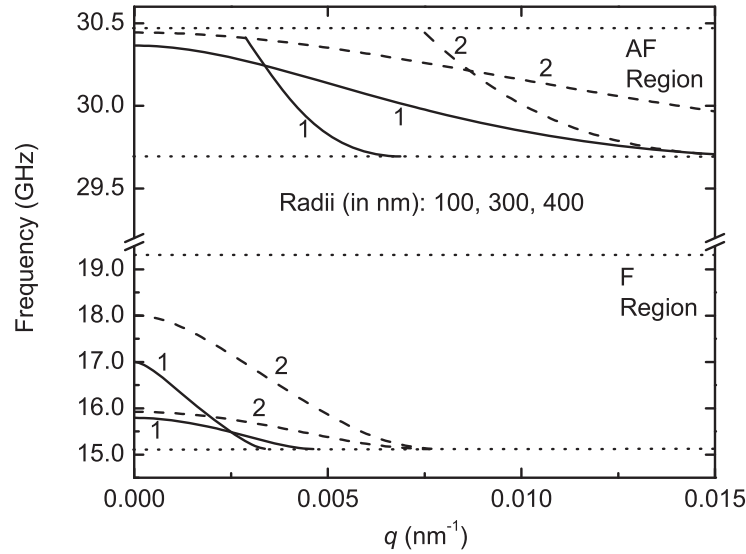
Figure 3.9: As in Fig. 3.8 but for the inverse bilayer nanotube structure where the AF now forms the inner layer, using the same values of the radii.

are perturbed in frequency and their localization properties are modified. As in Chapter 2 and previously in Chapter 3 (see also [70]), the frequency of each branch decreases monotonically as q increases until there is a cut-off value above which no localized modes occur. Also the modes exist only within specific ranges of frequency, as indicated by the horizontal lines. Quantitatively there are important differences that include the existence of the two bands of frequencies, as well as two branches for each $|n|$ in both bands. Other new features, which are a consequence of coupling across the cylindrical interface leading to restrictive conditions for localization, are the cut-off values when q is decreased seen for the uppermost surface branch in the AF region.

In Fig. 3.9 we present results for the inverse structure to that just described, i.e., the same values of the radii are employed for the bilayer but the AF is now the inner layer. It can be seen that the results are quite different in terms of the mode
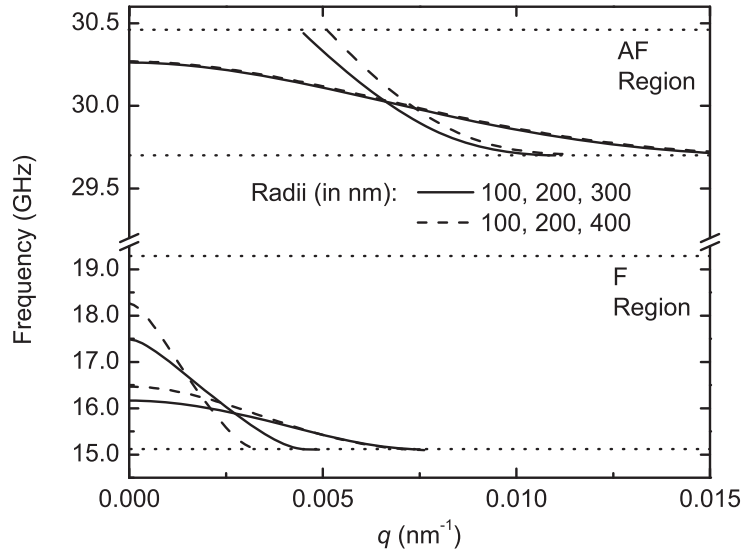
Figure 3.10: Frequencies of surface modes with $|n| = 1$ in a Permalloy / GdAlO$_3$ nanotube plotted versus q, where the AF forms the inner layer. Solid and broken lines refer to structures with different radii.

frequencies, cut-off values for q, hybridization (mode mixing), etc.

A final numerical example is given in Fig. 3.10, where we again take the case of a bilayer with the AF as the inner layer (as in Fig. 3.9), but we illustrate the effects of varying the radii. The mode dispersion curves are shown for $|n| = 1$ only, but we consider two different sets of values for the radii (see the solid and broken lines) in addition to those quoted in Fig. 3.9 for an analogous bilayer. In each case the four surface modes can be approximately associated with localization near the inner and outer radii of the AF and near the inner and outer radii of the F, although there is also some degree of mode mixing. The modes in Fig. 3.10 that are the least affected by the size variations are those represented by the almost degenerate curves starting at ~ 30.3 GHz in the AF Region, and we can identify these as having their maximum amplitude near the vacuum / AF interface (at $r = R_1$) and mainly localized within

the AF layer. The other mode (localized near R_2) in the AF Region is shifted in frequency due to the role of the interface anisotropy, which gives different H^F and H^{AF} values for the two structures in accordance with Eq. (3.1) due to a modified $\langle M \rangle$. Likewise the mode localized near R_2, but mainly in the F layer, is represented by the branches starting at ~ 16.2 and 16.5 GHz for the two structures in Fig. 3.10.

3.6 Conclusions

We have presented calculations for AF / F magnetic bilayer structures with a cylindrical geometry, generalizing previous studies for planar systems. Taking Ni, Permalloy and GdAlO$_3$ as examples we showed how the dispersion relations for surface magnetostatic modes are changed with respect to our previous calculations in Chapter 2 and how the inverse structures have different properties. In the two-interface case of tubes where GdAlO$_3$ is the core we showed how the frequency and localization properties were different from those in the inverse structure with Ni as the core. By extending our calculations to three interface cylindrical structures as long concentric tubes around a nonmagnetic core and its inverse structure, we also illustrated the different mode localization, hybridization and degeneracy of magnetic modes for various radii. Analogous conclusions follow regarding the coupled bulk modes of these magnetic bilayers. Numerical calculations (not shown) using AF materials with higher anisotropy (such as MnF$_2$) have also been carried out, leading to qualitatively similar results. However, the applications using GdAlO$_3$ are likely to be of greater interest since this AF has a much weaker uniaxial anisotropy (implying a smaller AF resonance frequency that may be comparable in magnitude with the F resonance frequency) than is typically the case.

Inelastic light scattering (which can be either BLS or RLS, depending on the frequency range of the modes) provides a convenient experimental technique to study the coupled magnetostatic modes described in this chapter. Further investigations of

the surface and interface dynamical effects as well as the role of interface anisotropy, could be carried out using the generalized multilayer formalism discussed in Sec. 2.4.

CHAPTER 4
Magnetic Polaritons in Cylindrical Tubes

(Some of the results in this chapter have been published in [101])

4.1 Introduction

As already mentioned, there has been recent interest in the SW excitations of long magnetic nanowires and nanotubes, in particular for the magnetostatic regime (discussed in Chapters 2 and 3) and the dipole-exchange regime (see the next chapter), from both the experimental [59, 60] and theoretical [68, 70, 82, 102] perspectives. On the other hand, the corresponding retarded electromagnetic modes or magnetic polaritons have been studied in a wide variety of finite systems, mostly in thin-film and other planar geometries (see, e.g., [35] for a review). The theory of surface polaritons on planar AF films [103], and their experimental investigation using attenuated total reflection (ATR) [56] are already well established. However, this is not so far the case for F and AF tubes, where the mode coupling is more complex, except in some special cases. Unlike the planar or even the spherical geometries, the cylindrical curved interfaces do not generally allow for the analysis of the transverse electric (TE) and the transverse magnetic (TM) modes independently [14]. As a result, the propagation of magnetic polaritons in cylindrical geometries is expected to be studied in terms of solutions for the transverse electromagnetic (TEM) modes. This has motivated the work of the present chapter.

In Chapters 2 and 3 we studied the SW dynamics in the magnetostatic regime of wavevectors (see Fig. 1.3) for multi-interface cylindrical geometries where the relevant wavevector values are easily accessible through BLS experiments. These analyses were carried out in terms of the magnetostatic form of Maxwell's equations

and the corresponding boundary conditions. In the present chapter we expand our earlier work by including the retardation effects to develop a theory of SW polaritons in the electromagnetic regime (see Fig. 1.3) where the coupling between the electromagnetic wave and the SW excitations must be taken into account in the dynamics. A brief introduction to magnetic polaritons in infinite media and planar films was given in Sec. 1.5.3. The aim of this chapter is to extend the earlier studies of polaritons in magnetic cylindrical wire structures (see [104, 105, 106]), where calculations were done for AF materials in a zero applied field, and to develop a theory for the localized surface and bulk magnetic polaritons in hollow magnetic cylinders or tubes (of AF or F materials) when a longitudinal applied field is present. For the experimental observation of these modes, the ATR, RLS and BLS techniques (see Sec. 1.6 and [16, 35] for reviews) would be the most promising to observe these modes.

Extending the approach in Chapter 2, we begin in Sec. 4.2 by describing our theory which consists of solving for the dynamical response using the non-diagonal susceptibility tensor for a F or AF and Maxwell's equations. The electric and magnetic field components within the magnetic and nonmagnetic regions are written in cylindrical coordinates and the explicit solutions are derived in complete forms where both fields are coupled in general. Afterwards, we apply the electromagnetic boundary conditions at the inner and outer tube interfaces to obtain the theoretical dispersion relations. In the absence of applied field for an AF, we describe a simplified theory, as a special case, where the longitudinal field components can be decoupled (allowing separation into TE and TM parts). The results for wires and antiwires are deduced as limiting cases of this geometry. In Sec. 4.3, we make numerical applications to YIG and MnF_2 materials in antiwire, wire and tube geometries using the full version of our theory. Finally, in Sec. 4.4 we summarize our analysis of magnetic polaritons.

4.2 Theoretical formalism for polariton modes in tubes

To investigate the properties of surface and bulk polaritons in F or AF cylindrical tubes we use the same geometrical model as in Fig. 2.1, where there are two nonmagnetic-magnetic interfaces at $r = R_1$ and at $r = R_2$ in terms of cylindrical polar coordinates (r, θ, z). By analogy with Chapter 2, the wire $(R_1 \to 0, R_2 \neq 0)$ and antiwire $(R_1 \neq 0, R_2 \to \infty)$ geometries are obtained as special limiting cases. Our previous calculations in Chapters 2 and 3 focussed on cases where the wave number q along the z axis corresponded to the magnetostatic [70] regime. Here we are concerned with the polariton or electromagnetic regime where exchange effects are again negligible but we include the retardation effects which become important at much smaller q.

In the presence of a longitudinal magnetic field and a static magnetization (or sublattice magnetization) along the symmetry axis (the z axis) of the tube, the dynamic response (at frequency ω) of a F or AF material in the region $R_1 < r < R_2$ can be characterized by a gyromagnetic permeability tensor [16]

$$\overleftrightarrow{\mu}(\omega) = \begin{pmatrix} \mu_1(\omega) & i\mu_2(\omega) & 0 \\ -i\mu_2(\omega) & \mu_1(\omega) & 0 \\ 0 & 0 & 1 \end{pmatrix}, \tag{4.1}$$

and a diagonal dielectric tensor chosen as

$$\overleftrightarrow{\epsilon} = \begin{pmatrix} \epsilon & 0 & 0 \\ 0 & \epsilon & 0 \\ 0 & 0 & 1 \end{pmatrix}, \tag{4.2}$$

where $\mu_1 = 1 + (\chi^+ + \chi^-)/2$, $\mu_2 = (\chi^+ - \chi^-/2$ and ϵ is a frequency independent constant. The quantities χ^+ and χ^- are expressed as in Eqs. (1.16) - (1.18) for F and AF materials. Although $\chi^{\pm}$ is more complicated for an AF than for a F, we have

$\chi^+ = \chi^-$ and so $\mu_2 = 0$ when $H_0 = 0$. Therefore there is a diagonal permeability tensor in this special case, which is not found for a F material. When $H_0 = 0$, we note that the response function term ν ($= 1/\mu_1$) in Fig. 2.3 will simplify to have poles at the resonance frequency ω_{AF}, and we later conclude that an enormous simplification then arises in determining the polariton modes for an AF cylindrical tube with $H_0 = 0$. The nonmagnetic layers in the regions $r < R_1$ and $r > R_2$ of tubes are occupied with vacuum or air and, are described by diagonal dielectric and magnetic permeability tensors with ϵ replaced by ϵ_1, $\mu_1 = 1$ and $\mu_2 = 0$.

In order to derive the dispersion relations for polariton spectra, we use the complete form of Maxwell's equations (see [14]) without sources of free charges or macroscopic currents, which can be written as stated in Eqs. (1.33) - (1.34). Also we note that the speed of light in the vacuum corresponds to $c = 1/\sqrt{\mu_0 \epsilon_0}$.

The calculation of the polariton modes proceeds by solving Maxwell's equations in cylindrical polar coordinates for a tube geometry. By contrast with our magnetostatic calculations (see Chapters 2 and 3), we cannot employ a scalar potential, but instead we seek solutions in terms of the electromagnetic fields, which have the general form

$$
\begin{aligned}
\vec{E}(r, \theta, z, t) &= \vec{E}(r) \exp[i(n\theta + qz - \omega t)], \\
\vec{H}(r, \theta, z, t) &= \vec{H}(r) \exp[i(n\theta + qz - \omega t)]
\end{aligned}
\tag{4.3}
$$

where n is an integer and q is the longitudinal wave number, as before. Using Eqs. (1.33) and (4.3) we can write the components of the electric field $\vec{E}(r) = (E^r, E^\theta, E^z)$ and magnetic field $\vec{H}(r) = (H^r, H^\theta, H^z)$ within the F or AF material as

$$
\frac{d}{dr}(\epsilon r E^r) + in\epsilon E^\theta + iqr E^z = 0,
$$

$$
\frac{d}{dr}\{r(\mu_1 H^r + i\mu_2 H^\theta)\} + in(\mu_1 H^\theta - i\mu_2 H^r) + iqr H^z = 0,
$$

$$\frac{1}{r}(nE^z - qrE^\theta) - \omega\mu_0(\mu_1 H^r + i\mu_2 H^\theta) = 0,$$

$$\frac{dE^z}{dr} - iqE^r + i\omega\mu_0(\mu_1 H^\theta - i\mu_2 H^r) = 0,$$

$$\frac{d}{dr}(rE^\theta) - inE^r - i\omega\mu_0 rH^z = 0,$$

$$\omega r(\frac{\epsilon}{\mu_0 c^2})E^r - qrH^\theta + nH^z = 0,$$

$$\frac{dH^z}{dr} - iqH^r - i\omega(\frac{\epsilon}{\mu_0 c^2})E^\theta = 0,$$

$$\frac{d}{dr}(rH^\theta) - inH^r + i\omega r(\frac{\epsilon}{\mu_0 c^2})E^z = 0. \tag{4.4}$$

After some lengthy calculations, all the transverse field components (namely, E^r, E^θ, H^r and H^θ) in Eq. (4.4) can be re-expressed in terms of the longitudinal field components E^z and H^z as

$$E^r = \frac{1}{(\kappa^4 - \xi^4)}\left\{ iq\left(\kappa^2\frac{dE^z}{dr} + \frac{n\xi^2}{r}E^z \right) + \mu_0\omega\left(\mu_2 q^2\frac{dH^z}{dr} + \frac{n(\mu_1\kappa^2 - \mu_2\xi^2)}{r}H^z \right) \right\},$$

$$E^\theta = \frac{1}{(\kappa^4 - \xi^4)}\left\{ -q\left(\xi^2\frac{dE^z}{dr} + \frac{n\kappa^2}{r}E^z \right) + i\mu_0\omega\left((\mu_1\kappa^2 - \mu_2\xi^2)\frac{dH^z}{dr} + \frac{n\mu_2 q^2}{r}H^z \right) \right\},$$

$$H^r = \frac{1}{(\kappa^4 - \xi^4)}\left\{ -\omega\epsilon_0\epsilon(\xi^2\frac{dE^z}{dr} + \frac{n\kappa^2}{r}E^z) + iq(\kappa^2\frac{dH^z}{dr} + \frac{n\xi^2}{r}H^z) \right\},$$

$$H^\theta = \frac{1}{(\kappa^4 - \xi^4)}\left\{ -i\omega\epsilon_0\epsilon\left(\kappa^2\frac{dE^z}{dr} + \frac{n\kappa^2}{r}E^z \right) - q\left(\xi^2\frac{dH^z}{dr} + \frac{n\kappa^2}{r}H^z \right) \right\}, \tag{4.5}$$

with $\kappa^2 = (\omega^2\epsilon\mu_1/c^2) - q^2$ and $\xi^2 = \omega^2\epsilon\mu_2/c^2$. Likewise, we find from Eq. (4.4) that

the longitudinal field components E^z and H^z are coupled in general and satisfy

$$\nabla^2 E^z(r) + \left(\kappa^2 - \xi^2 \frac{\mu_2}{\mu_1} + q^2 \right) E^z(r) + \beta H^z(r) \;\; = \;\; 0,$$

$$\nabla^2 H^z(r) + \left(\frac{\kappa^2}{\mu_1} + q^2 \right) H^z(r) + \delta E^z(r) \;\; = \;\; 0, \qquad (4.6)$$

where $\beta = -i\mu_0 \omega q \mu_2 / \mu_1$ and $\delta = i\epsilon_0 \epsilon \omega q \mu_2 / \mu_1$ are coupling terms.

In the absence of a static applied magnetic field, the off-diagonal permeability tensor component μ_2 vanishes for an AF material, which causes $\beta = \delta = 0$. This implies a decoupling of E^z and H^z in Eq. (4.6), which reduces to two independent equations of the form

$$\nabla^2 E^z(r) + \left(\kappa^2 + q^2 \right) E^z(r) \;\; = \;\; 0,$$

$$\nabla^2 H^z(r) + \left(\frac{\kappa^2}{\mu_1} + q^2 \right) H^z(r) \;\; = \;\; 0. \qquad (4.7)$$

In this special case, the above two equations can be solved independently for E^z and H^z in order to calculate the retarded TE ($E^z = 0$) and TM ($H^z = 0$) modes. Camley and Mills [42] also discussed a similar situation for the propagation of TE and TM surface polaritons in uniaxial AF films considering the external field to be zero. Another special case of Eq. (4.6) occurs in the limit of neglecting the retardation effects (since $\beta\delta \sim q^2\omega^2/c^2 \to 0$ as $c \to \infty$). The differential equation for H^z then reduces to the form of the Walker equation (see Eq. (2.2)) and can be used to reproduce our previous magnetostatic calculations.

More generally, either for a F tube or for a AF tube with $H_0 \neq 0$ and with retardation included, we cannot separate the TE and TM modes in the cylindrical geometry. Instead we proceed by forming explicit solutions for the radial dependence of $E^z(r)$ and $H^z(r)$ inside the magnetic tube, as well as in the nonmagnetic core and outer regions. Following an established procedure (e.g., as in [107, 108] for

other cylindrical geometries) the solutions for $E^z(r)$ and $H^z(r)$ from Eq. (4.6) each involve linear combinations of Bessel functions of the form $I_n(kr)$ and $K_n(kr)$ where k behaves as an effective wave number in the radial direction. It may be either real or imaginary, corresponding to localized surface-like or bulk-like behavior, respectively. By using Eq. (4.6) it is easily seen that there are actually two values for k, which we denote as k_1 and k_2. These can be obtained as the roots (for k) of the quadratic equation (see [107])

$$k^4 - \frac{\omega^2 \epsilon}{c^2}\left[\mu_1\{1 - (\mu_2/\mu_1)^2\} + 1 - Q^2\{1 + (1/\mu_1)\}\right]k^2 +$$
$$\frac{\omega^4 \epsilon^2}{c^4}\left[\mu_1\{1 - (\mu_2/\mu_1)^2\} + Q^2\{(Q^2/\mu_1) - 2\}\right] = 0, \qquad (4.8)$$

where $Q = cq/\omega\epsilon^{1/2}$. We note that the non-retarded case corresponds to $Q \gg 1$. The two roots k_1 and k_2 in this limit can be simplified to q and $q/\mu_1^{1/2}$. These values correspond to the decoupled TM and TE modes familiar from magnetostatic theory (see, e.g., [35]), as we will discuss in terms of examples later. However, in the general case solutions for the longitudinal field components in terms of k_i ($i = 1, 2$) now involve the linear combinations

$$\begin{aligned} E^z(r) &= a_1 I_n(k_1 r) + a_2 I_n(k_2 r) + b_1 K_n(k_1 r) + b_2 K_n(k_2 r), \\ H^z(r) &= -\frac{X_1}{\beta}a_1 I_n(k_1 r) - \frac{X_2}{\beta}a_2 I_n(k_2 r) - \frac{X_1}{\beta}b_1 K_n(k_1 r) - \frac{X_2}{\beta}b_2 K_n(k_2 r), \end{aligned}$$
$$(4.9)$$

where a_1, a_2, b_1, and b_2 are constants to be determined later by applying boundary conditions. Also we have defined

$$X_i = (\omega^2 \epsilon/c^2)[\mu_1\{1 - (\mu_2/\mu_1)^2\} - q^2/(\omega^2 \epsilon/c^2) - k_i^2/(\omega^2 \epsilon/c^2)]. \quad (4.10)$$

We next use Eqs. (4.9) and (4.5) to obtain the solutions of the transverse field

components in the forms

$$
\begin{aligned}
E^r \;=\; & (iqr)\Bigg[a_1 I_n(k_1 r)\left\{ \frac{1}{k_1 r}\frac{I_n^{'}(k_1 r)}{I_n(k_1 r)} - \frac{n\mu_1 X_1}{\mu_2 (k_1 q r)^2}\right\} + \\
& a_2 I_n(k_2 r)\left\{ \frac{1}{k_2 r}\frac{I_n^{'}(k_2 r)}{I_n(k_2 r)} - \frac{n\mu_1 X_2}{\mu_2 (k_2 q r)^2}\right\} + \\
& b_1 K_n(k_1 r)\left\{ \frac{1}{k_1 r}\frac{K_n^{'}(k_1 r)}{K_n(k_1 r)} - \frac{n\mu_1 X_1}{\mu_2 (k_1 q r)^2}\right\} + \\
& b_2 K_n(k_2 r)\left\{ \frac{1}{k_2 r}\frac{K_n^{'}(k_2 r)}{K_n(k_2 r)} - \frac{n\mu_1 X_2}{\mu_2 (k_2 q r)^2}\right\}\Bigg],
\end{aligned}
$$

$$
\begin{aligned}
E^{\theta} \;=\; & a_1 \frac{I_n(k_1 r)}{k_1{}^2}\left\{ \frac{\mu_1 k_1 X_1}{q\mu_2}\frac{I_n^{'}(k_1 r)}{I_n(k_1 r)} - \frac{nq}{r}\right\} + \\
& a_2 \frac{I_n(k_2 r)}{k_2{}^2}\left\{ \frac{\mu_1 k_2 X_2}{q\mu_2}\frac{I_n^{'}(k_2 r)}{I_n(k_2 r)} - \frac{nq}{r}\right\} + \\
& b_1 \frac{K_n(k_1 r)}{k_1{}^2}\left\{ \frac{\mu_1 k_1 X_1}{q\mu_2}\frac{K_n^{'}(k_1 r)}{K_n(k_1 r)} - \frac{nq}{r}\right\} + \\
& b_2 \frac{K_n(k_2 r)}{k_2{}^2}\left\{ \frac{\mu_1 k_2 X_2}{q\mu_2}\frac{K_n^{'}(k_2 r)}{K_n(k_2 r)} - \frac{nq}{r}\right\},
\end{aligned}
$$

$$
\begin{aligned}
H^r \;=\; & \frac{\mu_1}{\mu_0 \mu_2 \omega}\Bigg[a_1 I_n(k_1 r)\left\{ -\frac{S_1(\omega^2 \epsilon/c^2)}{k_1}\frac{I_n^{'}(k_1 r)}{I_n(k_1 r)} + \frac{n\mu_2 \omega^2 \epsilon}{c^2 \mu_1 r k_1{}^2}\right\} + \\
& a_2 I_n(k_2 r)\left\{ -\frac{S_2(\omega^2 \epsilon/c^2)}{k_2}\frac{I_n^{'}(k_2 r)}{I_n(k_2 r)} + \frac{n\mu_2 \omega^2 \epsilon}{c^2 \mu_1 r k_2{}^2}\right\} + \\
& b_1 K_n(k_1 r)\left\{ -\frac{S_1(\omega^2 \epsilon/c^2)}{k_1}\frac{K_n^{'}(k_1 r)}{K_n(k_1 r)} + \frac{n\mu_2 \omega^2 \epsilon}{c^2 \mu_1 r k_1{}^2}\right\} + \\
& b_2 K_n(k_2 r)\left\{ -\frac{S_2(\omega^2 \epsilon/c^2)}{k_2}\frac{K_n^{'}(k_2 r)}{K_n(k_2 r)} + \frac{n\mu_2 \omega^2 \epsilon}{c^2 \mu_1 r k_2{}^2}\right\}\Bigg],
\end{aligned}
$$

$$H^\theta = \omega \epsilon \epsilon_0 r \left[a_1 I_n(k_1 r) \left\{ \frac{1}{k_1 r} \frac{I_n{}'(k_1 r)}{I_n(k_1 r)} - \frac{n S_1 \mu_1}{\mu_2 (k_1 r)^2} \right\} + \right.$$
$$a_2 I_n(k_2 r) \left\{ \frac{1}{k_2 r} \frac{I_n{}'(k_2 r)}{I_n(k_2 r)} - \frac{n S_2 \mu_1}{\mu_2 (k_2 r)^2} \right\} +$$
$$b_1 K_n(k_1 r) \left\{ \frac{1}{k_1 r} \frac{K_n{}'(k_1 r)}{K_n(k_1 r)} - \frac{n S_1 \mu_1}{\mu_2 (k_1 r)^2} \right\} +$$
$$\left. b_2 K_n(k_2 r) \left\{ \frac{1}{k_2 r} \frac{K_n{}'(k_2 r)}{K_n(k_2 r)} - \frac{n S_2 \mu_1}{\mu_2 (k_2 r)^2} \right\} \right]. \tag{4.11}$$

We have also introduced the notation that (for $i = 1, 2$)

$$S_i = \{c^2/(\omega^2 \epsilon)\}\{(1/\mu_1)(q^2 + k_i{}^2) - \omega^2 \epsilon/c^2\}. \tag{4.12}$$

In the nonmagnetic (vacuum) regions the wave numbers are obtained by putting $\epsilon \to \epsilon_1$, $\mu_1 = 1$ and $\mu_2 = 0$ in Eq. (4.5). It is found (as expected) that there is just a single wave number, denoted by q_{out}, where

$$q_{out} = \sqrt{q^2 - (\omega^2 \epsilon_1/c^2)}. \tag{4.13}$$

We then use the relevant Bessel functions that are well behaved as $r \to 0$ for the core (when $r < R_1$) and as $r \to \infty$ for the outer region (when $r > R_2$). The field components in these two regions reduce to

$$E^z = c_1 I_n \{(\frac{1}{\sqrt{\epsilon_1}} q_{out}) r\},$$
$$H^z = d_1 I_n(q_{out} r),$$
$$E^r = -\frac{iq}{\sqrt{\epsilon_1} q_{out}} c_1 I_n{}' \{(\frac{1}{\sqrt{\epsilon_1}} q_{out}) r\} + \frac{\mu_0 n \omega}{r q_{out}^2} d_1 I_n(q_{out} r),$$
$$E^\theta = \frac{nq}{r q_{out}^2} c_1 I_n \{(\frac{1}{\sqrt{\epsilon_1}} q_{out}) r\} + \frac{i \mu_0 \omega}{q_{out}} d_1 I_n{}'(q_{out} r),$$
$$H^r = -\frac{\epsilon_0 \epsilon_1 n \omega}{r q_{out}^2} c_1 I_n \{(\frac{1}{\sqrt{\epsilon_1}} q_{out}) r\} - \frac{iq}{q_{out}} d_1 I_n{}'(q_{out} r),$$
$$H^\theta = -\frac{i \epsilon_0 \epsilon_1{}^{1/2} \omega}{q_{out}} c_1 I_n{}' \{(\frac{1}{\sqrt{\epsilon_1}} q_{out}) r\} + \frac{nq}{r q_{out}^2} d_1 I_n(q_{out} r), \tag{4.14}$$

for $r < R_1$, while for $r > R_2$ the results are

$$
\begin{aligned}
E^z &= c_3 K_n\{(\frac{1}{\sqrt{\epsilon_1}}q_{out})r\}, \\
H^z &= d_3 K_n(q_{out}r), \\
E^r &= -\frac{iq}{\sqrt{\epsilon_1}q_{out}}c_3 K_n{}'\{(\frac{1}{\sqrt{\epsilon_1}}q_{out})r\} + \frac{\mu_0 n\omega}{rq_{out}{}^2}d_3 K_n(q_{out}r), \\
E^\theta &= \frac{nq}{rq_{out}{}^2}c_3 K_n\{(\frac{1}{\sqrt{\epsilon_1}}q_{out})r\} + \frac{i\mu_0\omega}{q_{out}}d_3 K_n{}'(q_{out}r), \\
H^r &= -\frac{\epsilon_0\epsilon_1 n\omega}{rq_{out}{}^2}c_3 K_n\{(\frac{1}{\sqrt{\epsilon_1}}q_{out})r\} - \frac{iq}{q_{out}}d_3 K_n{}'(q_{out}r), \\
H^\theta &= -\frac{i\epsilon_0\epsilon_1{}^{1/2}\omega}{q_{out}}c_3 K_n{}'\{(\frac{1}{\sqrt{\epsilon_1}}q_{out})r\} + \frac{nq}{rq_{out}{}^2}d_3 K_n(q_{out}r). \quad\quad (4.15)
\end{aligned}
$$

Here c_1, d_1, c_3, and d_3 are constants.

Before proceeding, we emphasize that the general formalism is made compli-cated by the fact that the TM and TE modes are coupled in the cylindrical geometry, except when the magnetic susceptibility is diagonal (as for an AF with $H_0 = 0$) or when the magnetostatic limit is taken, and this is why both wave numbers k_1 and k_2 are needed here. By analogy with previous polariton work (see [35, 105, 107, 109]), we expect that the regime where retardation effects are significant is defined by $qd \sim 1$ and $cq \sim \omega_{res}\epsilon^{1/2}$, where d is the lateral dimension of the magnetic structure and ω_{res} is the resonance frequency (ω_0 for a F or ω_{AF} for an AF). Our numerical applications later confirm these conclusions.

The final stage in these calculations is to apply the standard set of electro-magnetic boundary conditions (see [14]) at both $r = R_1$ and $r = R_2$ interfaces of the tube. Using the condition for the continuity of the tangential **E** and **H** field components involved in Eqs. (4.9), (4.11) and (4.14) allows us to avoid making an unphysical decoupling of the TM and TE parts, since this latter approximation may lead to inconsistencies. For example, some previous calculations in [83] for the polaritons in an AF wire with $H_0 \neq 0$ did not yield the correct limiting behavior for

small retardation (i.e., the magnetostatic results). For the tube geometry the boundary conditions (four at each interface) yield eight homogeneous linear equations for the eight coefficients c_1, d_1, a_1, a_2, b_1, b_2, c_3 and d_3 that appear in the expressions for the field components. An implicit dispersion relation for the polariton modes can then be obtained in the form of the vanishing of a 8×8 determinant in the general tube case. This is described below after considering two special limiting geometries.

The general dispersion relation for a tube reduces to the vanishing of a 4×4 determinant in each the single-interface cases of an antiwire or a wire since only four coefficients are involved. We consider these simple cases to show the dispersion relations as

$$
\begin{vmatrix}
1 & 0 & 1 & 1 \\
0 & (\omega^2\epsilon/c^2) & -X_1 & -X_2 \\
-(n\mu_2/\mu_1)(q/q_{out}R)^2 & (1/u)I_n{}'(u)/I_n(u) & \Phi_{K1} & \Phi_{K2} \\
(\sqrt{\epsilon_1}/\epsilon u)I_n{}'(u/\sqrt{\epsilon_1})/I_n(u/\sqrt{\epsilon_1}) & -n/\{(\mu_2/\mu_1)(q_{out}R)^2\} & \Upsilon_{K1} & \Upsilon_{K2}
\end{vmatrix} = 0
$$

(4.16)

for an antiwire (where the coefficients involved are c_1, d_1, b_1 and b_2), and

$$
\begin{vmatrix}
1 & 1 & 1 & 0 \\
-X_1 & -X_2 & 0 & (\omega^2\epsilon/c^2) \\
\Phi_{I1} & \Phi_{I2} & -(n\mu_2/\mu_1)(q/q_{out}R)^2 & (1/u)K_n{}'(u)/K_n(u) \\
\Upsilon_{I1} & \Upsilon_{I2} & (\sqrt{\epsilon_1}/\epsilon u)K_n{}'(u/\sqrt{\epsilon_1})/K_n(u/\sqrt{\epsilon_1}) & -n/\{(\mu_2/\mu_1)(q_{out}R)^2\}
\end{vmatrix} = 0
$$

(4.17)

for a wire (where the coefficients involved are a_1, a_1, c_3 and d_3). The latter expression has the form of the wire dispersion relations derived by a slightly different method in [107], except that we have corrected for some typographical errors in that paper.

In both cases, we have defined $u = q_{out}R/\sqrt{(\omega^2\epsilon/c^2)}$ and

$$\Phi_{Ki} = -\{(X_i c)/(\omega\sqrt{\epsilon}k_i R)\}K_n{}'\left[k_i R/(\{\sqrt{(\omega^2\epsilon/c^2)}\}\right]/K_n\left[k_i R/(\{\sqrt{(\omega^2\epsilon/c^2)}\}\right] +$$
$$(n\mu_2/\mu_1)(q/k_i R)^2,$$
$$\Upsilon_{Ki} = \{\sqrt{(\omega^2\epsilon/c^2)}/(k_i R)\}K_n{}'\left[k_i R/(\{\sqrt{(\omega^2\epsilon/c^2)}\}\right]/K_n\left[k_i R/(\{\sqrt{(\omega^2\epsilon/c^2)}\}\right] -$$
$$(n\mu_1 S_i \omega^2 \epsilon)/(\mu_2(ck_i R)^2). \qquad (4.18)$$

Similarly, Φ_{Ii} and Υ_{Ii} can be expressed by replacing the Bessel function K everywhere in Eq. (4.18) by the Bessel function I.

The 8×8 determinant condition representing the dispersion relation of SW polaritons in a F or AF tube can now be expressed conveniently in block form as

$$\begin{vmatrix} \mathbf{M}_1 & \mathbf{M}_2 \\ \mathbf{M}_3 & \mathbf{M}_4 \end{vmatrix} = 0, \qquad (4.19)$$

where the M_j $(j = 1, 2, 3, 4)$ are 4×4 arrays. Specifically, the blocks M_1 and M_4 in Eq. (4.19) are formally the same as those in Eqs. (4.16) and (4.17) for the antiwire and wire cases, respectively, except that we replace R everywhere in those equations by R_1 and R_2 respectively. The blocks M_2 and M_3, which describe the additional effects of the second interface (e.g., the mode coupling across the tube thickness), are defined similarly. Specifically, M_2 is defined as in Eq. (4.17) but with R replaced by R_1 and the elements of columns 3 and 4 set to zero, while M_3 is defined as in Eq. (4.16) but with R replaced by R_2 and the elements of columns 1 and 2 set to zero.

As well as describing the surface polaritons, the above characteristic equation can also be used to study the bulk-like polaritons in F and AF antiwires, wires, or tubes. It is simply a matter of replacing the Bessel functions with their appropriate form for complex arguments. It is important to note that in all the geometries for F and AF materials we correctly describe the magnetostatic limit results of Chapter

2 (which is also evident from the numerical examples presented in the following section).

We can also employ the above formalism to examine the variation with respect to r of the surface mode amplitudes corresponding to longitudinal and transverse **E** and **H** field components. The same electromagnetic boundary conditions and the same expressions for the **E** and **H** field components as in Eqs. (4.9) - (4.14) are used to obtain the relative values of the constants involved in these equations. By numerical examples, we will later illustrate the variations of localized retarded mode amplitudes for different cylindrical structures. The variation of mode amplitudes for the bulk polaritons can similarly be found by choosing Bessel functions appropriate to their arguments (by analogy with Chapter 2).

4.3   Numerical applications

To illustrate the above theory, we present numerical examples for the surface polariton frequencies in YIG and MnF_2, chosen to represent the F and AF cases respectively. The applied field H_0 is typically taken to be nonzero. The relevant parameters for YIG are [110]: $\mu_0 M_0 = 0.175$ T, $\gamma/2\pi = 28.01$ GHz/T, and $\epsilon = 5.5$ (for wavelength 632.8 nm). For MnF_2 we use [23]: $\mu_0 M_0 = 0.754$ T, $\mu_0 H_A = 0.787$ T, $\mu_0 H_E = 55.0$ T, $\gamma/2\pi = 27.77$ GHz/T, and $\epsilon = 4.75$.

First, for a YIG antiwire of radius R (putting $R_1 = R$ and $R_2 \to \infty$) and for the applied field $\mu_0 H_0 = 0.3$ T, we show in Fig. 4.1 the surface polariton frequencies versus wave number (in terms of the dimensionless qR) for the two lowest frequencies, which correspond to $|n| = 1$ and $|n| = 2$. We note that, as in the magnetostatic limit, there are no surface modes found for $n = 0$ because localization cannot be satisfied. For the smallest R (curves A) retardation effects are negligible and the results are essentially the same as given by the magnetostatic theory for the antiwire geometry (see Chapter 2 and [70, 82]). The frequencies decrease with increasing q
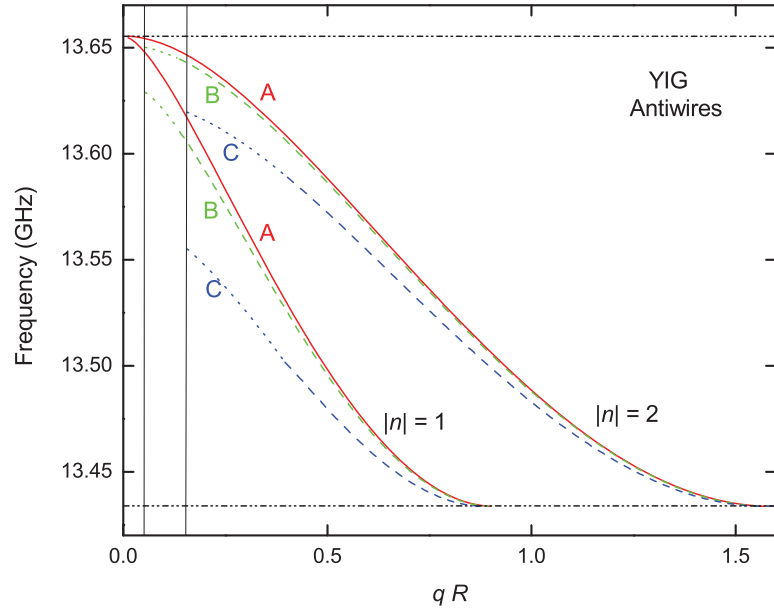
Figure 4.1: Frequencies of the surface polaritons with $|n| = 1$ and 2 in YIG antiwires versus qR for three values of the radius: (A) $R = 57$ μm; (B) $R = 1.1$ mm; (C) $R = 3.4$ mm. See the text for other notation.

until reaching a cut-off for localization. The maximum and minimum frequencies for the surface modes are indicated by the horizontal lines. As R is increased, the retardation effects become progressively more important in accordance with the criteria quoted earlier. This is the situation in cases B and C, and there are several important differences (compared with A) in the dispersion curves. First, the surface polaritons occur only to the right of the corresponding light line, which is defined by $\omega = cq$ and shown in Fig. 4.1 as a straight line with large gradient. Also the shapes of the dispersion curves are modified near the light line and the frequencies are reduced compared with the magnetostatic limit. This behavior is mainly a consequence of the localization of the surface modes being reduced due to retardation. The cut-off values, however, are only slightly modified since the
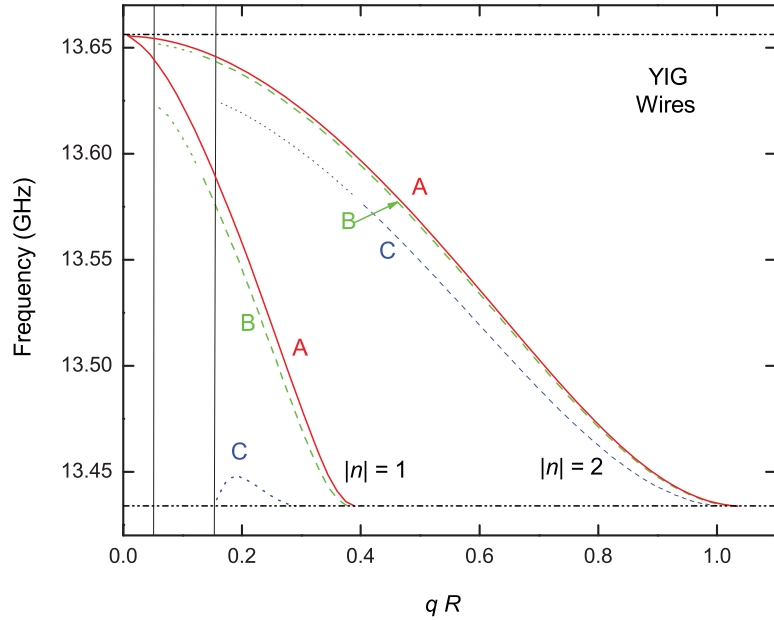
Figure 4.2: For comparison, the same as in Fig. 4.1 but for in YIG wires with the same radii.

retardation effects are less at larger q. The dispersion curves in the retarded cases are indicated using two different types of broken lines, depending on whether k_1 and k_2 are both imaginary (at larger qR) or just one of these quantities is imaginary (at smaller qR near the light line). Both situations correspond to localized modes, but in the latter case the fields oscillate as well as having a decaying amplitude with respect to distance from an interface.

The results for surface polaritons in YIG wires (taking $R_1 \to 0$ and $R_2 = R$) with $\mu_0 H_0 = 0.3$ T and the same radii are qualitatively rather similar, with the frequencies occurring within the same range. However, compared to antiwires, the cut-off qR values in wires are different due to the different localization properties (as might be expected from the magnetostatic limit [70]). Consequently the quantitative effects of retardation (e.g., the frequency shifts) when R is increased are different,
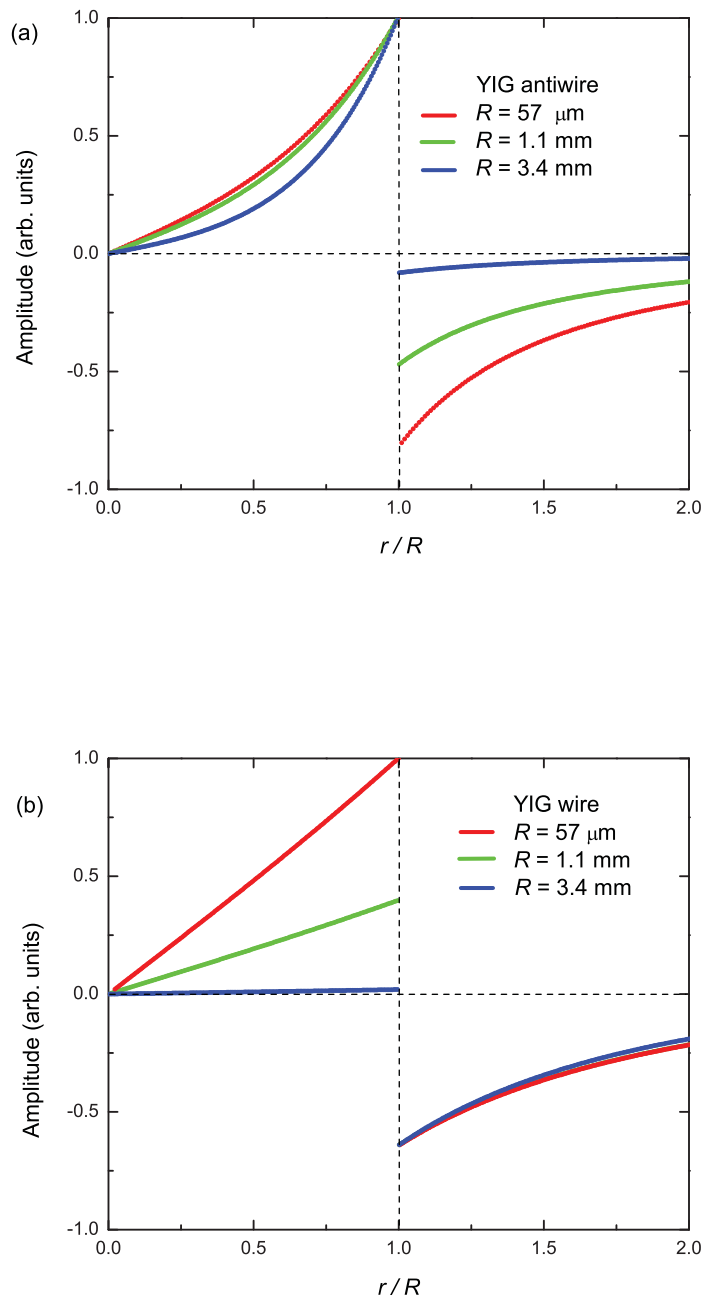
Figure 4.3: A plot of amplitude $H^r(r)$ for the lowest surface polariton mode ($|n| = 1$) versus r/R at applied field $\mu_0 H_0 = 0.3$ T and frequency $\omega/2\pi = 13.5$ GHz for (a) an antiwire and (b) a wire of YIG.

as can be seen by comparing Figs. 4.1 and 4.2. For example, the cut-off values for qR at about 0.8 and 1.5 for $n = 1$ and $n = 2$ for the antiwires in Fig. 4.1 occur near 0.3 and 1.0, respectively, for the corresponding wires in Fig. 4.2. We also see in the dispersion curves that the retardation effects decrease with the radius R of wires or antiwires, and for the size of $R = 57$ μm, we effectively reproduce the results for the surface magnetostatic modes.

Next we investigate the variations of the mode amplitudes with dimensionless r/R for YIG antiwires and wires, taking (for example) the mode frequency at $\omega/2\pi$ $= 13.5$ GHz, and the corresponding qR values deduced from the dispersion curves A, B and C in Figs. 4.1 and 4.2. We analyzed the radial function of different field components involved in Eqs. (4.9) (4.11) and (4.14) for the lowest frequency ($|n| = 1$) modes. The $H^r(r)$ mode amplitudes plotted in Fig. 4.3 show interesting features. They are strongly localized near the interface in the YIG antiwires or wires and decay with distance from the interface, by analogy with the discussion in Chapter 2 for the magnetostatic modes in nanotubes. When the radius R of the YIG antiwires or wires is reduced from 3.4 mm to 57 μm or less, the amplitude of modes increases and eventually become identical to the magnetostatic mode amplitudes. Also, our results highlight the substantial differences for the mode amplitudes in the antiwire and wire geometries.

In Fig. 4.4 we show some results for YIG tubes with $R_1 = 0.3R_2$ taking $\mu_0 H_0 =$ 0.2 T. The frequencies of the surface polaritons for $|n| = 1$ and 2 are plotted versus qR_2 for two tube sizes as indicated, showing different degrees of retardation. In this geometry, by contrast with the wire and antiwire cases, there are two surface modes for each $|n|$. A physical explanation is that these correspond to modes localized mainly at the inner or outer surface, by analogy with the magnetostatic limit (see Chapter 2 and [70]). Also, as in Figs. 4.1 and 4.2, the modes appear only to the right of their light line, have frequencies that decrease with increasing retardation
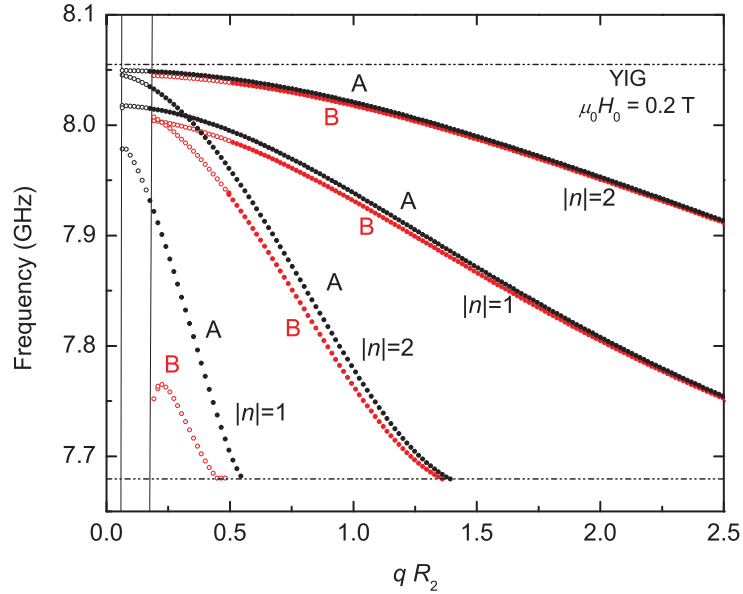
Figure 4.4: Frequencies of the surface polaritons in YIG tubes versus dimensionless qR_2 for two sizes: (A) $R_1 = 0.7$ mm and $R_2 = 2.3$ mm; (B) $R_1 = 2.1$ mm and $R_2 = 6.9$ mm.

for any given qR_2, and exist below the cut-off values of qR_2.

We have also considered F and AF tubes with both thin and thick walls in order to investigate the effect on the dynamics of surface polaritons. Here we illustrate our numerical calculations in Fig. 4.5 for YIG tubes, where surface mode frequencies for $|n| = 1$ and 2 are plotted as a function of R_1/R_2. The outer radius R_2 is kept fixed and the inner radius R_1 is varied (changing the wall thickness). By analogy with the magnetostatic example in Fig. 2.7, the mode frequencies lie between $(\omega_0 + \omega_m/2)$ and ω_B, which are marked as the two horizontal dotted lines in the figure. Starting with the limit of $R_1/R_2 \to 0$ (i.e., the wire), the $|n| = 2$ (and higher) modes are degenerate at the upper frequency bound, but split and reduce in frequency as R_1/R_2 increases. By contrast, the lowest ($|n| = 1$) mode has branches that show large frequency shifts due to retardation. When $R_1 \to R_2$, the retardation effect
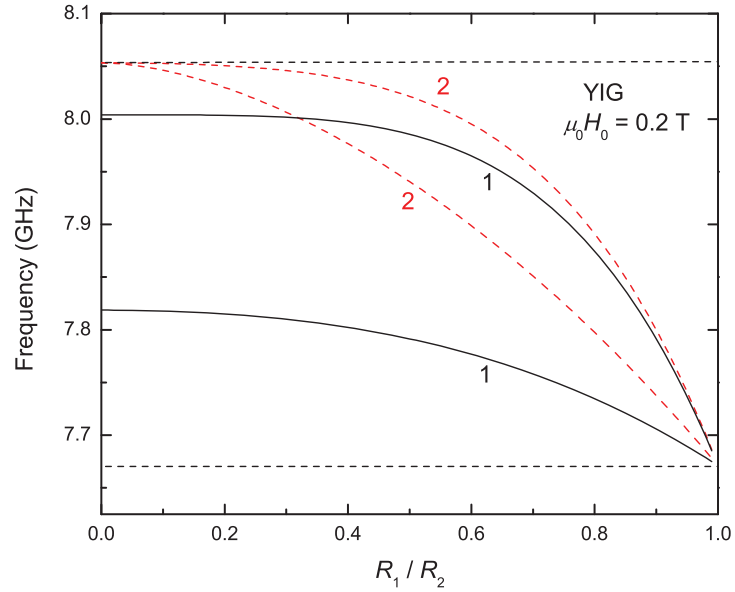
Figure 4.5: The surface polariton frequencies plotted versus R_1/R_2 for a YIG tube with $\mu_0 H_0 = 0.2$ T. The $|n| = 1$ and 2 modes are shown as black (solid) and red (dashed) lines respectively, when $qR_2 = 0.2$.

becomes minimal for these modes and, as a result, all these branches collapse towards the lower frequency bound, which was also the case found in Fig. 2.7.

For completeness, we next present some results for the frequency dispersion of bulk magnetic polaritons in a YIG tube. An applied field of 0.2 T and the appropriate YIG material parameters are used to solve the 8×8 determinant condition in Eq. (4.19). In order to display the effects of retardation on the bulk mode frequencies in the region $\omega_0 < \omega < \omega_B$ (see Fig. 2.2), we choose larger sizes of YIG tube taking R_1 = 10 mm and $R_2 = 34$ mm. In Fig. 4.6 we plot the dispersion curves only for the lowest seven branches (which come from $|n| = 0$, 1 and 2 modes). The frequencies of these branches are strongly reduced by retardation near the light line and no branches are found on the left side of the light line. Also, the group velocity of the retarded SW polaritons changes sign in some regions compared with the results for
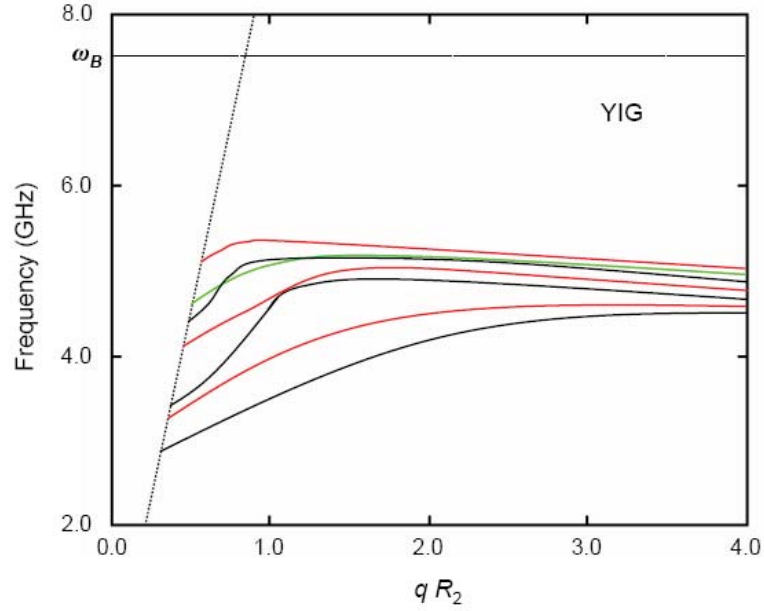
Figure 4.6: Frequencies of the lowest seven bulk polariton modes (which correspond to $|n| = 0$ (black), 1 (red) and 2 (green)) versus dimensionless qR_2 in a YIG nanotube. The inner and outer radii are 10 mm and 34 mm respectively and the applied field $\mu_0 H_0 = 0.2$ T.

bulk magnetostatic modes (see, e.g., Fig. 2.9).

Finally, some dispersion relations for AF wires of MnF_2 are shown in Fig. 4.7 using the parameters quoted previously. As in the earlier examples for YIG, the effects of retardation become more pronounced as R is increased. The existence of localized surface modes requires that $H_0 \neq 0$, so that the off-diagonal susceptibilty components in Eq. (4.1) are nonzero, and these modes occur in a narrow frequency regime intermediate between the two main regions for bulk polaritons. We also made calculations for FeF_2, which has a larger uniaxial anisotropy ($\mu_0 H_A = 19.7$ T) than MnF_2, but comparable exchange. As a consequence, the surface polaritons for FeF_2 occur at much higher frequencies (~ 1560 GHz) and in a very narrow band of width ~ 0.007 GHz. Otherwise the qualitative behavior for FeF_2 is similar to that in Fig. 4.7. Both of these AF materials have been used for experimental studies on
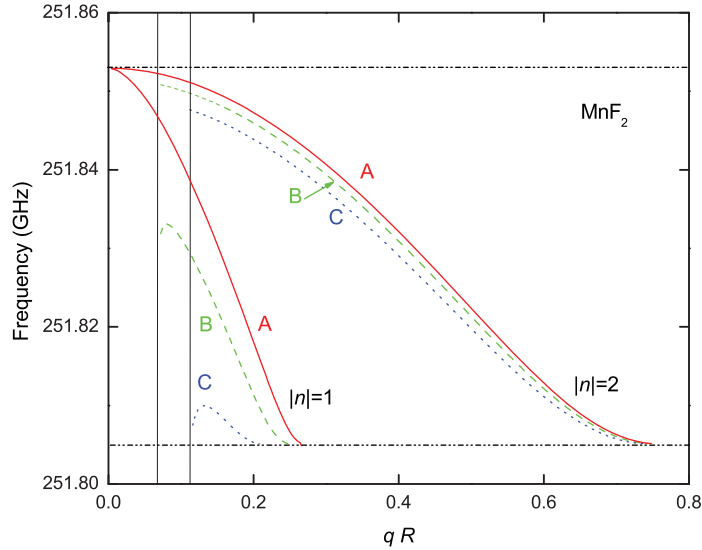
Figure 4.7: Frequencies of the surface polaritons in MnF_2 wires vs dimensionless qR for the applied field $\mu_0 H_0 = 0.3$ T and for three values of the radius: (A) $R = 1.7$ μm; (B) $R = 83$ mm; (C) $R = 132$ mm.

polaritons in thin films (see references in [35]), and are therefore suitable for similar experiments in cylindrical geometries.

4.4 Conclusions

We have developed a macroscopic continuum theory for the magnetic polariton spectra in tubes (with two interfaces) of F and AF materials, from which the limiting geometries of wires and antiwires (both single interface geometries) can be considered as special cases. The characteristic equations are derived by solving the full form of Maxwell's equations together with a non-diagonal frequency-dependent magnetic susceptibility tensor and a longitudinal applied field. In the AF case, it is the applied field that gives rise to off-diagonal components of the susceptibility tensor and causes a coupling between TE and TM modes in these

cylindrical geometries. By contrast with some previous calculations for AF wires in nonzero field [83] where an approximation was used to solve for TE or TM mode independently, our formalism has treated this coupling carefully. We solved the cylindrical form of Maxwell's equations for the magnetic and nonmagnetic layers of a tube and applied the electromagnetic boundary conditions at its inner and outer interfaces for both the electric and magnetic field components. This allowed us to derive theoretical dispersion relations for the surface and bulk polaritons which reduce correctly to the known magnetostatic limit (see Chapter 2) if the retardation effects become small (e.g., if the diameter is reduced).

In the dispersion curves of surface polaritons we have shown the degree of retardation and its effects on the SW dynamics by decreasing the radius of YIG antiwires or wires from the range of mm (large retardation) to μm (small retardation). Our results for a YIG wire are consistent with those in [107] derived for the special case of a F wire. We have found that the frequency of the surface polariton modes near the light line are reduced (compared to the magnetostatic limit), but this reduction depends on the specific geometry. Also, the variations of the mode amplitudes with radial distance were studied. The dispersion relations for surface polariton modes and their dependence on wall thickness were investigated for a YIG tube. We also made analogous calculations for MnF_2 and FeF_2 (AF) tubes. The limiting cases of wire and antiwires (as well as the behaviour in the magnetostatic limit) for zero and nonzero applied field were also analyzed in the AF case.

By analogy with the calculations for bulk and surface plasmon-polaritons propagating in arbitrary directions in planar semi-infinite semiconductor superlattices [111], our present theory of SW polaritons in tubes could be extended to cylindrical multilayers by following our transfer matrix analysis as in Sec. 2.4.

CHAPTER 5

Theory of Dipole-Exchange Spin Waves in Ferromagnetic Cylindrical Nanotubes.

(Some of the results in this chapter have been published in [112])

5.1 Introduction

Ferromagnetic nanowires and nanotubes, as well as arrays of these structures, have attracted much attention for their spin dynamics, e.g., in the development of magnonic analogs to photonic crystals [113] and in device applications [32, 72], as well as being of fundamental interest. In particular, BLS has proved to be a useful technique for probing the SW in these low-dimensional structures [32, 69, 113, 114], typically in the dipole-exchange regime. Most dipole-exchange studies have been applied to nanowires having a rectangular cross section (i.e., a F stripe geometry), as in [32, 114], and there has been relatively less attention given to long wires (and tubes) with a cylindrical geometry. Some exceptions are the BLS studies of quantized SW in wires [69] and tubes [60]. On the theoretical side, for cylindrical geometries, SW calculations in nanowires for the magnetostatic limit (at small wave numbers where the dynamical effects of exchange are negligible compared to dipole-dipole interactions) were made by Sharon and Maradudin [82] and later generalized by us to tubes and multi-interface structures (see Chapters 2 and 3, and [70, 71]).

Macroscopic dipole-exchange SW calculations for cylindrical wires have been reported [68] and then used in [69, 78] to study the SW dynamics in F nanowires, fabricated by electrodeposition in porous alumina templates and analyzed by BLS. The motivation for this chapter is to extend the macroscopic (or continuum) method

used in the earlier chapters to study the dipole-exchange SW (or DESW) in tubes, where additional quantization effects arise due to the two interfaces.

According to our general discussion in Chapter 1, the study of DESW excitations must include the interplay between the long range dipole-dipole interactions and the short range exchange interactions in the magnetization dynamics, as characterized by wavevectors such that typically $10^7 < q < 10^8$ m^{-1}. Following a similar procedure to that in [68] for a single interface F nanowire, we focus on applying the theory of DESW modes to F nanotubes (cylindrical geometries with two interfaces), including also the effects of a phenomenological damping. The magnetic modes within thin and thick walled nanotubes are described using both unpinned and effective pinned cases, together with the electromagnetic boundary conditions at the inner and outer interfaces. Our calculations describe the radial and angular quantization of the different modes in nanotubes and can be related to recent BLS experiments, e.g., in Ni nanotubes. The characteristic equations for the DESWs are deduced by a generalization of our results in Chapter 2 on multi-interface cylindrical magnetic geometries in situation where the dipole-dipole interactions were dominant (the magnetostatic regime). For limiting cases, our present calculations also simplify to describe the one interface geometries of DESWs in antiwires and wires.

We begin in Sec. 5.2 by describing our theoretical formalism where a frequency dependent response function is evaluated using the Landau-Lifshitz-Gilbert (LLG) equation and applied to the case of a F material in the presence of damping. Next, we use Maxwell's equations together with the response function to deduce and solve a sixth order differential equation for the magnetization dynamics. With the use of appropriate Bessel functions and the boundary conditions at the inner and outer interfaces of the nanotube, the solutions (using superposition) for the variable magnetization components and the DESW dispersion relations, as well as some limiting cases, are obtained. Following this, in Sec. 5.3 numerical calculations

are made for nanostructures of EuS and Ni including different pinning conditions and a phenomenological damping. Finally, in Sec. 5.4 we provide brief conclusions of the work in this chapter.

5.2 Analytic theory of dipole-exchange SW in a tube

As in Chapters 2 and 4, as well as Ref. [70], the model of nanotube in our present consideration is also an infinitely long, hollow magnetic cylinder (ignoring the end-effects) with inner radii $r = R_1$ and outer radii $r = R_2$. The regions $r < R_1$ and $r > R_2$ of the tube are filled with a nonmagnetic and the region $R_1 < r < R_2$ is filled with a F material. The case of an AF material could be treated in a similar fashion, but is slightly more complicated due to two-sublattice structure of a AF (as discussed in [115] for a film geometry). The limiting cases of wires ($R_1 \rightarrow 0$, $R_2 \neq 0$) and antiwires ($R_1 \neq 0$, $R_2 \rightarrow \infty$) are also of interest. In the previous chapters we emphasized the behaviour of SW excitations in the electromagnetic and the magnetostatic regimes where only the magnetic dipolar interaction played a major role in the SW dynamics. Here, the aim is to extend our previous theoretical investigations to the dipole-exchange regime, which includes both long range dipole-dipole and short range exchange interactions in the SW dynamics (see Chapter 1). With a longitudinal applied magnetic field we study the DESW modes propagating along the symmetry axis (z axis) and characterized by the wavevector q of magnitude 10^7 m^{-1} or larger.

In a theory of the DESW in a F nanotube, the dynamical response function for a F in Eqs. (1.15) and (1.16) must be re-derived with both dipolar and exchange effects present. We start from the Landau-Lifshitz torque equation with a phenomenological Gilbert damping term included [33], as quoted in Eq. (1.9). In our present case the total magnetization is $\overrightarrow{M} = M_0 \hat{z} + \overrightarrow{m}(\overrightarrow{r})e^{-i\omega t}$ with ω denoting the angular frequency of the SW and $|\overrightarrow{m}| << M_0$ in the linear SW regime. The

gyromagnetic ratio is γ and the total effective magnetic field is

$$\vec{H}_{eff} = H_0\hat{z} + \{\vec{h}_d(\vec{r}) + \vec{h}_{ex}(\vec{r})\}e^{-i\omega t}. \tag{5.1}$$

By analogy with Chapter 2 and Ref. [16], the dipolar field $\vec{h}_d$ is deduced from Maxwell's equations (without retardation) while the exchange field $\vec{h}_{ex}$ can be expressed in the form $\vec{h}_{ex} = -\lambda\vec{M} - (D/M_0)\nabla^2\vec{M}$ as in Eq. (1.11), where λ is a static exchange factor and D is the exchange stiffness constant. Finally, we remark that the inclusion here of a damping term, proportional to the dimensionless constant α_0 in Eq. (1.9), is important in the tube geometry (with its two interfaces) in order to get a more realistic description of the coupled SW modes and also to describe the wire and antiwire limiting cases.

Following dipole-exchange SW theories [68] for other geometric samples (see also Sec. 1.5.2), the calculation proceeds by substituting the $\vec{M}$ and $\vec{H}_{eff}$ terms into the LLG equation and linearizing the result in terms of $\vec{m}(\vec{r})$, i.e.,

$$-i\omega\vec{m}(\vec{r}) = -\omega_m\{\hat{z} \times \vec{h}_d(\vec{r}) + (\omega_0 - D\nabla^2 - i\alpha_0\omega)\{\hat{z} \times \vec{m}(\vec{r})\}, \tag{5.2}$$

which generalizes Eq. (1.26). Next, we use Eq.(5.2) and the magnetostatic form of Maxwell's equations, as in Chapter 2 to find the homogeneous differential equation for the magnetic scalar potential $\Psi(r, \theta, z)$ within the F layer of the tube, i.e.,

$$[(D\nabla^2 - \omega_0 + i\alpha_0\omega)\{D\nabla^2 - (\omega_m + \omega_0 - i\alpha_0\omega)\}]\nabla^2\Psi$$
$$-\omega^2\nabla^2\Psi + \omega_m(D\nabla^2 - \omega_0 + i\alpha_0\omega)\frac{\partial^2\Psi}{\partial z^2} = 0, \tag{5.3}$$

which is a generalization of the previous second order differential equation in Eq. (2.2), to what is now a sixth order differential equation. By analogy with [68] for other cylindrical geometries and the procedure established in our preceding chapters,

the magnetic scalar potential inside the F tube has a solution of the form $f_n(r)$ $\exp(in\theta) \exp(iqz)$, (e.g., as in Eq. (2.3)) where the integer n is the azimuthal quantum number and q is the wave number along the z axis of symmetry. The radial function f has the form of a linear combination of Bessel functions $I_n(\kappa r)$ and $K_n(\kappa r)$. However, instead of there being a single solution $\sqrt{\nu(\omega)}q$ for κ as previously in Eq. (2.5), we now find the following sixth order indicial equation after substituting the Bessel functions into Eq. (5.3):

$$(\kappa^2)^3 - X_1(\kappa^2)^2 + X_2\kappa^2 + X_3 = 0, \qquad (5.4)$$

with

$$
\begin{aligned}
X_1 &= \left(\frac{1}{D}\right)\left\{(3Dq^2 + 2\omega_0 + \omega_m) - i2\alpha_0\omega\right\}, \\
X_2 &= \left(\frac{1}{D^2}\right)\Big[\{3D^2q^4 + Dq^2(4\omega_0 + \omega_m) + \omega_0(\omega_0 + \omega_m) - \\
&\quad (1 + \alpha_0^2)\omega^2\} - i\alpha_0\omega(4Dq^2 + 2\omega_0 + \omega_m)\Big], \\
X_3 &= \left(\frac{1}{D^2}\right)\Big[-D^2q^6 - Dq^4(2\omega_0 + \omega_m) - \\
&\quad q^2\{\omega_0{}^2 - (1 + \alpha_0^2)\omega^2 - \omega_m Dq^2\} + i2\alpha_0\omega q^2(Dq^2 + \omega_0)\Big]. \qquad (5.5)
\end{aligned}
$$

Since Eq. (5.4) can be considered as a cubic equation in κ^2, there are three independent roots for κ in general and these can be denoted as κ_j (with $j = 1, 2, 3$). They depend on ω, q, H_0, M_0 and α_0, and they play the role of effective wave numbers in the radial direction. In general they are complex and contain information about the spatial localization and the degree of hybridization (mixing) of the modes. When the damping is small some of the κ_j are approximately real (with $\kappa_j{}^2 > 0$) for the localized surface modes and approximately pure imaginary (with $\kappa_j{}^2 < 0$) for the radial bulk modes, but they become complex in the regions of hybridization.
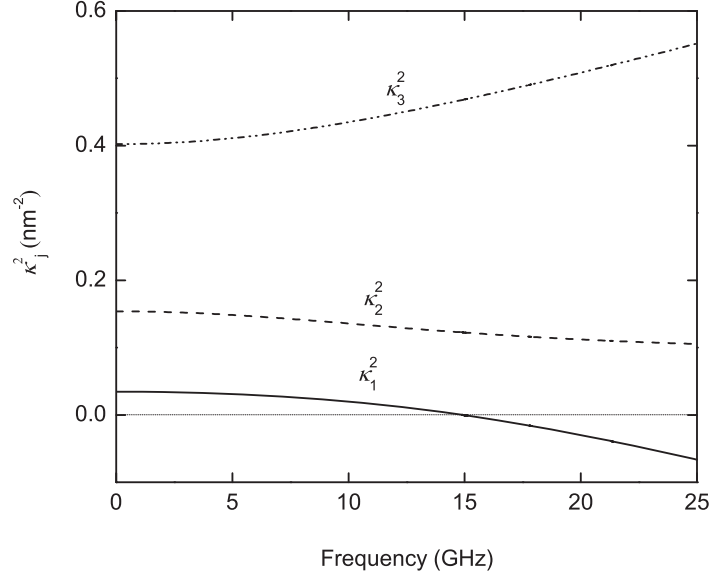
Figure 5.1: Variation of $\kappa_j{}^2$ with frequency for a F nanotube in the limit of zero damping $(\alpha_0 \to 0)$. We have chosen $q = 0.3$ nm^{-1}, $\omega_0 = 6.19$ GHz, $\omega_m = 18.66$ GHz, $D = 3.13$ T nm^2, as appropriate to Ni.

In Fig. 5.1 we show a plot of the real $\kappa_j{}^2$ versus frequency when $\alpha_0 \to 0$ in order to explain the physical nature for each wave number. The wave with $\kappa_1{}^2$ has decay-like characteristics in the frequency region where $\kappa_1{}^2$ is positive and an oscillatory bulk-like behaviour in the region where $\kappa_1{}^2$ is negative. The root $\kappa_2{}^2$ is always positive for the frequency range of interest, and its wave corresponds a localized surface mode. The wave related to $\kappa_3{}^2$ is a strongly localized surface mode as $\kappa_3{}^2$ is larger and positive. In the limiting case of $D \to 0$, the region of $\kappa_1{}^2 < 0$ dominates over the region of $\kappa_1{}^2 > 0$, which corresponds mostly to the oscillatory bulk modes, whereas the mode related to $\kappa_2{}^2$ shows the analogous magnetostatic surface modes (see [70]) and the other strongly localized surface wave does not have any analog to magnetostatic modes. These findings are analogous to those in [39] for the dipole-exchange SWs in the F thin-film geometry.

Generalizing our previous analysis in Chapter 2, the radial function $f_n(r)$ inside the magnetic material ($R_1 < r < R_2$) can be expressed as the form of a linear combinations of modified Bessel functions I_n and K_n, i.e.,

$$f_n(r) = \sum_{j=1}^{3} \left\{ a_j I_n(\kappa_j r) + b_j K_n(\kappa_j r) \right\}, \tag{5.6}$$

where a_1, a_2, a_3, b_1, b_2 and b_3 are unknown coefficients.

After some lengthy but straightforward algebra, the transverse components for $\vec{m}(r, \theta, z)$ inside the magnetic material take the form

$$m_r(r, \theta, z) = -\frac{\omega_m}{2} \exp[i(n\theta + qz)] \sum_{j=1}^{3} \kappa_j$$
$$\left\{ \frac{a_j I_{n+1}(\kappa_j r) + b_j K_{n+1}(\kappa_j r)}{\omega_0 + D(q^2 - \kappa_j{}^2) + (1 - i\alpha_0)\omega} + \frac{a_j I_{n-1}(\kappa_j r) + b_j K_{n-1}(\kappa_j r)}{\omega_0 + D(q^2 - \kappa_j{}^2) - (1 + i\alpha_0)\omega} \right\}, \tag{5.7}$$

and

$$m_\theta(r, \theta, z) = i\frac{\omega_m}{2} \exp[i(n\theta + qz)] \sum_{j=1}^{3} \kappa_j$$
$$\left\{ \frac{a_j I_{n+1}(\kappa_j r) - b_j K_{n+1}(\kappa_j r)}{\omega_0 + D(q^2 - \kappa_j{}^2) + (1 - i\alpha_0)\omega} - \frac{a_j I_{n-1}(\kappa_j r) - b_j K_{n-1}(\kappa_j r)}{\omega_0 + D(q^2 - \kappa_j{}^2) - (1 + i\alpha_0)\omega} \right\}. \tag{5.8}$$

Using the above results together with Eq. (5.2), we can also derive the generalized form of Eqs. (1.16) and (1.17) for the scalar representation of the susceptibility tensor components χ_a and χ_b as

$$\chi^{\pm} = \frac{\omega_m\{(\omega_0 + D(q^2 - \kappa_j{}^2) \mp \omega) + i\alpha_0\omega\}}{\{\omega_0 + D(q^2 - \kappa_j{}^2) \mp \omega\}^2 + (\alpha_0\omega)^2}, \tag{5.9}$$

for the mode labelled j. Here, the exchange (through D) and the damping (through α_0) modify the pole in the denominator of $\chi^{\pm}$, as can be seen by comparing with Eqs. (1.16) and (1.17). This causes a frequency shift in the response function for
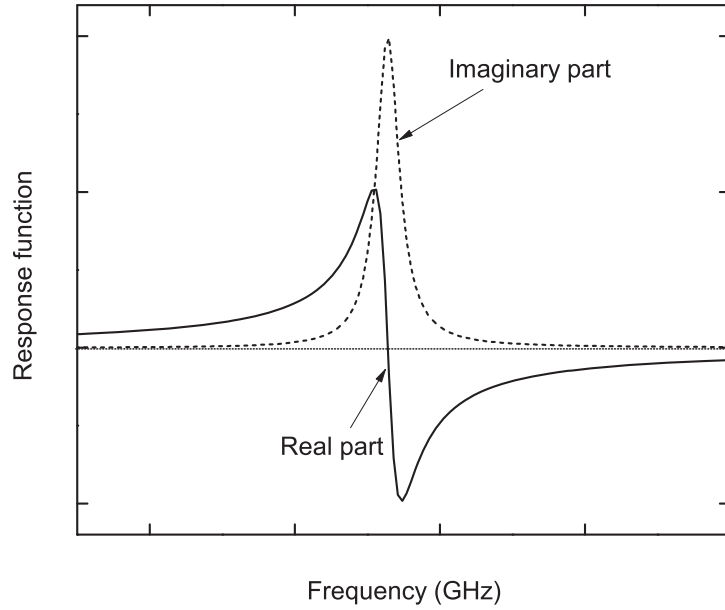
Figure 5.2: Schematic diagram of susceptibility function vs. frequency for a F material with Gilbert damping.

a F material, making it interesting to probe the SW experimentally using FMR or BLS. To estimate this shift, the admixture of κ_j terms with weighting factors must be determined using the boundary conditions at the inner and outer interfaces of the tube, as will be discussed later in this section and illustrated numerically in Sec. 5.3. At this stage, for the limit of $D \to 0$ but with damping included, the variation of the complex susceptibility function χ_a with frequency is plotted in Fig. 5.2. The mathematical divergence of this function near the resonance frequency (see Chapter 2) for a F material is removed when the Gilbert damping term is included, so the real (or dispersive) part of this response function is finite while the imaginary (or absorptive) part has a Lorentzian line shape, as shown in Fig. 5.2. This can be used to calculate the FMR line width at half-maximum. From the imaginary part of Eq. (5.9), the full resonance line width at half-maximum is $\triangle H = 2\omega\alpha_0/\gamma\mu_0$ where

we follow the FMR convention of expressing the result in magnetic field terms (see [33]).

Taking account of the dipolar fields in the nonmagnetic core ($r < R_1$) and external ($r > R_2$) regions, the magnetostatic scalar potential Ψ can be expressed by analogy with Eqs. (2.7) and (2.8), as

$$\Psi_n(r,\theta,z) = \begin{cases} c_1 I_n(qr)\exp[i(n\theta+qz)] & (r < R_1) \\ d_3 K_n(qr)\exp[i(n\theta+qz)] & (r > R_2) \ , \end{cases} \quad (5.10)$$

where c_1 and d_3 are unknown coefficients.

Next, we apply the boundary conditions at the R_1 and R_2 interfaces of the nanotube to determine the degree of mixing for the DESW. There are eight unknown coefficients c_1, a_1, a_2, a_3, b_1, b_2, a_3 and d_3 involve in Eqs (5.6), (5.7), (5.8) and (5.10). By contrast with our earlier calculation of magnetostatic modes in nanotubes, the two magnetostatic boundary conditions (see Chapter 2) will not be sufficient to determine all the eight unknowns. Two additional boundary conditions must now be considered based on the spatial inhomogeneity in the r.f. magnetization components near the interfaces. Based on the influence of exchange coupling and the effective pinning by the inhomogeneities in the dynamic magnetization fields at the interfaces, there are two extreme situations to take into account. One corresponds to 'zero pinning' where the DESW has an amplitude maximum at each interface (i.e., an antinode), while the other corresponds to 'strong pinning' with zero amplitude at each interface (i.e., a node). These two cases are shown schematically as in Fig. 5.3 for a F film with spatial quantization of the bulk SW (see [16]).

These considerations, which have been extensively discussed in the literature, lead us to consider two additional effective boundary conditions for the transverse magnetization components, one for m_θ and one for m_r, at each interface R_l ($l = 1$,

(a)   (b)
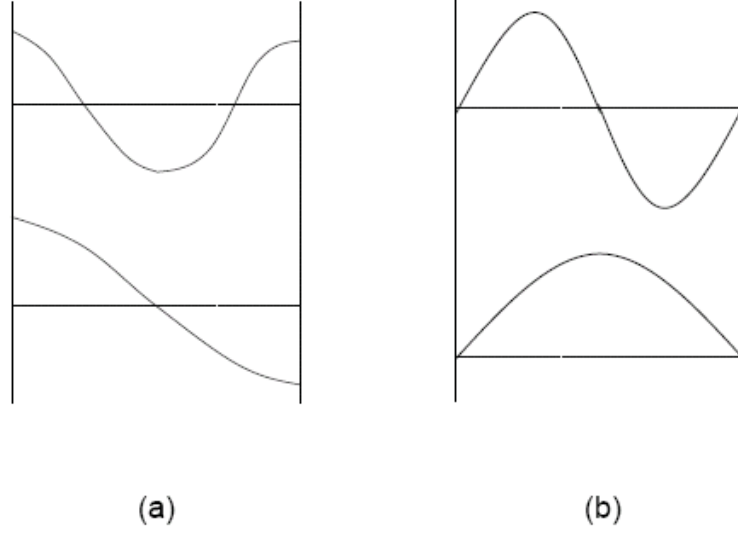
Figure 5.3: Schematic plots of some bulk SW amplitudes in a F film for (a) zero surface
           pinning and (b) strong surface pinning.

2):

$$\left[\frac{\partial m_\theta(r, \theta, z)}{\partial r}\right]_{r=R_l} = 0, \tag{5.11}$$

$$\left[\frac{\partial m_r(r, \theta, z)}{\partial r} + \eta_l m_r(r, \theta, z)\right]_{r=R_l} = 0, \tag{5.12}$$

which are analogous to the form deduced in [68, 116]. Here, the η_l coefficients (for $l =$ 1, 2) in Eq. (5.11) can be used as fitting parameters, or effective pinning constants, for the two interfaces of the F tube. Two limiting cases are often used: one is the Rado and Weertmann type unpinned boundary condition [117] taking $\eta_l \to 0$ and the other is the Kittel type strongly pinned boundary condition [25] taking $\eta_l \to \infty$.

We now employ these four boundary conditions at each interface of the nanotube, giving us eight homogeneous linear equations for the eight unknown coefficients that appear in the expressions for the magnetostatic scalar potential and

the transverse magnetization components. The elimination of these amplitude co-efficients will give rise to the vanishing of an 8×8 determinant, which yields the implicit dispersion relation of the DESW modes as

$$
\begin{vmatrix}
\Lambda_n^{\ 1}(\omega, q, R_1) & \Pi_n^{\ 1}(\omega, q, R_1) \\
\Lambda_n^{\ 2}(\omega, q, R_2) & \Pi_n^{\ 2}(\omega, q, R_2)
\end{vmatrix}
\;=\; 0 \, . \tag{5.13}
$$

Here Λ and Π are blocks representing the 4×4 matrices defined by

$$
\Lambda_n^{\ \iota} \;=\;
\begin{bmatrix}
\delta_{1,\iota} I_n(kR_\iota) & p_{1\iota} & p_{2\iota} & p_{3\iota} \\
\delta_{1,\iota} kR_1 I_n'(kR_\iota) & p_{1\iota}\Phi_{K_{1\iota}} & p_{2\iota}\Phi_{K_{2\iota}} & p_{3\iota}\Phi_{K_{3\iota}} \\
0 & 2\omega\Psi_{K_{1\iota}} - \Upsilon_{K_{1\iota}} & 2\omega\Psi_{K_{2\iota}} - \Upsilon_{K_{2\iota}} & 2\omega\Psi_{K_{3\iota}} - \Upsilon_{K_{3\iota}} \\
0 & 2\Omega_1\Psi_{K_{1\iota}} - \Upsilon_{K_{1\iota}} & 2\Omega_2\Psi_{K_{2\iota}} - \Upsilon_{K_{2\iota}} & 2\Omega_3\Psi_{K_{3\iota}} - \Upsilon_{K_{3\iota}}
\end{bmatrix}
\tag{5.14}
$$

where label ι can be 1 or 0. Other quantities introduced here are

$$
p_{j\iota} = K_n(\kappa_j R_\iota), \quad \Phi_{K_{j\iota}} = (1 + \chi_a)\kappa_j R_\iota \frac{K_n'(\kappa_j R_\iota)}{K_n(\kappa_j R_\iota)} \pm n\chi_b,
$$

$$
\Psi_{K_{j\iota}} = \frac{1}{T_j}\left[\kappa_j^2\left\{ -K_{n+2}(\kappa_j R_\iota) + \left(\frac{n+1}{\kappa_j R_\iota}\right)K_{n+1}(\kappa_j R_\iota)\right\} + \varrho_\iota\kappa_j K_{n+1}(\kappa_j R_\iota)\right],
$$

$$
\Upsilon_{K_{j\iota}} = \frac{K_n(\kappa_j R_\iota)}{Q_j}\left[\frac{2n}{R_\iota^2}\left\{\kappa_j R_\iota \frac{K_n'(\kappa_j R_\iota)}{K_n(\kappa_j R_\iota)} - 1\right\} + \frac{2n\varrho_\iota}{R_\iota}\right],
$$

$$
\Omega_j = \left\{\omega_0 + D(k^2 - \kappa_j^2) - i\alpha\omega\right\}, \quad T_j = \Omega_j^2 - \omega^2, \quad Q_j = \Omega_j - \omega. \tag{5.15}
$$

Similarly, the other block appearing in Eq. (5.13) is

$$
\Pi_n{}^\iota \;=\; \begin{bmatrix} q_{1\iota} & q_{2\iota} & q_{3\iota} & \delta_{2,\iota} K_n(kR_\iota) \\[4pt] q_{1\iota}\Phi_{I_{1\iota}} & q_{2\iota}\Phi_{I_{2\iota}} & q_{3\iota}\Phi_{I_{3\iota}} & \delta_{2,\iota} kR_1 K_n{}'(kR_\iota) \\[4pt] -2\omega\Psi_{I_{1\iota}} - \Upsilon_{I_{1\iota}} & -2\omega\Psi_{I_{2\iota}} - \Upsilon_{I_{2\iota}} & -2\omega\Psi_{I_{3\iota}} - \Upsilon_{I_{3\iota}} & 0 \\[4pt] -2\Omega_1\Psi_{I_{1\iota}} - \Upsilon_{I_{1\iota}} & -2\Omega_2\Psi_{I_{2\iota}} - \Upsilon_{I_{2\iota}} & -2\Omega_3\Psi_{I_{3\iota}} - \Upsilon_{I_{3\iota}} & 0 \end{bmatrix}
$$

$$(5.16)$$

with

$$
q_{j\iota} = I_n(\kappa_j R_\iota), \quad \Phi_{I_{j\iota}} = (1+\chi_a)\kappa_j R_\iota \frac{I_n{}'(\kappa_j R_\iota)}{I_n(\kappa_j R_\iota)} \pm n\chi_b,
$$

$$
\Psi_{I_{j\iota}} = \frac{1}{T_j}\left[\kappa_j{}^2\left\{I_{n+2}(\kappa_j R_\iota) + \left(\frac{n+1}{\kappa_j R_\iota}\right)I_{n+1}(\kappa_j R_\iota)\right\} + \varrho_\iota\kappa_j I_{n+1}(\kappa_j R_\iota)\right],
$$

$$
\Upsilon_{I_{j\iota}} = \frac{I_n(\kappa_j R_\iota)}{Q_j}\left[\frac{2n}{R_\iota{}^2}\left\{\kappa_j R_\iota \frac{I_n{}'(\kappa_j R_\iota)}{I_n(\kappa_j R_\iota)} - 1\right\} + \frac{2n\varrho_\iota}{R_\iota}\right]. \tag{5.17}
$$

We employ the characteristic equation expressed in Eq. (5.13) to make numerical applications in the next section.

It is noteworthy that our formalism deals correctly with the special limiting cases of exchange-dominated modes (taking $M_0 \to 0$) and magnetostatic modes (taking $D \to 0$) in the tube geometry. Results for the exchange limit are found by deducing the effective radial wave vector, which simplifies to have just one solution:

$$
\kappa \;=\; \{(1/D)(Dq^2 + \omega(1 - i\eta) + \omega_0)\}^{1/2}. \tag{5.18}
$$

The appropriate form of solutions for the transverse magnetization components using Eqs. (5.7) and (5.8) and the effective exchange boundary condition at the inner and outer interfaces are applied to derive the characteristic equation for the exchange

SW modes in a nanotube as

$$
\begin{vmatrix}
\Phi_{I1} I_n(\kappa R_1)/R_1 & \Phi_{K1} K_n(\kappa R_1)/R_1 \\
\Phi_{I2} I_n(\kappa R_2)/R_2 & \Phi_{K2} K_n(\kappa R_2)/R_2
\end{vmatrix} = 0 \, , \tag{5.19}
$$

where $\Phi_{Ij} = \{\kappa R_j I_{n+1}(\kappa R_j)\}/I_n(\kappa R_j) + n + \eta_j$, for $j = 1, 2$. Similarly, the term Φ_{Kj} can be obtained by replacing Bessel function I_n by Bessel function K_n in Φ_{Ij}. Likewise, we can recover the characteristic equation for the magnetostatic limit by deducing the effective radial wave number. As we have shown, one of effective radial wave numbers κ_2 shows the exact behaviour of the radial wave number $\sqrt{\nu(\omega)}q$ discussed in Chapter 2 for a F material when $D \to 0$ and $\alpha_0 \to 0$. The 8×8 determinant condition in Eq. (5.13) then reduces to the exact form of 4×4 determinant expressed in Eq. (2.11) for the magnetostatic modes in a nanotube.

By analogy with our earlier calculations, we also find a reduction of the 8×8 determinant in Eq. (5.13) to 4×4 determinant conditions in both of the limiting cases of the antiwire and wire geometries. In the limit of an antiwire, the expression involves the 4×4 matrix Λ (see Eq. (5.14)) as derived by taking $R_2 \to \infty$ and R_1 non-zero. Similarly, in the limit of a wire (taking $R_1 \to 0$ and finite R_2), our results is in terms of the 4×4 matrix Π (see Eq.(5.16)), which generalizes the previous wire DESW calculations [68] to include damping.

5.3 Numerical results

Numerical calculations are now carried out by solving the implicit dispersion relation Eq. (5.13) for the hybridized DESW modes in a nanotube, considering also some limiting cases. Specific numerical examples (mainly for the dispersion relations, the variation of SW frequency with sample radius, and the frequency-dependent response functions) are given, with comparisons made between weak and strong pinning. Applications are made for two F materials, namely EuS and Ni.

The relevant parameters are well known: we take $\mu_0 M_0 = 1.53$ T, $D = 0.20$ T-nm^2, and $\gamma = 28.0$ GHz/T for EuS, with $\mu_0 M_0 = 0.603$ T, $D = 3.13$ T-nm^2, and $\gamma = 30.9$ GHz/T for Ni. Ni nanotubes are included since this magnetic material was employed in BLS experiments [60, 69]. EuS (where the exchange effects are less pronounced) has also been previously studied using BLS, but in a film geometry [118]. In most of our examples a small damping constant ($\alpha_0 = 0.001$) is included, since it is helpful for numerical stability, but we also explore the role of damping by considering larger α_0. For simplicity, we begin with the single interface cases of antiwires and wires, making comparisons between the two geometries.

In Fig. 5.4 we show numerical results to compare the lowest $|n| = 1$ SW frequencies versus longitudinal wave number q for a EuS anti-nanowire and its corresponding nanowire. In both cases, results are presented for a radius $R = 20$ nm and for two cases, realizing weak and stronger pinning, namely $\eta = 0$ and $\eta = 4$. We observe that the DESW modes are strongly influenced by the pinning condition, especially in the antiwire case. A comparison with the surface magnetostatic mode (which lies between upper and lower bounds [70] indicated by the horizontal lines) is included, and it can be seen that the exchange-dominated bulk DESW branches (which are relatively flat in this wave number region) are strongly perturbed and hybridized in the vicinity of the magnetostatic branch. This effect is particularly pronounced in the antiwire case.

Next we investigate the frequency dependence of the lowest DESW mode ($|n| = 1$) on the radius R for Ni antiwires and wires, taking material parameters as given earlier. Also we use $\mu_0 H_0 = 0.3$ T, $\alpha_0 = 0.001$ and zero pinning. By choosing three values for the longitudinal wave number, namely $q = 0.007$ nm^{-1}, 0.041 nm^{-1} and 0.3 nm^{-1}, which are typical of the magnetostatic, dipole-exchange and exchange regions respectively of SW excitations (see Chapter 1), we find the results presented in Fig. 5.5. The behaviour in antiwires and wires is now rather similar, with both showing
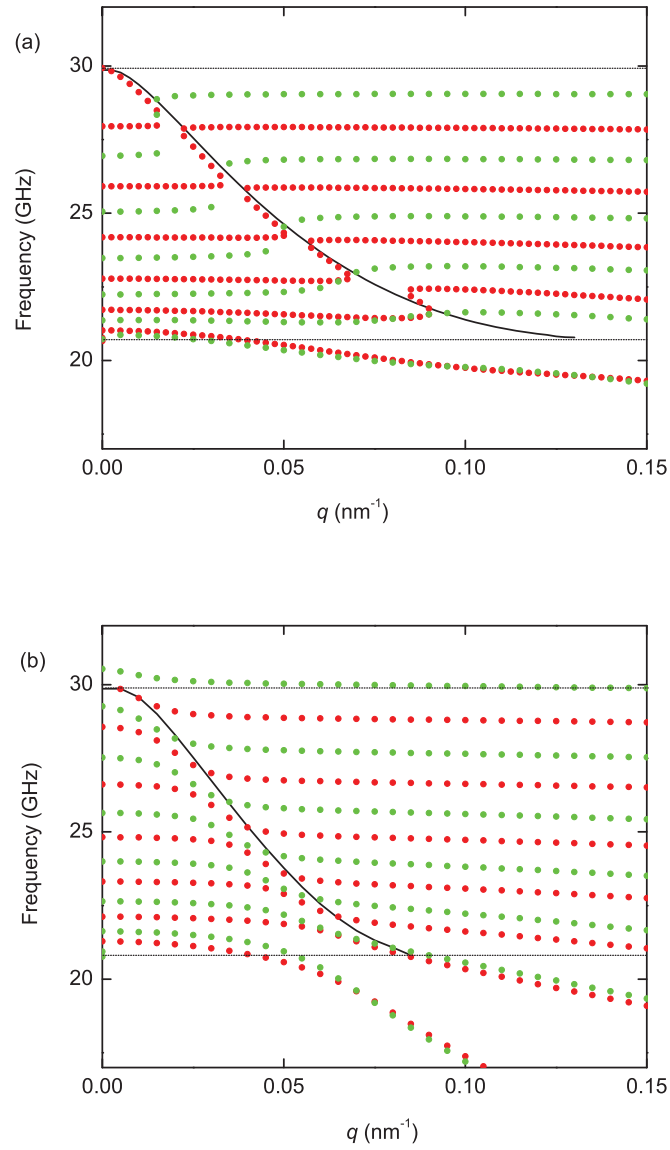
Figure 5.4: Frequencies of the DESW with $|n| = 1$ versus longitudinal wave number q with the unpinned (red circle) and pinned (green circle) cases for a EuS (a) antiwire and (b) wire. For comparison, dispersion curves for the surface magnetostatic modes are shown by the solid line. Also $\mu_0 H_0 = 0.3$ T, $\alpha_0 = 0.001$ and radius $R = 20$ nm.
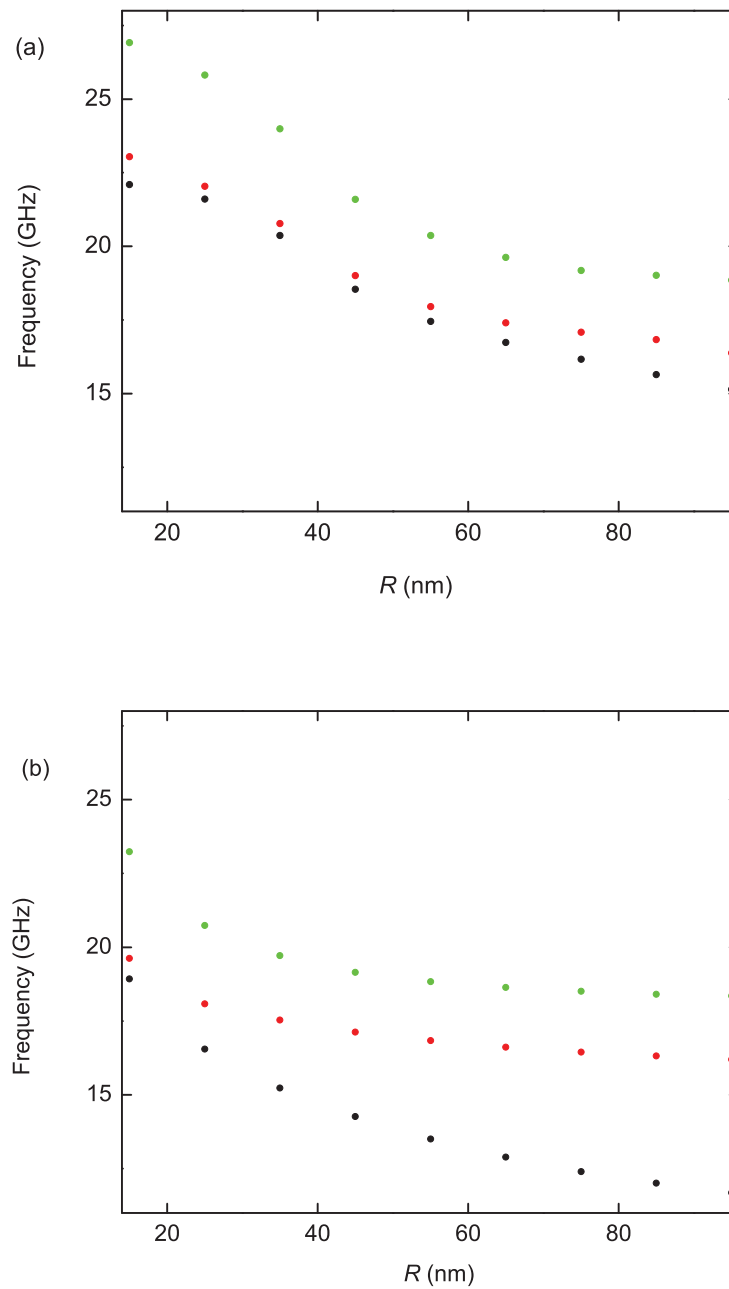
Figure 5.5: DESW frequency with $|n| = 1$ versus radius R taking fixed q values of 0.007 nm^{-1} (black circle), 0.041 nm^{-1} (red circle) and 0.3 nm^{-1} (green circle) for the unpinned case of a Ni (a) antiwire and (b) wire. Other parameters are given in the text.
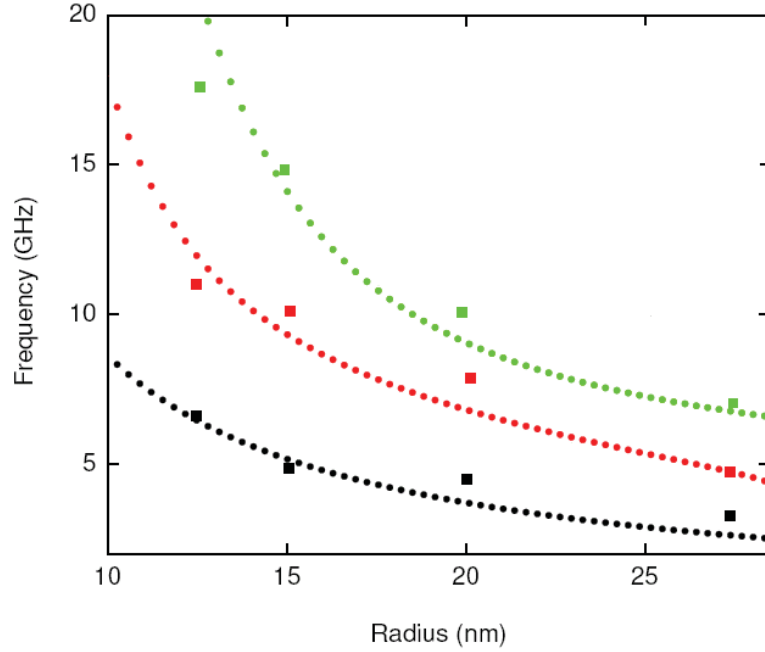
Figure 5.6: Dependence of DESW frequencies on the radius of Ni wires for $|n| = 1$ (black circle), 2 (red circle) and 3 (green circle). Other parameters used are $q = 0.041$ nm^{-1} and $\mu_0 H_0 = 0$ T. The squares represent experimental data [69].

a frequency reduction as R is increased. However, the frequencies are different in the two structures due to the different localization of the modes. For example, the frequency of SW corresponding to $q = 0.041$ nm^{-1} at $R = 25$ nm is 22.0 GHz for a Ni antiwire, whereas it is 18.1 GHz for the same size of Ni wire.

To compare our theory with the experimental BLS data for Ni wires in [69], we present results for the DESW frequencies versus wire radius. Results for the lowest $|n| = 1$, 2 and 3 modes are shown in Fig. 5.6, where the radius R varies in the range from 10 to 30 nm and a comparison is made with the experimental data [69] for $q = 0.041$ nm^{-1} and $H_0 = 0$. Good agreement between experiment and theory is found when the pinning is such that $\eta = 1.96$. This confirms that a DESW theory

is required to calculate the SW properties in nm-sized cylindrical geometries and it gives the first prediction a value for the pinning parameter.

Next we present numerical results for the DESW frequencies in nanotubes, starting with EuS and taking $R_2/R_1 = 2$. The dispersion relations of the lowest $|n|$ $= 1$ mode are shown in Fig. 5.7 where the mode frequencies are plotted versus q for zero and strong pinning (assumed to be the same at both interfaces). Corresponding to the limit of $D \to 0$, the two surface magnetostatic branches are shown as the full curves (consistent with Chapter 2), with one mode being mainly associated with the inner interface and the other mainly with the outer interface. The exchange effects are relatively weak for EuS, which is especially evident in Fig. 5.7 (a) for the zero pinning case where there are several "exchange-dominated" radially-quantized modes that become hybridized in the vicinity of modified surface magnetic modes [112]. In the strong pinning case of Fig. 5.7(b), it is clear that the mode hybridization near the outer interface of the tube can considerably modify the surface branch localized there (which is analogous to the wire), but there is a lesser effect for the inner interface (which is analogous to the antiwire). By analogy with our previous discussion for the single interface geometries, we have also confirmed that effective pinning causes significant changes in the mode mixing and localization near the inner interface of a EuS tube.

Next in Fig. 5.8 we consider a EuS nanotube with the same R_1 and R_2 values and zero pinning (as in Fig. 5.7(a)), but with a larger damping constant $\alpha_0 = 0.02$. We see that the variation of the $|n| = 1$ mode frequencies with the wave vector q is qualitatively similar to Fig. 5.7(a). However, the lowest "exchange-dominated" radially-quantized modes are reduced in frequency and the effects of hybridization are more apparent.

For further comparison with Fig. 5.7(a), the dispersion relations are presented in Fig. 5.9 for a Ni nanotube with $R_1 = 15$ nm and $R_2 = 30$ nm, taking $|n| = 1$
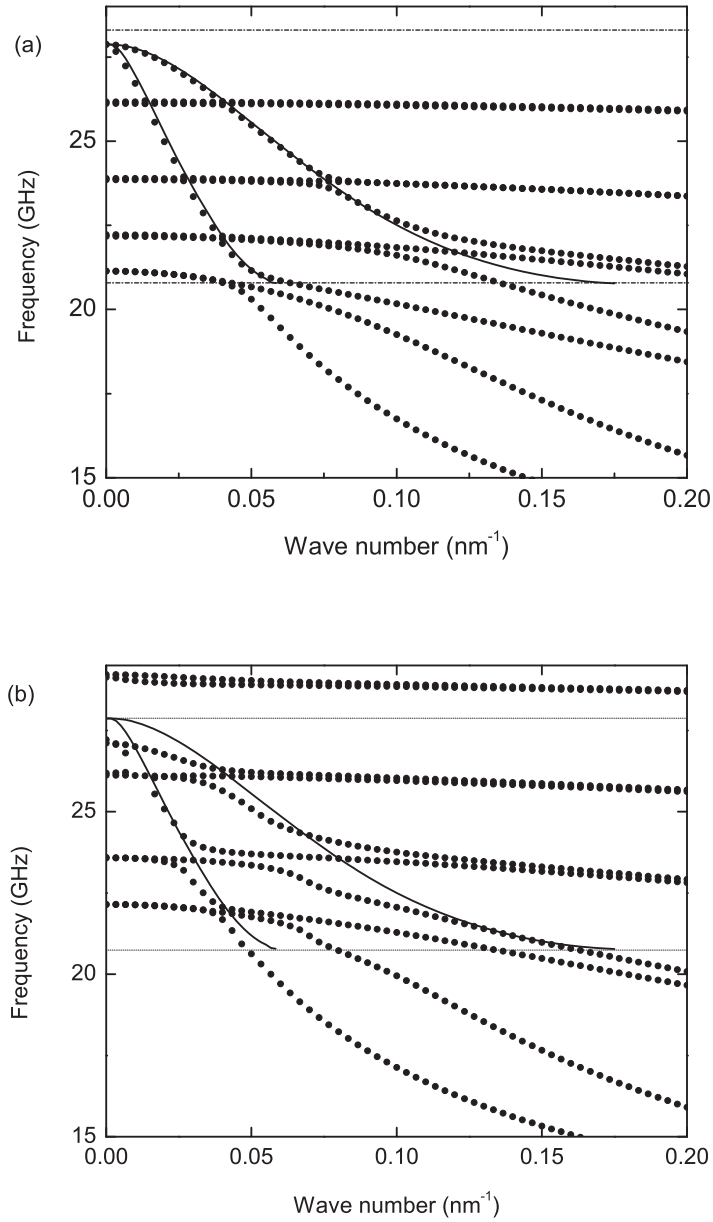
Figure 5.7: The hybridized SW frequencies versus wave number q for a tube with $R_1 = 15$ nm and $R_2 = 30$ nm in the case of (a) unpinned and (b) pinned surface surface spins. The DESW frequencies correspond to the circles and, for comparison, the surface magnetostatic modes are represented by the solid lines. Also, $\mu_0 H_0 = 0.3$ T, $\alpha_0 = 0.001$, and $|n| = 1$.
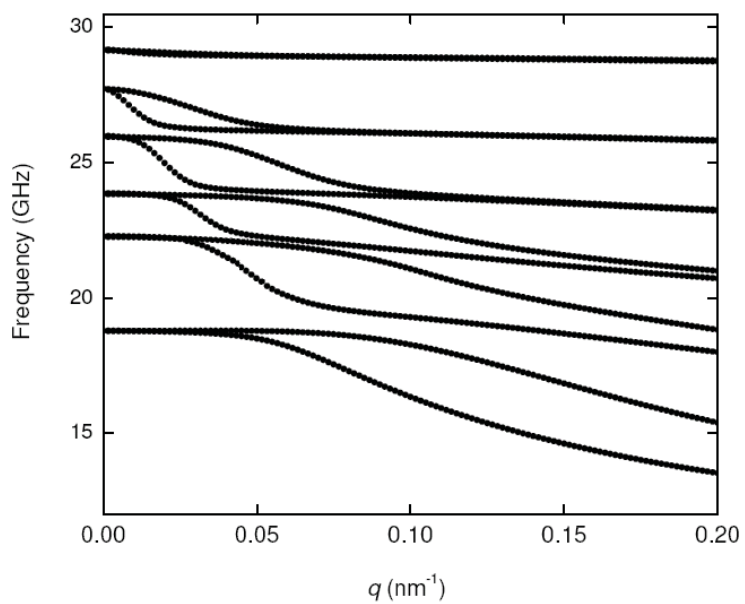
Figure 5.8: The same as in Fig. 5.7(a), but taking the damping constant $\alpha_0 = 0.02$.
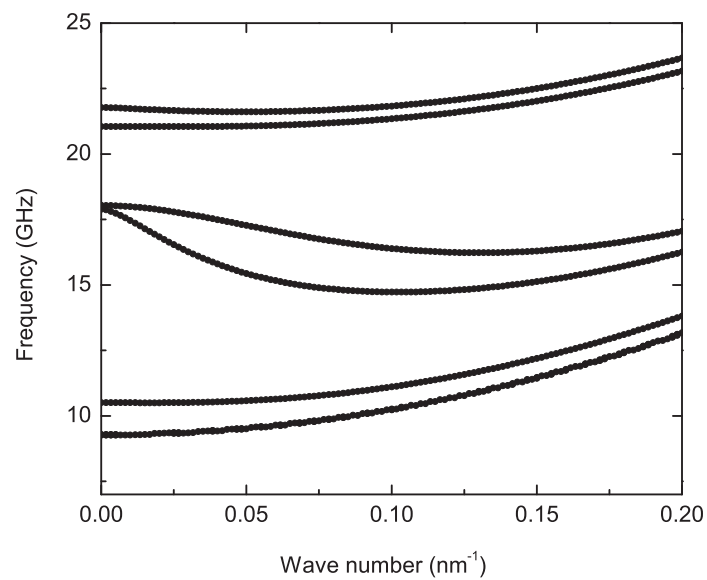
Figure 5.9: The same as in Fig. 5.8, but for a Ni nanotube with zero pinning, taking the damping constant $\alpha_0 = 0.001$.
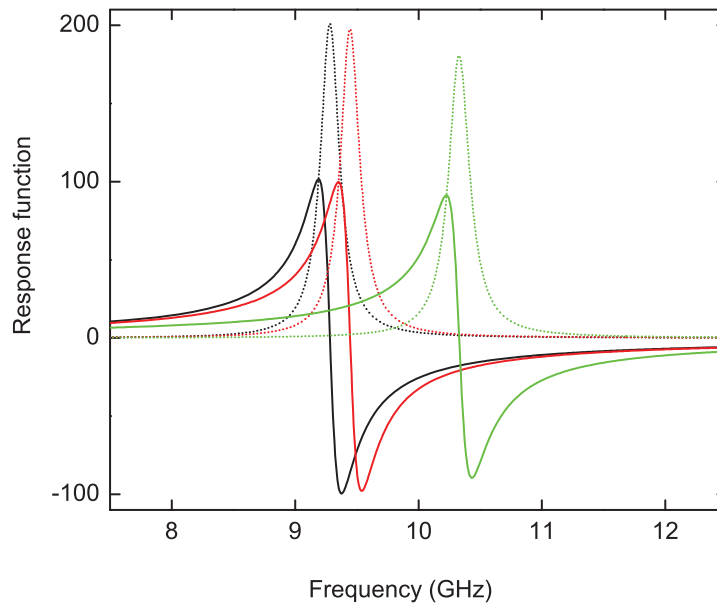
Figure 5.10: The real (solid line) and imaginary (dash line) parts of response func-
tion χ_a versus frequency for a Ni nanotube, varying $D = 0.003$ T nm^2
(black), 3.13 T nm^2 (red) and 20.13 T nm^2 (green). The other param-
eters are the same as in Fig. 5.9, but taking $q = 0.041$ nm^{-1} and $\alpha_0 =$
0.01.

and $\alpha_0 = 0.001$. The effects of exchange are stronger in Ni and so, by contrast with
the magnetostatic modes in tubes (see Chapter 2), the analogous DESW are shifted
upwards and eventually have a positive slope due to the exchange. This effect is
found to be more evident for modes associated with the outer interface compared
to the inner interface of the tube as a result of the higher mode localization in
the former case. In addition, there are exchange-type bulk modes (with positive
slope) in other frequency regions. Due to the larger exchange stiffness constant, the
radially quantized exchange modes become more separated in frequency, compared
to the results presented in Fig. 5.7(a).

Finally, as another illustration of the exchange-dependence of DESW, we plot

χ_a, deduced from Eq. (5.9), as a function of frequency in Fig. 5.10. Here we take $\mu_0 H_0 = 0.3$ T, $\alpha_0 = 0.01$, $q = 0.041$ nm^{-1}, and with other parameters chosen as for Ni except that we vary D. Recall that in Sec. 5.2 we gave a simple expression in the absence of exchange for the full resonance line width at half-maximum. In the case of DESW excitations, the expression for the line width becomes much more complicated, and we now use Fig. 5.10 to show its variation (and shift) with D. These calculations are carried out for three values of D, i.e., 0.003 T nm^2, 3.13 T nm^2 and 20.13 T nm^2, where the second value is typical of Ni. As is seen, the FMR frequency gets shifted and also the amplitude of the response function varies.

5.4 Conclusions

In this chapter, we have developed a general theory for the DESW in nanotubes, as well as in the limiting cases of wires and antiwires, and we have shown some numerical examples of dispersion relations for Ni and EuS at wave numbers typical of BLS experiments. It is shown that the magnetostatic results are considerably modified (especially in Ni) by the exchange. Numerical examples for the cases of weak, intermediate and strong pinning were shown. The effects on the mode hybridization were discussed. Numerical calculations have also been carried for larger damping by taking $\alpha_0 = 0.02$. This typically produces smaller changes than those due to varying the pinning conditions, but the frequency shifts may still be appreciable. The previous BLS measurements emphasized the size dependence (in the case of Ni wires [69]) and the field dependence (in the case of Ni tubes [60]). The macroscopic theory is broadly consistent with these findings, as already noted in both of the cited papers (and see also our Fig. 5.6), but a more complete comparison with our theory would be possible if future BLS experiments studied the effect of varying the longitudinal wave number q by varying the scattering geometry.

We note that the effects of core removal as identified here in long tubes is

quite distinct from the effect in flat disks [119], where there is vortex formation as a consequence of the different (mainly in-plane) magnetization orientation. Following an earlier work on an elliptical cylinder [28], magnetostatic mode calculations in tubes with an elliptical (rather than circular) cross section have recently been reported [120], and it would be of interest to generalize these to include explicitly the exchange effects, and the consequent mode mixing, by following the approach used here.

CHAPTER 6

Green's Function Theory of Magnetostatic Modes in Magnetic Nanotubes

6.1 Introduction

Green's functions provide the basis of a powerful and popular method in theoretical physics for obtaining full information about the excitations of many-body systems, e.g., they contain information about the intensity (or spectral weight) of the excitations, as well as their frequencies. Green's functions can also be related to scattering cross-sections, as measured (e.g.) in light scattering, so there is a convenient connection to experimental techniques. Green's functions can be defined in various ways, but basically they are a measure of the dynamic correlation functions between two quantities, such as two magnetization variables. The methods for calculating Green's functions include equation-of-motion methods, diagrammatic perturbation theory, and linear response theory. Some general references for Green's functions methods are [121, 122, 123, 124, 125].

Green's functions have been used extensively for finite magnetic materials (both F and AF), mainly in planar geometries. For example, in a finite thickness F slab, the linear response Green's functions in the magnetostatic regime were calculated and applied to BLS in [90]. Green's function formalisms were also applied to Heisenberg F films where the exchange effects dominate in the SW excitations [126], to semi-infinite F systems with both dipole and exchange interactions [89], and to semi-infinite AF systems for magnetic polaritons [103]. These examples of earlier research motivate us to develop a Green's function theory for the magnetostatic modes in cylindrical nanotubes in order to extend the results for the magnetostatic SW dispersion relations presented in Chapter 2.

We will use the linear response formalism (see, e.g., [121]) for Green's functions. This will enable us to investigate the spectral intensities of the surface and bulk magnetostatic SW in the different cylindrical geometries (tubes, wires, and antiwires), assumed to have a large length-to-diameter aspect ratio as previously. Our calculations, which are carried out for F and AF materials, apply when both the applied magnetic field and the saturation magnetization are parallel to the cylinder axis. Specifically, the response functions are derived for situations where the dipole-dipole interactions are dominant over the exchange in the spin dynamics, but the results could be extended to other regimes of magnetic behaviour.

The outline of this chapter is as follows. In Sec. 6.2 we develop the Green's function theory for SW in F and AF nanotubes. Basically, we supplement the formalism in Chapter 2 by adding an external driving field to the Landau-Lifshitz equation in the absence of damping, and we calculate the linear response in the r.f. magnetization components. We again use the magnetostatic form of Maxwell's equations together with the usual boundary conditions, but now we obtain a second order inhomogeneous differential equation from which the magnetic Green's functions are deduced. Using a result known as the fluctuation-dissipation theorem, we derive an expression for the spectral intensities of the SW. Afterwards, some specific numerical applications are given in Sec. 6.3 for F (e.g., Ni) and AF (e.g., $GdAlO_3$) materials, supplementing the magnetostatic mode results of Chapter 2. Then in Sec. 6.4 we conclude our work with an outline of possible extensions.

6.2 Response functions for magnetostatic modes in nanotubes

Following the model for magnetic nanotubes used in Chapter 2, we now extend our theory of the magnetostatic modes by calculating the magnetic Green's functions (or response functions) in F and AF cylindrical tubes. With a longitudinal

applied field H_0 and the saturation magnetization M_0 along the symmetry axis of the tube, we derive the response functions for situations where the long range dipole-dipole effects dominate in the SW dynamics over the exchange effects. By analogy with earlier chapters, the magnetic response function for nanotubes will provide results for the single interface cases of antiwires and wires as limiting cases.

In the long wavelength SW dynamics (ignoring exchange and damping), the semi-classical torque equation of motion for the magnetization $\vec{M}$ can be expressed, putting $\alpha_0 = D = 0$ in Eq. (1.9), as

$$\frac{d\vec{M}}{dt} = -\gamma\mu_0(\vec{M} \times \vec{H}_{eff}),\qquad(6.1)$$

where the total magnetization is $\vec{M} = M_0\hat{z} + \vec{m}(\vec{r})e^{-i\omega t}$ with $|\vec{m}| << M_0$ in the linear SW regime, as before. However, in the presence of a time dependent external driving field $\vec{H}_{ext}(\vec{r},t) = \vec{H}_{ext}(\vec{r})e^{-i\omega t}$, Eq. (5.1) becomes (see, e.g., [90])

$$\vec{H}_{eff} = H_0\hat{z} + \{\vec{h}_d(\vec{r}) + \vec{H}_{ext}(\vec{r})\}e^{-i\omega t}.\qquad(6.2)$$

Here ω is the angular frequency of the driving field (and of the SW excitations). Our goal is to investigate the linear response between the r.f. magnetization components and the external driving field in the magnetic tubes in order to evaluate the response functions. In contrast with [90], where the response functions for a F slab were deduced by choosing the driving field in a plane wave representation, the radial dependence in a cylindrical geometry is more complicated. It is now more convenient to choose the driving field in our calculations in the form

$$\vec{H}_{ext}(\vec{r}) = \vec{H}_{ext}\delta(r - r')e^{i(n\theta+qz)},\qquad(6.3)$$

where n is an integer and q is the wave number of magnetostatic modes along

the symmetry axis, as in Chapter 2. By analogy with other calculations where a delta-function representation of the driving term was chosen (e.g., for the DESW in a semi-infinite F material [89] and for surface phonons [16]), we will eventually deduce the magnetic linear response at position $\vec{r}$ due to a driving field at $\vec{r}'$.

Next, we linearize Eq. (6.1) after substituting for $\overrightarrow{M}$ and $\overrightarrow{H}_{eff}$, which gives

$$-i\omega\overrightarrow{m}(\overrightarrow{r}) = -\omega_m\{\hat{z} \times (\overrightarrow{h}_d(\overrightarrow{r}) + \overrightarrow{H}_{ext}(\overrightarrow{r}))\} + \omega_0\{\hat{z} \times \overrightarrow{m}(\overrightarrow{r})\}. \tag{6.4}$$

By analogy with Chapter 2, we use the magnetostatic form of Maxwell's equations to re-express the dipolar part $\overrightarrow{h}_d$ of the fluctuating field in terms of the magnetostatic scalar potential Ψ with the form given in Eq. (2.3). After some algebra, we obtain an *inhomogeneous* differential equation for the radial part $\psi(r)$ of the scalar potential inside the magnetic layer of cylindrical tubes and the result is

$$\frac{d^2\psi(r)}{dr^2} + \frac{1}{r}\frac{d\psi(r)}{dr} - \left(\frac{n^2}{r^2} + k^2\right)\psi(r) =$$
$$\nu(\omega)\left[A\left\{\frac{\delta(r - r')}{r} + \frac{d\delta(r - r')}{dr}\right\} + \frac{nB\delta(r - r')}{r}\right], \tag{6.5}$$

where $k = \sqrt{\nu(\omega)}q$, $A = \chi_a H_{ext}{}^r + i\chi_b H_{ext}{}^\theta$ and $B = \chi_b H_{ext}{}^r + i\chi_a H_{ext}{}^\theta$. The forms of χ_a and χ_b can be expressed as in Chapter 2 for a F or AF material.

To solve Eq. (6.5) we need to examine the behaviour in the region of $r = r'$. Integrating Eq. (6.5) from $r = r' - \varepsilon$ to $r = r' + \varepsilon$ and taking the limit of $\varepsilon \to 0$, it is found that the first derivative of ψ is discontinuous at $r = r'$, but ψ is continuous. This gives two boundary conditions at $r = r'$, which are

$$\left.\frac{d\psi(r)}{dr}\right|_{r=r'+\varepsilon} - \left.\frac{d\psi(r)}{dr}\right|_{r=r'-\varepsilon} = -\frac{\nu(\omega)(A - nB)}{r'}, \tag{6.6}$$

$$\left.\psi(r)\right|_{r=r'+\varepsilon} - \left.\psi(r)\right|_{r=r'-\varepsilon} = 0. \tag{6.7}$$

It is now straightforward to find the solutions of Eq. (6.5). The homogeneous part of this equation turns into the form of the Walker equation in Eq. (2.4), and therefore the solution inside the magnetic layer has the form

$$
\psi(r) \;=\; \begin{cases} p_1 I_n(kr) + p_2 K_n(kr) \;\; ; \quad r < r^{'} \\[2mm] p_3 I_n(kr) + p_4 K_n(kr) \;\; ; \quad r > r^{'}, \end{cases}
\tag{6.8}
$$

with unknown coefficients p_1, p_2, p_3 and p_4. As in Chapter 2, $\psi(r)$ for the nonmagnetic regions $r < R_1$ and $r > R_2$ has the same form as in Eqs. (2.7) and (2.8), where two more coefficients a_1 and a_3 are involved with Bessel functions I_n and K_n.

To find these six unknown coefficients a_1, p_1, p_2, p_3, p_4 and a_3, the magnetostatic form of the boundary conditions (see Chapter 2) are applied at the $r = R_1$ and $r = R_2$ interfaces of the tube. These four conditions, plus the two additional conditions in Eq. (6.6), give a set of equations which can be used to solve for the six coefficients. After some extensive algebra, the magnetic scalar potential for $r < r^{'}$ inside the magnetic layer of the tube can be expressed as

$$
\psi(r) \;=\; \frac{\Lambda(A - nB)}{T_1 T_3}\left[\left\{T_2 T_3 \frac{K_n(kR_2)}{I_n(kR_2)} I_n(kr) I_n(kr^{'}) + \right.\right.
$$
$$
\left.\left. T_1 T_4 \frac{I_n(kR_1)}{K_n(kR_1)} K_n(kr) K_n(kr^{'})\right\} - T_1 T_3 I_n(kr) K_n(kr^{'})\right],
\tag{6.9}
$$

and the form of scalar potential inside the tube for $r > r^{'}$ is

$$
\psi(r) \;=\; \frac{\Lambda(A - nB)}{T_1 T_3}\left[\left\{T_2 T_3 \frac{K_n(kR_2)}{I_n(kR_2)} I_n(kr) I_n(kr^{'}) + \right.\right.
$$
$$
\left.\left. T_1 T_4 \frac{I_n(kR_1)}{K_n(kR_1)} K_n(kr) K_n(kr^{'})\right\} - T_1 T_3 K_n(kr) I_n(kr^{'})\right].
\tag{6.10}
$$

Here we have introduced the following definitions:

$$\Lambda = \frac{\nu(\omega)}{kr' I_n(kr') K_n(kr')} \left\{ \frac{K_n'(kr')}{K_n(kr')} - \frac{I_n'(kr')}{I_n(kr')} \right\}^{-1},$$

$$T_1 = \{\nu(\omega)\}^{-1} kR_2 \frac{I_n'(kR_2)}{I_n(kR_2)} - qR_2 \frac{K_n'(qR_2)}{K_n(qR_2)} - n\chi_b,$$

$$T_2 = \{\nu(\omega)\}^{-1} kR_2 \frac{K_n'(kR_2)}{K_n(kR_2)} - qR_2 \frac{K_n'(qR_2)}{K_n(qR_2)} - n\chi_b,$$

$$T_3 = \{\nu(\omega)\}^{-1} kR_1 \frac{K_n'(kR_1)}{K_n(kR_1)} - qR_1 \frac{I_n'(qR_1)}{I_n(qR_1)} - n\chi_b,$$

$$T_4 = \{\nu(\omega)\}^{-1} kR_1 \frac{I_n'(kR_1)}{I_n(kR_1)} - qR_1 \frac{I_n'(qR_1)}{I_n(qR_1)} - n\chi_b \quad . \tag{6.11}$$

Next, we substitute for the dipolar field terms in Eq. (6.4) by using the solutions for ψ in Eqs. (6.9) and (6.10). These calculations establish a linear relationship between components of $\overrightarrow{m}$ and $\overrightarrow{H}_{ext}$. For example, the m^r component of magnetization can be derived for $r < r'$ as

$$m^r(r < r') = \{(\chi_a - n\chi_b)\Theta_1\}H_{ext}{}^r + i\{(\chi_b - n\chi_a)\Theta_1\}H_{ext}{}^\theta, \tag{6.12}$$

with

$$\Theta_1 = \frac{\Lambda}{rT_1T_3}\left[T_3 I_n(kr)\left\{ \chi_a kr \frac{I_n'(kr)}{I_n(kr)} - n\chi_b \right\}\left\{ T_2 \frac{K_n(kR_2)}{I_n(kR_2)} I_n(kr') - T_1 K_n(kr') \right\} \right.$$
$$\left. + T_1 T_4 K_n(kr') K_n(kr) \frac{I_n(kR_1)}{K_n(kR_1)}\left\{ \chi_a kr \frac{K_n'(kr)}{K_n(kr)} - n\chi_b \right\} \right], \tag{6.13}$$

whereas for $r > r'$ it is

$$m^r(r > r') = \{(\chi_a - n\chi_b)\Theta_2\}H_{ext}{}^r + i\{(\chi_b - n\chi_a)\Theta_2\}H_{ext}{}^\theta, \tag{6.14}$$

with

$$
\begin{aligned}
\Theta_2 &= \frac{\Lambda}{rT_1T_3}\left[T_1K_n(kr)\left\{\chi_a kr\frac{K_n^{'}(kr)}{K_n(kr)} - n\chi_b\right\}\left\{T_4\frac{I_n(kR_1)}{K_n(kR_1)}K_n(kr^{'}) - T_3I_n(kr^{'})\right\}\right. \\
&\quad \left. + T_2T_3I_n(kr^{'})I_n(kr)\frac{K_n(kR_2)}{I_n(kR_2)}\left\{\chi_a kr\frac{I_n^{'}(kr)}{I_n(kr)} - n\chi_b\right\}\right]. \tag{6.15}
\end{aligned}
$$

Eqs. (6.12) and (6.14) give the linear response between the magnetization component $m^r(r)$ and the driving-field components $H_{ext}{}^r$ and $H_{ext}{}^\theta$, which couple to $m^r(r^{'})$ and $m^\theta(r^{'})$ respectively. The position-dependent magnetic response functions can then be written down (see [121]). In the standard Green's function notation we obtain for $r < r^{'}$

$$
\begin{aligned}
\langle\langle m^r(r); m^r(r^{'})\rangle\rangle &= (\chi_a - n\chi_b)\Theta_1, \\
\langle\langle m^r(r); m^\theta(r^{'})\rangle\rangle &= i(\chi_b - n\chi_a)\Theta_1. \tag{6.16}
\end{aligned}
$$

while for $r > r^{'}$

$$
\begin{aligned}
\langle\langle m^r(r); m^r(r^{'})\rangle\rangle &= (\chi_a - n\chi_b)\Theta_2, \\
\langle\langle m^r(r); m^\theta(r^{'})\rangle\rangle &= i(\chi_b - n\chi_a)\Theta_2. \tag{6.17}
\end{aligned}
$$

In a similar fashion, we could solve for linear response of $m^\theta(r)$ in order to derive other magnetic Green's functions like $\langle\langle m^\theta(r); m^r(r^{'})\rangle\rangle$ and $\langle\langle m^\theta(r); m^\theta(r^{'})\rangle\rangle$. From Eqs. (6.16) and (6.17) and the form of Θ_1 and Θ_2, it is apparent that the Green's functions have denominators that contain the previous analytical dispersion relations of surface magnetostatic modes in magnetic nanotubes (see Chapter 2). This is expected from the general property that the poles of Green's functions yield the excitation frequencies.

Briefly, we discuss the two special cases of an antiwire (taking $R_1 = R$, $R_2 \rightarrow \infty$) and a wire (taking $R_1 \rightarrow 0$, $R_2 = R$) for the magnetic Green's functions. As

before, we form an appropriate solution for $\psi(r)$ in terms of Bessel functions and follow a similar procedure as for tubes. The magnetic Green's functions can still be expressed in the form of Eqs. (6.16) and (6.17), but the expressions for Θ_1 and Θ_2 are modified to become

$$
\begin{aligned}
\Theta_1 &= \frac{\Lambda}{rT_3} K_n(kr') \left[T_4 K_n(kr) \frac{I_n(kR)}{K_n(kR)} \{ \chi_a kr \frac{K_n'(kr)}{K_n(kr)} - n\chi_b \} \right. \\
&\quad \left. - T_3 I_n(kr) \left\{ \chi_a kr \frac{I_n'(kr)}{I_n(kr)} - n\chi_b \right\} \right],
\end{aligned}
\tag{6.18}
$$

$$
\Theta_2 = \frac{\Lambda}{rT_3} K_n(kr) \left\{ \chi_a kr \frac{K_n'(kr)}{K_n(kr)} - n\chi_b \right\} \left\{ T_4 \frac{I_n(kR)}{K_n(kR)} K_n(kr') - T_3 I_n(kr') \right\},
\tag{6.19}
$$

for the antiwire geometry, and

$$
\Theta_1 = \frac{\Lambda}{rT_1} I_n(kr) \left\{ \chi_a kr \frac{I_n'(kr)}{I_n(kr)} - n\chi_b \right\} \left\{ T_2 I_n(kr') \frac{K_n(kR)}{I_n(kR)} - T_1 K_n(kr') \right\},
$$

$$
\begin{aligned}
\Theta_2 &= \frac{\Lambda}{rT_1} I_n(kr') \left[T_2 \frac{K_n(kR)}{I_n(kR)} I_n(kr) \left\{ \chi_a kr \frac{I_n'(kr)}{I_n(kr)} - n\chi_b \right\} - \right. \\
&\quad \left. T_1 K_n(kr) \left\{ \chi_a kr \frac{K_n'(kr)}{K_n(kr)} - n\chi_b \right\} \right],
\end{aligned}
\tag{6.20}
$$

for the wire geometry.

Finally, as a further application of the Green's functions, we may employ the fluctuation-dissipation theorem (see [34, 121, 124]) to calculate the spectral intensities. This powerful result allows us to express the correlation function $\langle m^\alpha(r) m^\beta(r') \rangle$ in terms of its corresponding Green's function:

$$
\langle m^\alpha(r) m^\beta(r') \rangle_\omega = -2[1 + n(\omega)] \mathrm{Im} \langle\langle m^\alpha(r); m^\beta(r') \rangle\rangle_{\omega + i\epsilon},
\tag{6.21}
$$

where ϵ denotes a positive infinitesimal. The superscripts α and β correspond here to r and θ components, and $n(\omega) = [\exp(\hbar\omega/k_B T) - 1]^{-1}$ is the Bose-Einstein distribution function. If we put $r' \to r$ in Eq. (6.21) and choose (for example) $\alpha = \beta = r$, we obtain an expression for the quantity $\langle|m^r(r)|^2\rangle_\omega$ which is a measure of the mode intensity at radius r and frequency ω.

Based on our analytical expressions for the magnetic response functions, numerical examples for the spectral intensities of surface and bulk magnetostatic modes in F nanotubes, with the single interface limits, will be presented in the next section. Numerical applications will also be made for AF nanotubes.

6.3   Numerical applications

We now present some numerical results for the spectral intensities taking Ni and GdAlO$_3$ for the magnetic materials, as used in Chapters 2 and 3 for studies of the surface and bulk magnetostatic dispersion relations. In each case, we will present the frequency dispersion relations in order to illustrate the surface and bulk SW modes, and then describe the dependence of the integrated intensities on frequency, wave number q, and size. Some results will be included as well for the spatial distribution of the mode intensities. In all examples, a small value of the half-width of the spectral intensity peaks, i.e., $\epsilon = 0.02$ GHz, is arbitrarily chosen.

We first show the results for a single interface case of a Ni antiwire with radius $R = 500$ nm in an applied field $\mu_0 H_0 = 0.3$ T. The imaginary part of $\langle\langle m^r(r); m^r(r')\rangle\rangle$ from Eqs. (6.16) and (6.17) can be used to calculate the spectral intensity $\langle|m^r(r)|^2\rangle_\omega$ for the surface modes as explained earlier. The dispersion relations are presented in Fig. 6.1(a) for the lowest four $|n|$ surface modes and then in Fig. 6.1(b) we plot the corresponding integrated intensities in arbitrary units as a function of frequency, taking $q = 1.0 \times 10^6$ m^{-1}. It is seen that the intensities for this q tend to increase with increasing $|n|$ for the antiwires.
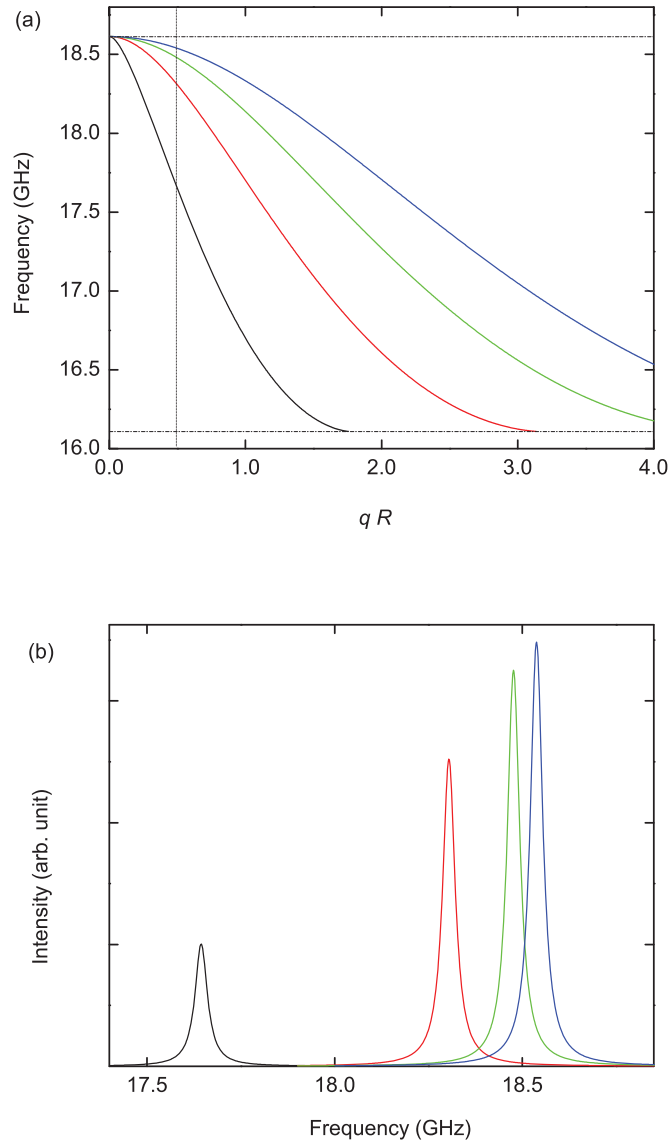
Figure 6.1: (a) Frequencies of surface magnetostatic modes in a Ni antiwire versus qR, taking $\mu_0 H_0 = 0.3$ T. The lower and the upper limits of the surface-mode regions are shown as horizontal lines. The four lowest modes for $|n| = 1$ (black), 2 (red), 3 (green) and 4 (blue) are plotted. (b) Spectral intensities of these four modes versus frequency for the same antiwire taking $qR = 0.5$, as marked by a vertical dashed line in (a).
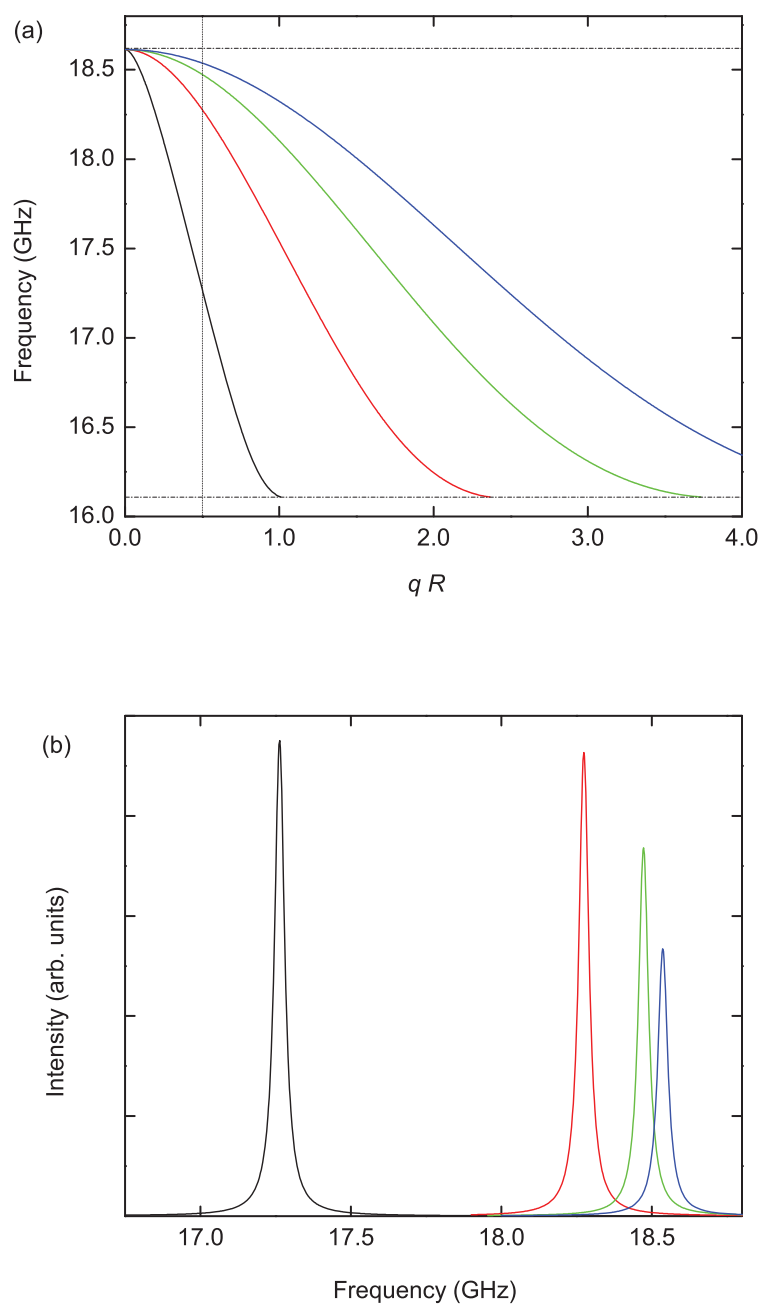
Figure 6.2: Same as in Fig. 6.1, but for a Ni nanowire of the same radius.

For comparison, in Fig. 6.2 we present analogous calculations for the frequencies and spectral intensities, taking a Ni nanowire of the same radius $R = 500$ nm. In contrast to the results in Fig. 6.1(b) for an antiwire, it turns out that the relative heights of the Lorentzian-like peaks for individual mode intensities in a Ni wire decreases when $|n|$ increases (see Fig. 6.2(b)).

Next, we compute the spectral intensities of the surface magnetostatic modes for a Ni nanotube of inner radius $R_1 = 150$ nm and outer radius $R_2 = 500$ nm. Following our previous examples, the frequencies of surface SWs versus wave number for the three lowest $|n|$ modes are plotted in Fig. 6.3(a). With the choice of $q = 1.2 \times 10^6$ m^{-1}, which is less than the mode cut-off value, our results for the spectral intensity of the individual modes as a function of frequency are presented in Fig. 6.3(b). For each value of $|n|$ there are in general two modes, and each of these gives a peak in the spectral intensity that depends on the mode localization. Broadly, the lower-frequency and upper-frequency branches are localized near the outer and inner radii of the tube respectively. At any intermediate radial distance r, chosen as 300 nm in Fig. 6.3(b), there are contributions from both branches, but the ratio of intensities will vary as r ranges between R_1 and R_2. For more information on the localization of individual surface SW modes, we illustrate in Fig. 6.4 the variation of the spectral intensities with r throughout the wall thickness. The ratio r/R_2 for the Ni nanotube varies from 0.3 to 1, keeping other parameters are same as in 6.3(a). It is evident that the lower- and upper- frequency branches are typically localized near the R_2 and R_1 interfaces, respectively.

The preceeding analysis of spectral intensities for surface magnetostatic SWs can straightforwardly be extended to study the spectral intensities of the bulk modes. As an example, we show in Fig. 6.5 the spectral intensity versus r/R_2, taking other parameters as in Fig. 6.4 for a Ni nanotube, but using $q = 1.5 \times 10^7$ m^{-1}. It is found that the standing SWs propagate within the wall thickness of the tube with
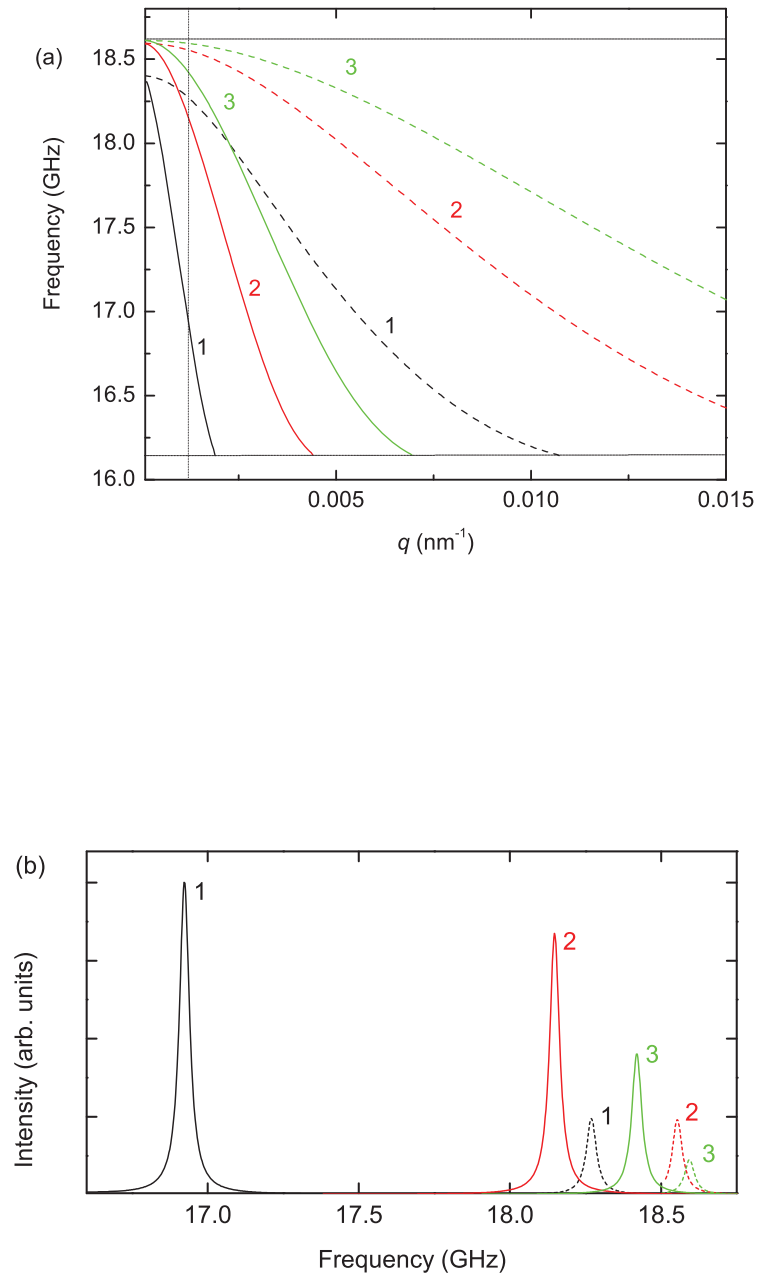
Figure 6.3: (a) Frequencies of surface modes in a Ni nanotube versus q, taking $\mu_0 H_0$ = 0.3 T, $R_1 = 150$ nm and $R_2 = 500$ nm. The lower and the upper limits of the surface-mode regions are shown as horizontal lines. (b) Spectral intensity plotted versus frequency in the same nanotube for $q = 1.2 \times 10^6$ m^{-1}. The solid and dash lines refer to the lower- and upper-frequency branches respectively for $|n| = 1$ (black), 2 (red) and 3 (green).
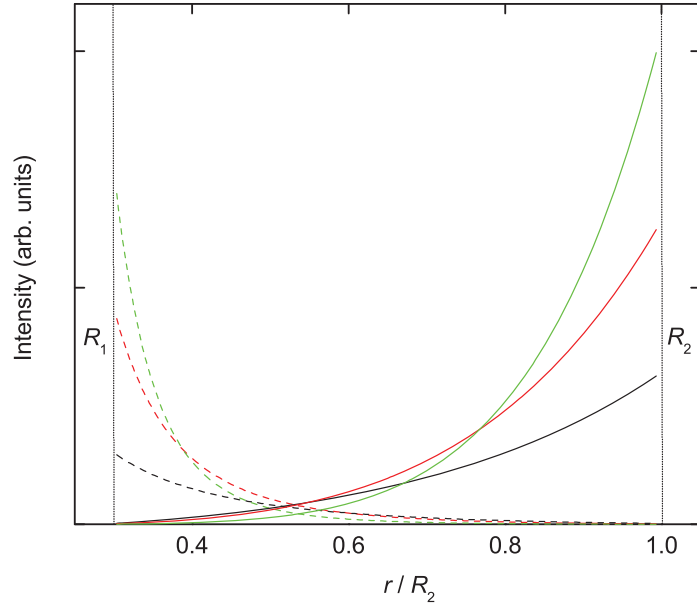
Figure 6.4: Intensities of the lowest surface modes in a Ni nanotube plotted against r/R_2. The solid and dashed lines refer to the lower and upper frequency branches respectively for $|n| = 1$, 2 and 3. The interfaces at $R_1 = 150$ nm and $R_2 = 500$ nm correspond to the vertical lines.

zero, one and two nodes, depending on $|n|$. In contrast to the surface modes where spectral intensities are localized near surface (see Fig. 6.4), the intensities of bulk modes show an oscillatory behaviour between two interfaces of tubes.

A similar analysis of spectral intensities can be made for surface and bulk magnetostatic modes in AF nanotubes. For example, we have made calculations for a GdAlO$_3$ nanotube with $R_1 = 200$ nm and $R_2 = 500$ nm. Taking $q = 8.0 \times 10^5$ m^{-1}, $\mu_0 H_0 = 0.7$ T and other material parameters as in Sec. 3.3, we present some results in Table 6.1 for a study of the spectral intensities with the frequencies of surface modes for the intermediate radial distances $r = 250$ nm and 310 nm.
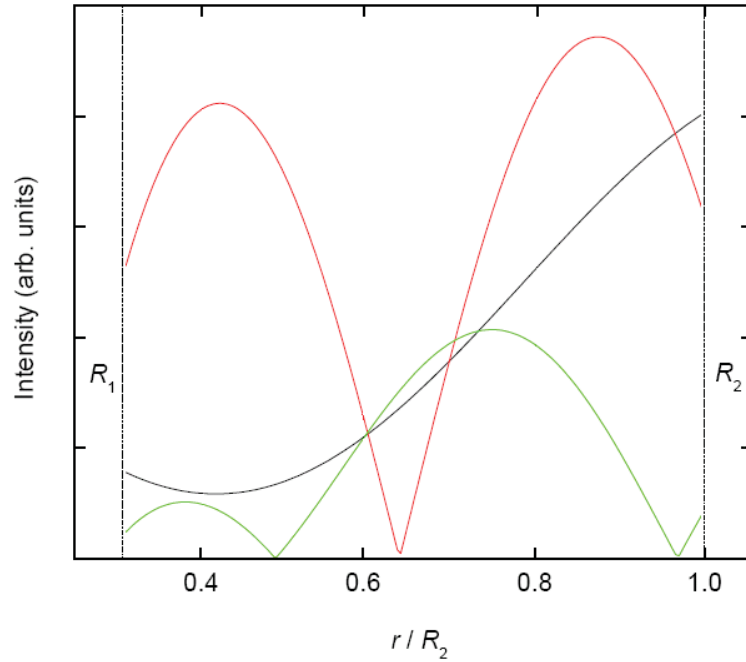
Figure 6.5: The same as in Fig. 6.4, but for each of the lowest bulk modes of $|n| = 0$ (black), 1 (red) and 2 (green), taking $q = 1.5 \times 10^7$ m^{-1}.

Table 6.1: Integrated intensities and frequencies of three different surface modes in an AF nanotube of GdAlO$_3$. Parameter values are $q = 8.0 \times 10^5$ m^{-1}, $\mu_0 H_0 = 0.7$ T, $R_1 = 200$ nm, and $R_2 = 500$ nm.

$|n|$	Frequency (GHz)	Relative Intensity (arb. units)	
		r = 310 nm	r = 250 nm
	17.54	0.57	0.22
1	17.78	0.15	0.31
	17.80	0.50	0.15
2	17.86	0.23	0.86
	17.85	0.30	0.06
3	17.87	0.26	1

6.4 Conclusions

Using linear response methods we have developed a theory of Green's functions for studying the properties of the magnetostatic modes in cylindrical tubes, together with the limiting geometries of wires and antiwires. This involved adding an external driving field to the LL torque equation for the magnetization, together with the magnetostatic form of Maxwell's equations and the usual boundary conditions at the interfaces. After solving an inhomogeneous differential equation, the position-dependent magnetic Green's functions were obtained in terms of the linear response between the position dependent magnetization components and the position dependent external driving field components. It can be noted that each of the expressions for the magnetic Green's functions contained the analytical dispersion relations (as derived in Chapter 2) in the denominator. In addition, the Green's functions also provide results for the spectral intensity of the magnetostatic SW. Based on our analytical calculations for the response functions, numerical applications were made to F (using Ni) and AF (using $GdAlO_3$) magnetic structures. Our calculations in these cylindrical geometries have clearly illustrated the structural effects on the strength of intensity peaks. Consistent with our previous results in Chapter 2, we also noticed that the spectral intensities of surface modes are localized near inner and outer interface of tubes, whereas the intensities of bulk modes behave in an oscillatory fashion within the tube.

There are several possible extensions to this chapter. By analogy with earlier work on planar geometries such as superlattices [34], it would be of great interest to generalize our present Green's function formalism for the magnetostatic modes in tubes to the case of cylindrical magnetic multilayers. This could be achieved by using linear response theory together with our transfer matrix analysis discussed in Chapter 2. The formalism could also be extended to the SW polariton modes in tubes (generalizing results in Chapter 4). Similarly, Green's function calculations

could be carried out for the dipole-exchange regime (generalizing results in Chapter 5). In all of these magnetic regimes, it would be possible to use the Green's functions to deduce expressions for the scattering cross-section for BLS in a cylindrical geometry, as was done for planar geometries (see, e.g., [34]).

CHAPTER 7
Conclusions

We have presented in this thesis new theoretical calculations of magnetic excitations in F and AF cylindrical geometries. A macroscopic continuum approach has been used to study the dynamical properties of the SW excitations in different wavevector regimes taking account of the long range dipole-dipole and short range exchange interactions together with or without retardation effects according to the region of interest. By contrast with other theoretical methods (e.g., [102, 127]) that used approximations based on the Holstein-Primakoff transformation to boson operators, our calculations are developed with the linearized form of the semi-classical torque equation, Maxwell's equations and appropriate electromagnetic boundary conditions to describe the propagation of the SW modes. Our approach is convenient and has the flexibility to allow us to cover the different wavevector regimes in the chosen geometries.

In Chapter 2 we illustrated results for the nonretarded dipolar SW modes in cylindrical nanotubes. As we have seen, the dynamical properties of magnetostatic modes, e.g., the mode localizations, the radial distribution of mode amplitudes, etc. in tubes show different behaviour from the results in wires or antiwires. Previously only results for wires were available. The transfer matrix method outlined in that chapter enabled us to generalize these results to cylindrical multilayer systems. We have illustrated in the dispersion curves that the localized interface modes are strongly modified (e.g., in their frequency and wave number cut-off) by the multilayer structure, compared to the behaviour found in earlier cases. Results for the coupled dipolar modes in F-AF cylindrical bilayer systems have presented in Chapter 3, where we have illustrated the influence of exchange anisotropy on magnetostatic

modes. These calculations provide useful information for experimental studies by BLS, e.g., with 90^0 scattering geometry to achieve the small q (typically less than 10^7 m^{-1}) for the magnetostatic regime.

In Chapter 4 we developed a theory for the localized surface and bulk magnetic polaritons in cylindrical tubes. The dispersion relation was solved numerically, which allowed us to account for the magnetic polariton spectra in F and AF tubes, including the limiting wires and antiwires. By contrast with some previous calculations for AF wires in nonzero fields [83] where a decoupling approximation was used, our formalism correctly reduces to the known magnetostatic limit if the retardation effects become small (i.e., as the diameter shrinks). Also, in the presence of retardation, our formalism is consistent with that in [107] derived for the special case of a F wire. The magnetic polariton modes in these cylindrical geometries could be investigated experimentally by the ATR technique.

In Chapter 5 we presented a general theory for the dipole-exchange SW in nanotubes together with its limiting geometries. The dispersion relations were derived by including both dipole-dipole and exchange effects. Overall, our results are broadly consistent with the BLS data in [60, 69] and provide information about the pinning. However, a more complete comparison would be possible if further BLS experiments with the variation of longitudinal wave number is used for probing SW in these cylindrical nanostructures.

In Chapter 6 the magnetic response functions (Green's functions) were evaluated in the magnetostatic regime for different F and AF cylindrical geometries and employed to investigate the spectral intensities of the modes. In accordance with the mode localization, the spectral intensity peaks for each $|n| > 0$ were deduced, showing the existence of two surface modes for each $|n|$ in the dispersion relations provided q does not exceed a cut-off value. The spatial distribution of surface modes for each $|n|$ were investigated, showing that the lower- and upper-frequency branches

are typically localized near the tubes inner and outer radii, respectively. These intensity calculations are useful for applications to BLS and can be extended to other wavevector regimes.

New developments in magnetic metamaterials, or man-made artificial materials, have been attracting much attention due to their wide range of potential applications starting from radio frequencies to near optical frequencies [128]. The recent fabrications of magnetic metamaterials and the unprecedented growth in related technology [129, 130, 131] provide motivation to extend our magnetic polariton calculations for exploring fundamental properties and functionality that would be unattainable in naturally occurring materials, particularly as regards optics and nanotechnology. Such a calculation could proceed by assuming an isotropic medium of dielectric permittivity $\overleftrightarrow{\epsilon}(\omega)$ and magnetic permeability $\overleftrightarrow{\mu}(\omega)$ having the form expressed in [132] and in Chapter 4, respectively, governing the electromagnetic properties of these materials where a negative refractive index is claimed to be feasible. This would change the usual light properties, i.e., the light would be refracted on the same side of the normal incidence, reversing the Doppler shift, etc. By allowing the coupling of the $\vec{E}$- and $\vec{B}$-field components of light in cylindrical geometries, interesting features of the negative refraction anomalies on magnetic polaritons could be investigated in magnetic metamaterial multilayered cylindrical systems.

It would also be of interest to extend our linear SW calculations to the nonlinear regimes. In 1952 Bloembergen *et al* [133] first observed the nonlinearity effect in a high-power FMR experiment. The properties of nonlinear SW dynamics in microwave-driven planar multilayer systems were investigated in [134]. The LL equation was used to show that a high-power microwave driving field parallel to the applied d.c. field can cause nonlinear effects. The study of nonlinear properties in terms of magnetostatic dispersion relations and their relation to bistable and

multistable microwave transmission in F thin film was described in [135]. Recently, the nonlinear effects in terms of second harmonic generation of AF multilayers in the Voigt geometry were investigated [136]. Reviews for a magnetic thin film are given in [16]. To proceed with the macroscopic continuum theory, the power series expansion for magnetic susceptibility could be written as

$$m_\alpha = \chi_{\alpha\beta} h_\beta + \chi_{\alpha\beta\gamma} h_\beta h_\gamma + \chi_{\alpha\beta\gamma\delta} h_\beta h_\gamma h_\delta, \tag{7.1}$$

where $\chi_{\alpha\beta}$ is the linear susceptibility tensor components, which was discussed in Chapter 1, while the new terms $\chi_{\alpha\beta\gamma}$ and $\chi_{\alpha\beta\gamma\delta}$ are the second- and third-order nonlinear susceptibilities, respectively. Following an established procedure [137] for a uniaxial AF material, it would be possible to derive these higher order susceptibility components from the LLG equation for a magnetic material, then to proceed using Maxwell's equations and the electromagnetic boundary conditions. These calculations can be done independently for second- and third-order interactions to illustrate the properties of nonlinear SW dynamics in cylindrical multilayered structures for different wavevector regimes.

References

[1] D. L. Mills and J. A. C. Bland (eds.), *Nanomagnetism: Ultrathin Films, Multilayers and Nanostructures* (Amsterdam: Elsevier, 2006).

[2] D. S. Parasnis, *Magnetism*(Hutchinson & Co., London 1961).

[3] R. C. O'Handley, *Modern Magnetic Materials*(John Wiley and Sons, New York, 2000).

[4] J. A. C. Bland and B. Heinrich (eds.), *Ultrathin Magnetic Structures III* (Springer, Berlin, 2005).

[5] B. Behin-Aein, D. Datta, S. Salahuddin and S. Datta, Nature Nanotechnology **5**, 266 (2010).

[6] D. Weller and A. Moser, Magn. IEEE Trans. **35**, 4423 (1999).

[7] W. H. Meiklejohn and C. P. Bean, Phys. Rev. **102**, 1413 (1956).

[8] J. Eisenmenger and I. K. Schuller, Nature Materials **2**, 437 (2003).

[9] R. E. Camley, Surf. Sci. Rep. **7**, 103 (1987).

[10] S. Neusser and D. Grundler, Adv. Mater. **21**, 2927 (2009).

[11] S. Linden, M. Decker, and M. Wegener, Phys. Rev. Lett. **97**, 083902 (2006).

[12] J. P. Jakubovics, *Magnetism and Magnetic Materials*(The Institute of Materials, London, 1994).

[13] N. A. Spaldin *Magnetic Materials*(Cambridge University Press, Cambridge, 2003).

[14] J. D. Jackson, *Classical Electrodynamics, 3rd edn.* (Wiley, New York 1999).

[15] M. G. Cottam (ed.), *Linear and Nonlinear Spin Waves in Magnetic Films and Superlattices* (World Scientific, Singapore, 1994).

[16] M. G. Cottam and D. R. Tilley *Introduction to Surface and Superlattice Excitations, 2nd edn.* (Institute of Physics, Bristol, 2005).

[17] A. P. Guimarães and I. S. Oliveira, *Magnetism and Magnetic Resonance in Solids* (John Wiley and Sons, New York, 1998).

[18] R. Skomski and J. M. D. Coey, *Permanent Magnetism* (Institute of Physics Publishing, Bristol, 1999).

[19] J. Nogués, J. Sort, V. Langlais, V. Skumryev, S. Suriñach, J. S. Muñoz and M. D. Baró, Phys. Rep. **422**, 65 (2005).

[20] D. L. Mills, *Surface Excitations*, ed. by V. M. Agranovich and R. Loudon, (North-Holland, Amsterdam, 1984).

[21] R. E. Camley, J. Magn. Magn. Mater. **200**, 583 (1999).

[22] L. R. Walker, Phys. Rev. **105**, 390 (1957).

[23] R. L. Stamps and R. E. Camley, J. Appl. Phys. **56**, 3497 (1984).

[24] E. F. Sarmento and D. R. Tilley, J. Phys. C **10**, 795 (1977).

[25] C. Kittel, Phys. Rev. **110**, 1295 (1958).

[26] M. H. Seavey and P. E. Tannenwald, Phys. Rev. Lett. **1**, 168 (1958).

[27] R. W. Damon and J. R. Eshbach, J. Phys. Chem. Solids **19**, 308 (1961).

[28] R. E. DeWames and T. Wolfram, Appl. Phys. Lett. **16**, 305 (1970).

[29] A. Hartstein, E. Burstein, A. A. Maradudin, R. Brewer and R. F. Wallis, J. Phys. C **6**, 1226 (1973).

[30] V. V. Tarasenko and V. D. Kharitonov, Zh. Eksp Teor. Fiz. **60**, 2321 (1971 Sov. Phys.-JETP **33** 1246).

[31] R. E. Camley, Phys. Rev. Lett. **45**, 283 (1980).

[32] B. Hillebrands and K. Ounadjela, *Spin Dynamics in Confined Magnetic Structures I* (Springer, Berlin 2001).

[33] D. D. Stancil and A. Prabhakar, *Spin Waves: Theory and Applications* (Springer, New York, 2009).

[34] M. G. Cottam and D. J. Lockwood, *Light Scattering in Magnetic Solids* (Wiley, New York, 1986).

[35] E. A. Albuquerque and M. G. Cottam, *Polaritons in Periodic and Quasiperiodic Structures* (Elsevier, Amsterdam, 2004).

[36] C. Kittel, *Introduction to Solid State Physics, 8th edn.* (Wiley, New York 2005).

[37] R. Marcelli and S. A. Nikitov (eds), *Nonlinear Microwave Signal Processing: Towards a New Range of Devices*(Kluwer, Dordrecht, 1996).

[38] C. Herring and C. Kittel, Phys. Rev. **81**, 869 (1951).

[39] T. Wolfram and R. De Wames, Prog. Surf. Sci. **2**, 233 (1972).

[40] B. A. Auld, J. Appl. Phys. **31**, 1642 (1960).

[41] M. S. Bose, E. N. Foo and M. A. Zuniga, Phys. Rev. B **12**, 3885 (1975).

[42] R. E. Camley and D. L. Mills, Phys. Rev. B **26**, 1280 (1982).

[43] F. A. Oliveira, A. F. Khater, E. F. Sarmento and D. R. Tilley, J. Phys. C **12**, 4021 (1979).

[44] J. T. Yu, R. A. Turk and P. E. Wigen, Phys. Rev. B. **11**, 420 (1975).

[45] J. A. C. Bland and B. Heinrich (eds.), *Ultrathin Magnetic Structures I* (Springer, Berlin, 1994).

[46] J. R. Sandercock and W. Wettling, J. Appl. Phys. **50**, 7784 (1979).

[47] P. Grünberg and F. Metawe, Phys. Rev. Lett.**39**, 1561 (1977).

[48] P. A. Fleury, S. P. S. Porto, L. E. Cheesman and H. J. Guggenheim, Phys. Rev. Lett.**17**, 84 (1966).

[49] J. R. Sandercock , Phys. Rev. Lett. **28**, 237 (1972a).

[50] J. R. Sandercock , Phys. Rev. Lett. **29**, 1735 (1972b).

[51] P. Grünberg, Prog. Surf. Sci.**18**, 1 (1985).

[52] P. Grünberg, *Light Scattering in Solids V*, ed. by M. Cardona and G Güntherodt, (Springer, Berlin 1989).

[53] W. Hayes and R. Loudon, *Scattering of Light by Crystals*(John Wiley and Sons, New York, 1978).

[54] B. Hillebrands and G G*ü*ntherodt, *Ultrathin Magnetic Structures II*, ed. by B. Heinrich and J.A.C. Bland, (Springer, Berlin 1994).

[55] D. E. Brown, T. Dumelow, M. R. F. Jensen and T. J. Parker, Infrared Phys. Tech. **40**, 219 (1999).

[56] M. R. F. Jensen, T. J. Parker, Kamsul Abraha and D. R. Tilley, Phys. Rev. Lett. **75**, 3756 (1995).

[57] M. R. F. Jensen, S. A. Feiven, T. J. Parker and R. E. Camley, J. Phys.: Condens. Matter **9**, 7233 (1997).

[58] A. Otto, Z. Physik **216**, 398 (1968).

[59] K. L. Hobbs, P. R. Larson, G. D. Lian, J. C. Keay and M. B. Johnson, Nano Lett. **4**, 167 (2004).

[60] Z. K. Wang, H. S. Lim, H. Y. Liu, S. C. Ng, M. H. Kuok, L. L. Tay, D. J. Lockwood, M. G. Cottam, K. L. Hobbs, P. R. Larson, J. C. Keay , G. D. Lian and M. B. Johnson, Phys. Rev. Lett. **94**, 137208 (2005).

[61] S. O. Demokritov, B. Hillebrands and A. N. Slavin, Physics Reports, **348**, 441 (2001).

[62] A. Kozhanov, D. Ouellette, Z. Griffith, M. Rodwell, A. P. Jacob, D. W. Lee, S. X. Wang and S. J. Allen, Appl. Phys. Lett. **94**, 012505 (2009).

[63] S. O. Demokritov, J. Phys.: Condens. Matter **15**, 2575 (2003).

[64] R. Arias and D. L. Mills, Phys. Rev. B **72**, 104418 (2005).

[65] B. Heinrich and J. A. C. Bland (eds.), *Ultrathin Magnetic Structures II* (Springer, Heidelberg, 1994).

[66] C. T. Boone, J. A. Katine, J. R. Childress, V. Tiberkevich, A. Slavin, J. Zhu, X. Cheng and I. N. Krivorotov, Phys. Rev. Lett. **103**, 167601 (2009).

[67] M. A. Monteiro, G. A. Farias, R. N. Costa Filho, and N.S. Almeida, Eur. J. Phys. **61**, 121 (2008).

[68] R. Arias and D. L. Mills, Phys. Rev. B **63**, 134439 (2001).

[69] Z. K. Wang, M. H. Kuok, S. C. Ng, D. J. Lockwood, M. G. Cottam, K. Nielsch, R. B. Wehrspohn and U. Gösele, Phys. Rev. Lett. **89**, 027201 (2002).

[70] T. K. Das and M. G. Cottam, Surf. Rev. and Lett. **14**, 471 (2007).

[71] T. K. Das and M. G. Cottam, IEEE Trans. Magnetics **46**, 1544 (2010).

[72] M. L. Plumer, J. van Ek and D. Weller, *The Physics of Ultra-High-Density Magnetic Recording*, ed. by M. L. Plumer, J. van Ek and D. Weller, (Springer, Berlin 2001).

[73] T. M. Nguyen, M. G. Cottam, H. Y. Liu, Z. K. Wang, S. C. Ng, M. H. Kuok, D. J. Lockwood, K. Nielsch and U. Gösele, Phys. Rev. B **73**, 140402(R), (2006).

[74] L. Giovannini, F. Montoncello, F. Nizzoli, G. Gubbiotti, G. Carlotti, T. Okuno, T. Shinjo and M. Grimsditch, Phys. Rev. B **70**, 172404 (2004).

[75] W. Xu, D. B. Watkins, L. E. DeLong, K. Rivkin, J. B. Ketterson and V. V. Metlushko, J. Appl. Phys. **95**, 6645, (2004).

[76] T. M. Nguyen and M. G. Cottam, J. Appl. Phys. **99**, 1, (2006).

[77] G. Gubbiotti, M. Madami, S. Tacchi, G. Carlotti, H. Tanigawa, T. Ono, L. Giovannini, F. Montoncello and F. Nizzoli , Phys. Rev. Lett. **97**, 247203 (2006).

[78] K. Nielsch, R. B. Wehrspohn, J. Barthel, J. Kirschner, U. Gösele, S. F. Fischer and H. Kronmüller, Appl. Phys. Lett. **79**, 1360 (2001).

[79] K. Mika and P. Grünberg, Phys. Rev. B **31**, 4465 (1985).

[80] E. A. Albuquerque and M. G. Cottam, Physics Reports **376**, 225 (2003).

[81] D. Shi, B. Aktaş and F. Mikailov, *Nanostructured Magnetic Materials and Their Applications* (Springer, Berlin, 2002).

[82] T. M. Sharon and A. A. Maradudin, J. Phys. Chem. Solids **38**, 977 (1977).

[83] N. S. Almeida, G. A. Farias, N. Oliveira and E. Vasconcelos, Phys. Rev. B **48**, 9839 (1993).

[84] M. Abramowitz and I. A. Stegun, *Handbook of Mathematical Functions: with Formulas, Graphs, and Mathematical Tables* (Dover Publications, New York 1965).

[85] H. Y. Liu, Z. K. Wang, H. S. Lim, S. C. Ng, M. H. Kuok, D. J. Lockwood, M. G. Cottam, K. Nielsch and U. Gösele, J. Appl. Phys. **98**, 046103 (2005).

[86] H. Leblond and V. Veerakumar, Phys. Rev. B **70**, 134413 (2004).

[87] R. E. Camley, B. Djafari-Rouhani, L. Dobrzynski, and A. A. Maradudin, Phys. Rev. B **27**, 7318 (1983).

[88] P. Harrison, *Quantum Wells, Wires and Dots, 2nd edn.* (Wiley, Chichester, 2005).

[89] R. E. Camley and D. L. Mills, Phys. Rev. B **18**, 4821 (1978).

[90] M. G. Cottam, J. Phys. C: Solid State Phys. **12**, 1709 (1979).

[91] T. K. Das and M. G. Cottam, AIP Conf. Proc. **1147**, 536 (2009).

[92] T. K. Das and M. G. Cottam, Journal of Physics: Conf. Ser. **200**, 072022 (2010).

[93] A. E. Berkowitz and K. Takano, J. Magn. Magn. Mater. **200**, 552 (1999).

[94] J. Nogués and I. K. Schuller, J. Magn. Magn. Mater. **192**, 203.

[95] S. O. Demokritov and B. Hillebrands, J. Magn. Magn. Mater. **200**, 706 (1999).

[96] J. I. Martín, J. Nogués, K. Liu, J. L. Vicent and I. K. Schuller, J. Magn. Magn. Mater. **256**, 449 (2003).

[97] R. L. Stamps and K. D. Usadel, Europhysics Lett. 74, 512 (2006).

[98] I. V. Roshchin, O. Petracic, R. Morales, Z. P. Li, X. Batlle and I. K. Schuller, Europhysics Lett. **71**, 297 (2005).

[99] B. Negulescu, R. Tanasa and A. Stancu, J. Optoelectron. Adv. Mater. **6**, 991 (2004).

[100] T. K. Das and M. G. Cottam, J. Mag. Magn. Mat. **310**, 2183 (2006).

[101] T. K. Das and M. G. Cottam, J. Appl. Phys. **103**, 07B104 (2008).

[102] T. M. Nguyen and M. G. Cottam, Phys. Rev. B **71**, 094406 (2005).

[103] R. L. Stamps and R. E. Camley, Phys. Rev. B **40**, 596 (1989).

[104] E. F. Nobre, R. S. T. Moretzsonh, R. C. Vilela, G. A. Farias and N. S. Almeida, Braz. J. Phys. **36**, 967 (2006). (1999).

[105] E. F. Nobre, R. N. Costa Filho, G. A. Farias and N. S. Almeida, Phys. Rev. B **57**, 10583 (1998).

[106] E. F. Vasconcelos, N. T. Oliveira, G. A. Farias and N. S. Almeida, Phys. Rev. B **44**, 12621 (1991).

[107] F. Schott, T. Tao and R. Freibun, J. Appl. Phys. **38**, 3015 (1967).

[108] M. S. Kushwaha and B. Djafari-Rouhani, Phys. Rev. B **71**, 195317 (2005).

[109] E. F. Nobre, G. A. Farias and N. S. Almeida, J. Opt. Soc. Am. **17**, 173 (2000).

[110] W. Wettling, M. G. Cottam, and J.R. Sandercock, J. Phys. C **8**, 211 (1975).

[111] B. L. Johnson and R. E. Camley, Phys. Rev. B **43**, 6554 (1991).

[112] T. K. Das and M. G. Cottam, J. Appl. Phys. (submitted).

[113] Z. K. Wang, V. L. Zhang, H. S. Lim, S.C. Ng, M. H. Kuok, S. Jain, and A. O. Adeyeye, Appl. Phys. Lett. **94**, 083112 (2009).

[114] G. Gubbiotti, S. Tacchi, G. Carlotti, P. Vavassori, N. Singh, S. Goolaup, A. O. Adeyeye, A. Stashkevich, and M. Kostylev, Phys. Rev. B **72**, 224413 (2005).

[115] R. L. Stamps and R. E. Camley, Phys. Rev. B **35**, 1919 (1987).

[116] K. Yu. Guslienko and A. N. Slavin, Phys. Rev. B **72**, 014463 (2005).

[117] G. T. Rado and J.R. Weertman, J. Phys. Chem. Solids **11**, 315 (1959).

[118] P. Böni, M. Hennion and J. L. Martínez, Phys. Rev. B **52**, 10142 (1995).

[119] F. Hoffmann, G. Woltersdorf, K. Perzlmaier, A. N. Slavin, V. S. Tiberkevich, A. Bischof, D. Weiss and C. H. Back, Phys. Rev. B **76**, 014416 (2007).

[120] M. A. Popov and I. V. Zavislyak, Ukr. J. Phys. **53**, 702 (2008).

[121] M. G. Cottam and A. A. Maradudin, *Surface Excitations, Vol. 9 of Modern Problems in Condensed Matter Sciences* (North-Holland, Amsterdam, 1984).

[122] Alexander L. Fetter and John Dirk Walecka, *Quantum Theory of Many-Particle Systems* (Dover Publications, New York, 2003).

[123] C. Kittel, *Quantum Theory of Solids* (Wiley, New York 1987).

[124] G. D. Mahan, *Many-Particle Physics* (Plenum, New York, 1990).

[125] R. D. Mattuck, *A Guide to Feynman Diagrams in the Many-Body Problem* (Dover Publications, New York, 1992).

[126] R. C. Moul and M. G. Cottam, J. Phys. C: Solid State Phys. **16**, 1307 (1983).

[127] A. Kreisel, F. Sauli, L. Bartosch, and P. Kopietz, Eur. Phys. J. B **71**, 59 (2009).

[128] W. J. Padilla, D. N. Basov and D. R. Smith, Materials Today **9**, 28 (2006).

[129] F. Magnus, B. Wood, J. Moore, K. Morrison, G. Perkins, J. Fyson, M. C. K. Wiltshire, D. Caplin, L. F. Cohen and J. B. Pendry, Nature Materials **7**, 295(2008).

[130] V. M. Shalaev, Nature Photon. **1**, 41 (2007).

[131] J. B. Pendry, A. J. Holden, D. J. Robbins and W. J. Stewart, IEEE Trans. Microwave Theory Tech. **47**, 2075 (1999).

[132] G. A. Farias, E. F. Nobre, R. Moretzsohn, N. S. Almeida and M. G. Cottam, J. Opt. Soc. Am. **19**, 2449 (2002).

[133] N. Bloembergen and P. S. Pershan, Phys. Rev. **128**, 606 (1962).

[134] S.M. Rezende and F.M. de Aguiar, J. Appl. Phys. **79**, 6309 (1996).

[135] A. D. Boardman, S. A. Nikitov,Q. Wang,J. S. Bao and Y. S. Cai, SPIE Int. Conf. on Thin Film Physics and Applications **1519**, 597 (1991).

[136] S. Lim, J. Phys.: Condens. Matter **18**, 4329 (2006).

[137] S. Lim, J. Osman and D. R. Tilley, J. Phys. D: Appl. Phys. **33**, 2899 (2000).

Vita

Name:	Tushar Kanti Das

Education and Degrees:

University of Western Ontario

London, Ontario, Canada

2007 - 2010 Ph.D.

2004 - 2006 M.Sc.

The Abdus Salam International Centre for Theoretical

Physics, Trieste, Italy

2001 - 2002 Diploma in Condensed Matter Physics.

Shah Jalal University of Science and Technology

Sylhet, Bangladesh

1997 - 1998 M.Sc.

1994 - 1997 B.Sc.

Honors and awards:

Graduate Entrance Scholarship, 2007

Graduate Tuition Scholarship, 2004 - 2010

The University of Western Ontario

London, Ontario, Canada.

ICTP Diploma Scholarship

The Abdus Salam International Centre for Theoretical

Physics, Trieste, Italy, 2001 - 2002.

Related work

experience: Teaching Assistant

The University of Western Ontario

2004 - 2010.

Lecturer

Shah Jalal University of Science and Technology

2000 - Present (On study leave).

Publications: T. K. Das and M. G. Cottam,

J. Appl. Phys. (submitted).

T. K. Das and M. G. Cottam,

IEEE Trans. Magnetics **46**, 1544 (2010).

T. K. Das and M. G. Cottam,

Journal of Physics: Conf. Ser. **200**, 072022 (2010).

T. K. Das and M. G. Cottam,

AIP Conf. Proc. **1147**, 536 (2009).

T. K. Das and M. G. Cottam,

J. Appl. Phys. **103**, 07B104 (2008).

T. K. Das and M. G. Cottam,

Surf. Rev. and Lett. **14**, 471 (2007).

T. K. Das and M. G. Cottam,

J. Mag. Magn. Mat. **310**, 2183 (2006).

A. Giacometti, D. Gazzillo, G. Pastore and T. K. Das,

Phys. Rev. E**71**, 031108 (2005).